



**Universitat**  
de les Illes Balears

**DOCTORAL THESIS**

**Study of the Generation of Optical Pulses  
by Mode-Locking in Semiconductor Lasers  
for Applications in LiDAR Systems**

**Daniel Chaparro González**

**2019**





**Universitat**  
de les Illes Balears

**DOCTORAL THESIS**  
Doctoral Programme in Physics

**Study of the Generation of Optical Pulses  
by Mode-Locking in Semiconductor Lasers  
for Applications in LiDAR Systems**

**Daniel Chaparro González**  
Doctor by the Universitat de les Illes Balears

**Advisor:**  
Prof. Dr. Salvador Balle Monjo

**Tutor:**  
Prof. Dr. Raúl Toral Garcés

**2019**



This thesis has been written by Mr. Daniel Chaparro González under the supervision of Dr. Salvador Balle Monjo.

Palma, 12 de septiembre de 2019

**Advisor:**

Dr. Salvador Balle Monjo

**PhD student:**

Mr. Daniel Chaparro González

The work presented in this thesis has been possible thanks to the funding provided by the Ministerio de Economía y Competitividad by the call “Ayudas para contratos predoctorales para la formación de doctores 2013” through the grant BES-2013-065230, linked to the project TEC2012-38864-C03-01, as well as the financial support provided by the “Plan Estatal de Investigación Científica y Técnica y de Innovación” through Project TEC2015-65212-C3-3-P.





## List of publications derived from this thesis

- **D. Chaparro** and Salvador Balle, “Optical Addressing of Pulses in a Semiconductor-Based Figure-of-Eight Fiber Laser,” Physical Review Letters, vol. 120, iss. 6, pp. 064101-064105, Feb. 2018.  
DOI: 10.1103/PhysRevLett.120.064101
- **D. Chaparro**, L. Furfaro and S. Balle, “247 fs Time-localized structures from a passively mode-locked figure-of-eight semiconductor laser,” 2017 Conference on Lasers and Electro-Optics Europe & European Quantum Electronics Conference (CLEO/Europe-EQEC), Munich, 2017, pp. 1-1.  
DOI: 10.1109/CLEOE-EQEC.2017.8087528
- **D. Chaparro**, L. Furfaro, and Salvador Balle, “Subpicosecond pulses in a self-starting mode-locked semiconductor-based figure-of-eight fiber laser,” Photonics Research 5, 37-40, 2017.  
DOI: 10.1364/PRJ.5.000037
- M. Marconi, P. Camelini, S. Barland, M. Giudici, J. Javaloyes, **D. Chaparro** and S. Balle, “Temporal localized states in semiconductors (II): from mode-locking to localized pulses,” 2015 Spatiotemporal Complexity in Nonlinear Optics (SCNO), Como, Italy, 2015, pp. 1-3.  
DOI: 10.1109/SCNO.2015.7324011
- M. Marconi, P. Camelini, M. Giudici, J. Javaloyes, **D. Chaparro** and S. Balle, “Localized pulses in passively mode-locked semiconductor lasers,” 2016 Photonics North (PN), Quebec City, QC, 2016, pp. 1-1.  
DOI: 10.1109/PN.2016.7537880
- M. Marconi, J. Javaloyes, P. Camelini, **D. C. González**, S. Balle and M. Giudici, “Control and Generation of Localized Pulses in Passively Mode-Locked Semiconductor Lasers,” in IEEE Journal of Selected Topics in Quantum Electronics, vol. 21, no. 6, pp. 30-39, Nov.-Dec. 2015, Art no. 1101210.  
DOI: 10.1109/JSTQE.2015.2435895



## Acknowledgements

Research can be compared with hiking through a wild path. It is an adventure for brave people with the only knowledge of the starting line and the final goal where blocking rockfalls, landslides, brushwood, thicket and rifts may be found. Here is where the helping hand of a good guide makes the difference in surviving the journey. Fortunately, I was lucky enough to count on my way with Dr. Salvador Balle, my thesis supervisor. I want to thank Salvador all what I have learned from him, not only about physics but also about how the work of a scientist must be: passionate, committed, ethical and highly self-demanding and self-critical to ensure the good quality of the results. Thank you very much for teaching me how to cut the thicket and how to bridge the rifts in the wild path of research.

I am also thankful to Dr. Massimo Giudici for his kind guidance in the knowledge of VCSELs during the months of internship in the Institute Non Linéaire de Nice at the beginning of this thesis. Thank you very much to all the French Ph.D. students (now Doctors) there for their friendship and those good ping-pong matches. Mathias, Patrice, Cristina, Alex, Bruno, Simona, Gustave François *et al...*merci à tous!

Very special thanks to Dr. Luca Furfaro for the great technical help offered whenever required. Thank you for your brilliant ideas and for making those crazy devices work when nobody else could. I was skeptical the first time I heard Salvador saying *If there is a person that can make it work...that is Dr. Luca Furfaro*. Now, it is me the one who proclaims this sentence. Thank you for all the time you spent with me in the lab without minding the time or hunger.

I appreciate also the support provided by Dr. Marc Sorel, Dr. Ignacio Esquivias and Dr. Antonio Pérez Serrano by means of so many useful discussions and comments.

Thanks also to Dr. Julien Javaloyes for its guidance in the lab during the first steps of the experimental work and for developing the codes for the acquisition of the experimental data.

However, not only troubles are present when hiking. Green fields can also be found during the journey where one can briefly take a pleasing rest and regain energy. As it is known, those moments have a much better taste if they are shared with beloved people as my colleagues and friends from IMEDEA. Thank you, Gema, for shouting out loud *There is a newbie in the office!!!* in front of everybody the first day I arrived timidly asking if there were any available desk. Thank you, Adri, for teaching me some of the ancestral zen techniques of the bread making. Thank you, Juanma, for letting me know that a scientific mind does not need to be odds with a deep spirituality. Thank you, Eva, for teaching me that scientists can also show calmness and serenity. Thanks to Paula for her big lesson about tenacity and perseverance. I am also grateful to Ana Payo for

irradiating optimism and a unique attitude in facing life (Ana, trust me...it opened my mind). Big thanks to Alex & Miguel who very kindly gave me shelter twice...thank you for so many interesting debates at home. Thank you, Vero, Javi and Edu for being the legal representatives of Andalucía in IMEDEA...you helped me a lot to feel at home. Thank you, Laura Royo, for pushing me to sing and being a member of the Galàctic Swing Cor. And HUGE thanks to Lucía for sharing with me the passion for music and for being a great support in the bad moments and an amazing source of laughs in the good ones. Thanks also to Josep, Romain, Andrea, Albert, Marc, Manu, Noelia, Merit & Carlos, Esther, Laura, Marina, Guillem, Guille, Dani, Xisca, Eva, Sara...sorry if somebody does not find his/her name here, it is just that I have to stop writing names at some point but you are all in my memory. Also thanks to all the PAS of IMEDEA in special to Ramona for radiating always good vibes with a smile on her face.

My non-IMEDEIC friends on the island are also on my mind: Dani & Rocío, Gemma, Vincent, Miguel, Emilio, Alberto, and some of the best musicians I have ever played with...Pau, Pilu, Alberto and Mateo, "The Black Moaning". Thank you all for so many good moments.

Finally, I have saved this paragraph to the most special people to me: my closest friends and family. Gracias a mis amigos de Sevilla por hacerme sentir como si no me hubiera ido nunca de allí cuando volvía de visita. Gracias a mis hermanos y a mis sobrinas por tantos abrazos. Miles de gracias a mi novia, SARA, mi motor y mi motivación. Gracias por ser tan auténtica, única e irremplazable como eres. Por quererme y cuidarme cada uno de los 13 años que llevamos juntos y, en especial, por tu paciencia y tu fuerza en estos últimos 4 años en los que has soportado mi caos mental de tesista esperándome al otro lado del Mediterráneo. Gracias también a Tesla, nuestro perro, por cuidar tan bien de Sara los complicados años que ha pasado en Almería. Un abrazo y un beso al cielo para mis suegros a los que tengo siempre presentes y que, de seguro, se alegrarán desde algún lugar privilegiado por la finalización de esta tesis. Y, por supuesto, miles de gracias y mi más profundo reconocimiento a MIS PADRES, un apoyo incondicional e inquebrantable en la distancia tanto en épocas de aguas revueltas como de aguas tranquilas. Muchas gracias por tantos años de cuidados, cariños, juegos, dedicación, sacrificios y enseñanzas. Muchas gracias por haberme hecho quien soy. Os quiero a todos...disculpadme si la distancia ha resultado más dura de lo esperado.





A los tres pilares de mi vida:  
mi madre, mi padre y Sara.



## Abstract

The present work constitutes a study on the generation and control of optical pulses in different kind of semiconductor lasers and their potential application to remote measurement systems. First, a brief introduction to the techniques most commonly used for the realization of remote measurements by light will be made and the benefits with which semiconductor lasers can contribute to these techniques in both continuous and pulsed emission will be justified. Next, it will be described the generation of pulse trains that takes place in an experimental assembly formed by a vertical cavity surface emitting laser with emission at 980 nm in an external cavity configuration through two mechanisms: cross-reinjection of polarization in the laser and mode-locking by coupling the laser to a resonant saturable absorber mirror. The possibility of controlling the number of pulses in the train through the electrical modulation of the laser bias current will be studied and the capacity of generating different pulse patterns by activating and deactivating the electrical modulation will be demonstrated. Next, an adaptation of the mentioned experimental assembly will be carried out in which the propagating medium for light will be changed from being air to optical fiber. A first fiber laser assembly will be studied consisting in a unidirectional ring configuration in which the gain medium will be a semiconductor optical amplifier with emission at 1550 nm and, almost exclusively, in a single polarization. Under this scheme, it will be pursued to reproduce the generation of pulses under the same mechanisms previously exposed for the system emitting at 980 nm and it will be shown how the pulses obtained with this system can be used to perform ranging measurements. The relevant role played by the evolution of the polarization in its trip along the optical fiber in the previous configuration and the difficulty on its deterministic control will lead to the exploration of new topologies for the experimental configuration of the fiber laser. A configuration of two coupled loops, known as a *figure-of-eight* and formed by polarization-maintaining fibers, capable of generating different highly stable pulse train regimes, having a width of the order of femtoseconds, will be described through the variation of the laser bias current. Finally, the construction of a fully optical reinjection branch added to the experimental assembly will allow the selection of a single pulse of the train and its subsequent reinjection in it will be described, and the possibility of erasing a previously written pulse will also be demonstrated. The ability to write and delete multiple pulses on the train at will proves their nature as temporal localized structures and demonstrates the possibility of using such a system as an all-optical generator of arbitrary ultra-short pulse patterns.



## Resumen

El presente trabajo constituye un estudio sobre la generación y control de pulsos ópticos en diferentes tipos de láseres de semiconductor y su potencial aplicación a sistemas de medidas a distancia. En primer lugar, se realizará una breve introducción a las técnicas más comúnmente empleadas para la detección y realización de medidas a distancia mediante la luz y se justificarán los beneficios que los láseres de semiconductor pueden aportar a dichas técnicas tanto en emisión continua como en emisión pulsada. Seguidamente, se describirá la generación de trenes de pulsos que tiene lugar en un montaje experimental formado por un láser de semiconductor de emisión superficial en cavidad vertical externa con emisión a 980 nm a través de dos mecanismos: la reinyección cruzada de polarización en el láser y enganche de modos mediante el acople a un espejo resonante de absorbente saturable. Se estudiará la posibilidad de controlar el número de pulsos en dicho tren a través de la modulación eléctrica de la corriente de alimentación del láser, demostrando la posibilidad de generar diferentes patrones de pulsos mediante la activación y desactivación de la modulación eléctrica. A continuación, se realizará una adaptación de dicho montaje experimental en el que el medio propagante para la luz pasará de ser el aire a ser fibra óptica. Se estudiará un primer montaje de láser en fibra en configuración de anillo unidireccional en el que el medio de ganancia pasará a ser un amplificador óptico de semiconductor con emisión a 1550 nm y, casi exclusivamente, en una única polarización. Bajo dicho esquema, se perseguirá reproducir la generación de pulsos bajo los dos mismos mecanismos expuestos previamente para el sistema emitiendo a 980 nm y se mostrará cómo los pulsos obtenidos con este sistema permiten ser usados para realizar medidas a distancias. El papel relevante jugado por la evolución de la polarización en su viaje a lo largo de la fibra óptica en la configuración anterior y la dificultad en el control determinista de la misma, llevarán a la exploración de nuevas topologías para la configuración experimental del láser en fibra. Se describirá una configuración de dos bucles acoplados, conocida como *figura de ocho* y formada por fibras mantenedoras de la polarización, capaz de generar diferentes regímenes de trenes de pulsos altamente estables, que presentan una anchura del orden de los femtosegundos, a través de la variación de la corriente de alimentación del láser. Finalmente, se describirá la construcción de una rama de reinyección completamente óptica añadida al montaje experimental que permitirá la selección de un único pulso del tren y su posterior reinyección en el mismo y se demostrará, también, la posibilidad de borrar un pulso previamente escrito. La capacidad de escribir y borrar a voluntad múltiples pulsos en el tren prueba la naturaleza de los mismos como estructuras localizadas y demuestra la posibilidad de usar dicho sistema como un generador óptico de patrones arbitrarios de pulsos ultracortos.



## Resum

El present treball constitueix un estudi sobre la generació i control de polsos òptics en diferents tipus de làsers de semiconductor i el seu potencial aplicació a sistemes de mesures a distància. En primer lloc, es realitzarà una breu introducció a les tècniques més comument emprades per a la detecció i realització de mesures a distància mitjançant la llum i es justificaran els beneficis que els làsers de semiconductor poden aportar a aquestes tècniques tant en emissió contínua com en emissió pulsada. Seguidament, es descriurà la generació de trens de polsos que té lloc en un muntatge experimental format per un làser de semiconductor d'emissió superficial en cavitat vertical externa amb emissió a 980 nm a través de dos mecanismes: la reinjecció creuada de polarització en el làser i enganxament de modes mitjançant l'acoblament d'un mirall resonant d'absorbent saturable. S'estudiarà la possibilitat de controlar el nombre de polsos en aquest tren a través de la modulació elèctrica del corrent d'alimentació del làser, demostrant la possibilitat de generar diferents patrons de polsos mitjançant l'activació i desactivació de la modulació elèctrica. A continuació, es realitzarà una adaptació de l'esmentat muntatge experimental en què el medi propagant per a la llum passarà de ser l'aire a ser fibra òptica. S'estudiarà un primer muntatge de làser en fibra en configuració d'anell unidireccional en què el medi de guany passarà a ser un amplificador òptic de semiconductor amb emissió a 1550 nm i, gairebé exclusivament, en una única polarització. Sota aquest esquema, es perseguirà reproduir la generació de polsos sota els dos mateixos mecanismes exposats prèviament per al sistema emetent a 980 nm i es mostrerà com els polsos obtinguts amb aquest sistema poden ser usats per a realitzar mesures de distàncies. El paper rellevant jugat per l'evolució de la polarització en el seu viatge al llarg de la fibra òptica a la configuració anterior i la dificultat en el control determinista de la mateixa, han de portar a l'exploració de noves topologies per a la configuració experimental del làser en fibra. S'ha desenvolupat una configuració de dos bucles acoblats, coneguda com a *figura de vuit* i formada per fibres mantenidores de la polarització, capaç de generar diferents règims de trens de polsos altament estables, que presenten una durada temporal de l'ordre dels femtosegons, a través de la variació del corrent d'alimentació del làser. Finalment, es descriurà la construcció d'una branca de reinjecció completament òptica afegida al muntatge experimental que permetrà la selecció d'un únic pols del tren i la seva posterior reinjecció en el mateix i es demostrarà, també, la possibilitat d'escriure i/o d'esborrar un pols prèviament escrit. La capacitat d'escriure i esborrar a voluntat múltiples polsos al tren prova la naturalesa dels mateixos com a estructures localitzades i demostra la possibilitat d'usar aquest sistema com un generador òptic de patrons arbitraris de polsos ultracurts.



# Contents

<b>1</b>	<b>Introduction</b>	<b>1</b>
1.1	LiDAR: origins and applications . . . . .	1
1.2	Ranging techniques based on lasers . . . . .	3
1.3	Semiconductor lasers in LiDAR systems: use and advantages . . . . .	9
1.4	Generation of pulses by mode-locked semiconductor lasers . . . . .	10
1.4.1	Vertical-cavity surface-emitting lasers . . . . .	12
1.4.2	Semiconductor-based fiber lasers . . . . .	14
1.4.3	Pulses as localized structures in semiconductor lasers . . . . .	17
1.5	Overview of this thesis . . . . .	22
<b>2</b>	<b>Generation and control of pulses in a passively mode-locked VCSEL in an external cavity</b>	<b>25</b>
2.1	Antecedents to the study . . . . .	25
2.2	Description of the experimental setup . . . . .	31
2.3	Pulse addressing and multi-pulse pattern generation . . . . .	33
2.4	Theoretical evaluation of the generated pattern . . . . .	36
2.5	Conclusions to the Chapter . . . . .	41
<b>3</b>	<b>Generation of pulses in a SOA-based ring fiber laser</b>	<b>43</b>
3.1	From an air-based VCSEL arrangement to a fiber-based SOA design .	43
3.2	Characterization of the optical devices . . . . .	49
3.3	Generation of pulses by a SOA-based fiber laser with a saturable absorber	55
3.4	Generation of pulses by a SOA-based fiber laser under cross-polarization reinjection . . . . .	58
3.5	Proof of principles: fibered SOA laser pulses for LiDAR measurements	77
3.6	Conclusions to the Chapter . . . . .	81
<b>4</b>	<b>Subpicosecond pulses in a self-starting mode-locked semiconductor-based figure-of-eight fiber laser</b>	<b>83</b>
4.1	Introduction . . . . .	84
4.2	Experimental Setup . . . . .	85
4.3	Experimental results . . . . .	85

4.4	Conclusions . . . . .	92
<b>5</b>	<b>Optical addressing of pulses in a SOA-based Figure-of-Eight fiber laser</b>	<b>93</b>
5.1	Introduction . . . . .	93
5.2	Experimental Setup . . . . .	96
5.3	Experimental results . . . . .	96
5.4	Supplemental material . . . . .	103
<b>6</b>	<b>Summary and conclusions</b>	<b>109</b>
	<b>Bibliography</b>	<b>115</b>

## List of Figures

1.1	Advantages of LiDAR data over traditional map views of the landscape for archaeological purposes . . . . .	2
1.2	Setup for LiDAR data collection mounted in a drone . . . . .	3
1.3	Schematic illustration of the principles of RM-CW LiDAR . . . . .	5
1.4	Schematic setup of a CLiDAR system with an optically injected semiconductor laser . . . . .	6
1.5	Three irregular (possibly chaotic) states for CLiDAR obtained experimentally with decreasing injection strengths . . . . .	6
1.6	Ranging resolution plotted as a function of chaos bandwidth . . . . .	7
1.7	Illustration of the general principles of FMCW LiDAR operation . . . . .	8
1.8	Illustration of the mode-locking mechanism for the emission of pulses . . . . .	11
1.9	A typical gallium arsenide-based vertical-cavity surface-emitting laser (VCSEL) structure . . . . .	12
1.10	Power reflectivity of a linear fiber loop mirror as a function of the coupling ratio of the used fiber coupler . . . . .	16
1.11	Near field of a VCSEL in which different LS have been independently written as binary pixels using a phase mask . . . . .	18
1.12	Localized structures generated by a F8L containing a polarization controller which presents different pulsing states based on a locked or a rotating polarization. . . . .	23
2.1	Experimental setup for the implementation of XPR and PSF in a VCSEL emitting at 850 nm . . . . .	26
2.2	Pulsed emission of the VCSEL due to the polarization dynamics originated from XPR and PSF . . . . .	27
2.3	Space-time diagrams of different coexisting pulsed situations . . . . .	28
2.4	Temporal signal obtained when detecting simultaneously either one or two spots of the far-field emission of the VCSEL . . . . .	29
2.5	Coexisting time traces with different pulse number . . . . .	30
2.6	Bifurcation scenario as a function of the gain for different values of the delay . . . . .	31

2.7	Experimental setup for the passive mode-locking of pulses through the coupling of a VCSEL and an RSAM . . . . .	32
2.8	Time traces showing the experimental process for pulse generation via current modulation . . . . .	34
2.9	Addressing of independent pulses by applying a sinusoidal modulation to the bias current of the VCSEL . . . . .	35
2.10	Writing of a pulse when the modulation period is set to half the round-trip	36
2.11	Different co-existing time traces of the temporal intensity over several and two round-trips for $\Delta g = 0.23$ and $\tau_m = \tau + 0.26$ . . . . .	38
2.12	Gain and absorption dynamics for the simulations performed over the two co-existing time traces in 2.11 . . . . .	39
2.13	Numerical bifurcation diagram for the pulse number as a function of the modulation of the gain . . . . .	40
2.14	Numerical bifurcation diagram for the pulse number as a function of the detuning modulation period as compared to the cavity round-trip	40
3.1	Typical attenuation and responsitivity for the usual operating range of optical fiber systems . . . . .	45
3.2	Typical fibered SOA containing an InP/InGaAsP quantum well inside a butterfly case . . . . .	46
3.3	Typical arrangements of RSAM devices . . . . .	47
3.4	Typical external aspect and internal operation of a manually tunable bandpass filter . . . . .	48
3.5	Different kind of controllers for the management of the polarization in optical fiber . . . . .	48
3.6	ASE corresponding to each of the legs of the SOA used for the generation of pulses . . . . .	49
3.7	2D-maps for the characterization of the central wavelength and FWHM of the SOA with respect to the temperature and bias current . . . . .	51
3.8	Optical spectra corresponding to the SOA and RSAM in different configurations . . . . .	52
3.9	Detail of the displacement of the resonance wavelength of the RSAM for different temperatures at fixed current and temperature values of the SOA . . . . .	53
3.10	Characterization of the absorption of the RSAM when its temperature is varied for constant current and temperature values of the SOA . . . . .	54

3.11 All fibered experimental setup for a laser in a unidirectional ring cavity configuration for the generation of pulses by passive mode-locking induced by saturable absorption . . . . .	55
3.12 Charaterization of the optical bandpass tunable fibered filter . . . . .	56
3.13 Emission of brief and different coexisting pulsed states produced by the fibered SOA–RSAM ring cavity for the same set of parameters values	58
3.14 Setup for the generation of pulses by crossed reinjection polarization .	59
3.15 Management of the polarization performed by the IPC to the signal sent by the SOA when the DC current is modulated by a triangular signal	62
3.16 LI curves corresponding to different cases of reinjection of light in the SOA . . . . .	65
3.17 LI curve by reinjection of an elliptical state of light obtained by setting the half-wave plate at $11^\circ$ with respect to the case of $y$ -polarization . .	67
3.18 Temporal traces by reinjection of an elliptical state of light obtained by setting the half-wave plate at $11^\circ$ with respect to the case of $y$ -polarization and varying the current . . . . .	68
3.19 Optical spectra obtained by reinjection of an elliptical state of light achieved by setting the half-wave plate by $11^\circ$ with respect to the case of $y$ -polarization and varying the current . . . . .	69
3.20 Severe differences in the LI curves accomplished by reinjecting two close elliptical states of light obtained by setting the half-wave plate at two angles values –with respect to the case of $y$ -polarization reinjection– showing a tiny variation below the instrumental error of the controller	70
3.21 Temporal traces corresponding to the LI curve shown in Figure 3.20b and Figure 3.20d obtained for different current values . . . . .	71
3.22 Temporal trace showing a square wave generated by a reinjection performed with a random position of the paddles of the controller . . . . .	72
3.23 Temporal traces obtained by reinjections performed with a random but fixed position of the paddles of the controller and varying the current .	73
3.24 Temporal traces showing a multiplicity of coexistent states for a fixed set of parameters values at a current of 287 mA . . . . .	74
3.25 Space-time diagram showing the evolution of pulses generated by a random position of the paddles of the in-line fibered polarization controller	75
3.26 Experimental setup for the proof-of-principles of LiDAR measurements	78
3.27 Delay times produced on the temporal trace by patch cords of different length. The blue line stands for the reference trace while the orange, yellow, purple and green lines show respectively the traces for patch cord lengths of 0 m, 1 m, 2 m, and 5 m. . . . .	79

3.28 Temporal delay experienced by the optical pulses as a function of the length of the replaceable patch cord described in 3.26. The green dots stand for the experimental points while the orange line shows the linear regression of the data and the blue line represents the theoretical delay line calculated for a standard refractive index for silica fiber of 1.5 . . . . .	80
4.1 Photograph and schematics of the self-starting pulsed F8L setup . . . . .	86
4.2 Output power of the F8L when the substrate temperature is $T = 20^\circ\text{C}$ as the bias current of the SOA is increased and decreased . . . . .	87
4.3 Optical spectra of the F8L output when the substrate temperature is $T = 20^\circ\text{C}$ for different bias currents . . . . .	88
4.4 Time trace and RF spectrum of the fundamental mode-locked emission of the F8L when the substrate temperature is $T = 20^\circ\text{C}$ and the bias current $I = 85.2 \text{ mA}$ . . . . .	89
4.5 Time traces and RF spectra of the F8L emission when the substrate temperature is $T = 20^\circ\text{C}$ for different values of the bias current close to the lasing threshold . . . . .	90
4.6 Optical spectra of the pulses before and after amplification by the L-band fiber amplifier. RF spectrum and intensity autocorrelation trace and $\text{sech}^2$ fit of the amplified pulses . . . . .	91
5.1 Schematics of the F8L setup for the addressing of pulses . . . . .	95
5.2 Time trace, optical spectrum and RF spectrum of the pulse train with a single pulse per roundtrip with the fundamental repetition period of 55 ns and with two pulses per roundtrip with a delay of 15 ns. Space-time diagram showing the stability of the two-pulses state over $\sim 1000$ roundtrips . . . . .	97
5.3 Variation of the temporal location of a pulse from 17 ns to 15 ns when the reinjection current is decreased from 80 mA to 0 mA . . . . .	98
5.4 Optical addressing of individual pulses with a reinjection delay of $\sim 15$ ns . . . . .	100
5.5 Creation of a cluster of pulses with spacing $\sim 2$ ns and erasure of individual pulses . . . . .	101
5.6 Erasure of the central pulse of a three-pulse cluster . . . . .	102
5.7 Theoretical space-time distribution of the local gain in the fundamental state . . . . .	107

## Acronyms

**ADC** Analog-to-Digital Converter.

**AML** Active Mode-Locking.

**ASE** Amplified Spontaneous Emission.

**CFBG** Chirped Fiber Bragg Grating.

**CW** Continous Wave.

**DS** Dissipative Solitons.

**EPC** External Polarization Controller.

**EPG** Electrical Pulse Generator.

**F8L** Figure-of-Eight Laser.

**FC/APC** Fiber Connectors exhibiting Angled Physical Contact.

**FMCW** Frequency-Modulated Continuous-Wave.

**FPBS** Fibered Polarizing Beam Splitter.

**FWHM** Full Width at Half Maximum.

**GPS** Global Positioning System.

**IMU** Inertia Measurement Unit.

**IPC** Intracavity Polarization Controller.

**LD** Laser Driver.

**LS** Localized Structures.

---

*Acronyms*

---

**ML** Mode-Locking.

**NALM** Nonlinear Amplifying Loop Mirror.

**NOLM** Nonlinear Optical Loop Mirror.

**NPR** Nonlinear Polarization Rotation.

**OSA** Optical Spectrum Analyzer.

**PM** Polarization Maintaining.

**PML** Passive Mode-Locking.

**PRBS** Pseudo Random Binary Sequence.

**PSF** Polarization Selective Optical Feedback.

**RF** Radio-Frequency.

**RM-CW** Random Modulated Continuous Wave.

**RSAM** Resonant Saturable Absorber Mirror.

**SESAM** Semiconductor Saturable-Absorber Mirror.

**SNR** Signal-to-Noise Ratio.

**SOA** Semiconductor Optical Amplifier.

**TE** Transverse Electric.

**TEC** Thermoelectric Cooler.

**TELS** TErrestrial Laser Scanners.

**TLSs** Temporal LS.

**TM** Transverse Magnetic.

**TOF** Time Of Flight.

**VCSEL** Vertical-Cavity Surface-Emitting Laser.

**XPR** Crossed Polarization Reinjection.

# **Chapter 1**

## **Introduction**

### **1.1 LiDAR: origins and applications**

LiDAR is a technique for teledetection based on the use of laser light which has become a standard nowadays in an extensive variety of ranging applications. The basic principle of LiDAR consists in the emission of an optical pulse onto an object and the later detection and processing of the reflected or scattered signal to determine the distance. In the same way as the techniques using sound or radio waves under this scheme for the ranging of objects were named SONAR and RADAR, the analogous use of light for these same purposes received the name of LiDAR which is the acronym of Light Detection and Ranging. However, other denominations may also be found in the literature to refer to these techniques and devices as LIDAR (Light Intensity Detection and Ranging), LADAR (Laser Detection and Ranging), laser range finders, laser scanners or laser radars [1].

The origins of LiDAR arose in the early 1960s, barely two years after the construction of the first functioning laser [2–5]. Although light had already been used since the late 1930s to measure atmospheric properties by means of searchlight devices [6–9], the potential of the improvements offered by laser light over conventional light sources such as its monochromaticity, coherence, narrow spectral width and beam, tunability of the operation frequency and possibility of pulsed emission, were rapidly recognized by the scientific community as an ideal tool for remote sensing and originated a whole new field of research on the techniques using light for ranging [10, 11].

LiDAR systems allow for the retrieval of information both from the ground and the atmosphere depending on whether the light is emitted from the air (airborne LiDAR) or from the ground (terrestrial LiDAR). Furthermore, in comparison with other ranging techniques, LiDAR systems exhibit robust advantages such as the high speed of data collecting, extremely high accuracy or higher surface data sampling due to the shorter wavelengths of light [12]. These features, together with the possibility of acquiring 2D and 3D images, allow LiDAR applications to encompass a vast range of topics of broad and current interest like astronomy and atmospherical studies [13–20],

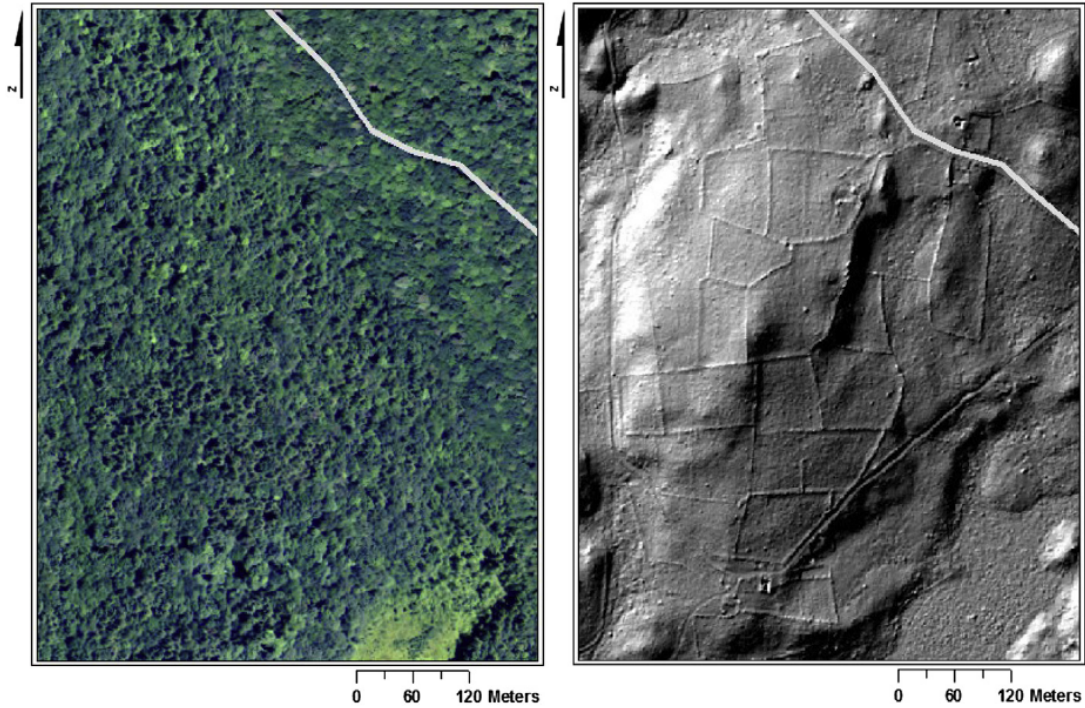


Figure 1.1: Advantages of LiDAR data over traditional map views of the landscape for archaeological purposes. The left image shows a leaf-on aerial photograph with a modern road superimposed through the northeast corner of the image for reference. The right image was created from LiDAR data and depicts many archaeological features which cannot be seen from aerial photographs (adapted from [57]).

nuclear reactors [21], self-driving cars [22–26], biology and conservation [27–34], geology and soil science [35–41], solar photovoltaic deployment optimization [42–47], wind farm optimization [48–50], forestry [51–53], robotics [54–56] or archaeology (see Figure 1.1) [57–60].

In general, LiDAR systems are integrated by many different components which may –or not– be present on its design depending on the purpose for which it has been fabricated. Thus, LiDARs stations in ground and aerial vehicles may integrate on their designs a Global Positioning System (GPS) to record the location coordinates of the scanner and an Inertia Measurement Unit (IMU) to compensate the movements of the vehicle and ensure the correct calculations of distances (see Figure 1.2) [61–64].

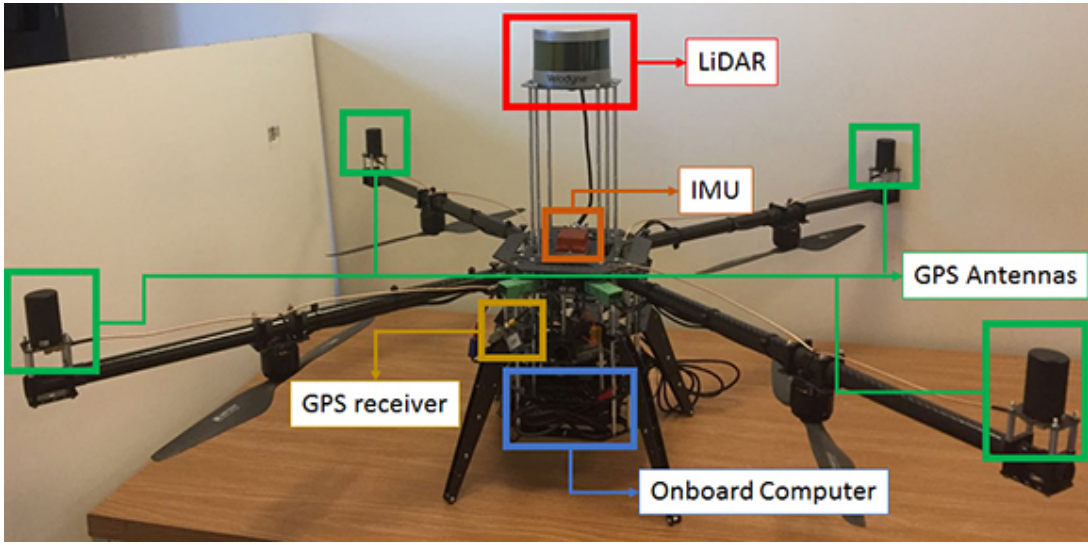


Figure 1.2: Setup for data collection mounted in a drone assembling a LiDAR unit, a GPS receiver, antennas, an IMU, and an onboard computer [61].

On the other hand, fixed ground-based LiDAR stations such as TERrestrial Laser Scanners (TELS) used in architecture to obtain 3D-images of facades of buildings or infrastructures may disregard these additional components as they are not a requirement for this type of measurements. However, the laser can be considered the cornerstone of any LiDAR system as it is always present in any design, triggers the ranging process by generating the light to be used and determines the resolution and sampling rate of the measure by means of the temporal width and repetition rate of the emitted pulses.

## 1.2 Ranging techniques based on lasers

The more traditional remote measurements techniques using lasers can be classified into three main categories: triangulation, interferometry and Time Of Flight (TOF) [65]. Triangulation is the simplest method to obtain the distance from an object and profits from the capability of laser beams to travel long distances in a well-collimated shape due to its low divergence. Under this technique, an object whose distance wants to be known is pointed with a beam and the backscattering from the target is monitored by a photodetector perpendicularly placed to the line of sight at a known

distance from the laser. The triangular configuration formed by the emitter, the target, and the receptor allows to measure the angle between the forward and backward lines of sight and calculate the distance between the pointer and the target. On the other hand, interferometry exploits the coherence property of lasers to make interfere the beam sent to the target and its reflection and to derive the distance information from the changes in the phase of the signal. Finally, TOF techniques directly measure the time spent by the light pulse in the round-trip from the emitter to the target and back to the receptor. The distance can be easily derived from the elemental relation  $2L = \tau c$ , where  $L$  is the distance from the emitter to the target,  $\tau$  is the round-trip time and  $c$  is the speed of light. The spatial accuracy of the measurement is given by the temporal width of the pulses which, due to the high value of the speed of light, must be very short to achieve high spatial resolutions (pulse width of 1 ns is required to achieve a spatial resolution of 15 cm). Alternatively to light pulses, TOF systems can also send a Continuous Wave (CW) and evaluate the distance with high resolution using either the phase delay or the frequency change of the backscattered continuous radiation [66, 67].

During the last decades, techniques in a halfway between CW and pulsed TOF LiDARs have also been developed. One of these techniques is the known as Random Modulated Continuous Wave (RM-CW) LiDAR in which a Pseudo Random Binary Sequence (PRBS) is imposed in a CW laser by an electro-optical modulator switching on and off the emitting laser according to a fundamental clock period that defines the shortest on and off widths [68]. This allows the outcoming light from the laser to be emitted as a binary and arbitrary pulsed light pattern which is periodically repeated after a certain delay time. Once that this patterned light reaches the target and is back-reflected, the signal is detected as a delayed and attenuated signal – following the inverse square law to the distance – which is digitized in a low noise receiver and compared with the original PRBS pattern. The cross-correlation function between the transmitted PRBS sequence and the delayed received version allows for the calculation of the delay time to be used for determining the distance of the object with a non-ambiguous range (see Figure 1.3) [69, 70]. In RM-CW LiDARs, the range of unambiguous detection is limited due to the finite length of the PRBS sequence and the repetition frequency rate. Besides, the resolution is typically limited by the Analog-to-Digital Converter (ADC) sampling rate and the PRBS bit width (chip time) to the range of the meters. However, some methods have demonstrated the possibility of enhancing the resolution up to the centimeter as, for example, the addition of an analog integrator installed prior to the digital cross-correlation process [71] or the application of a fast modulation to the laser with bit-to-bit samples at clock rates up to the gigahertz range [69].

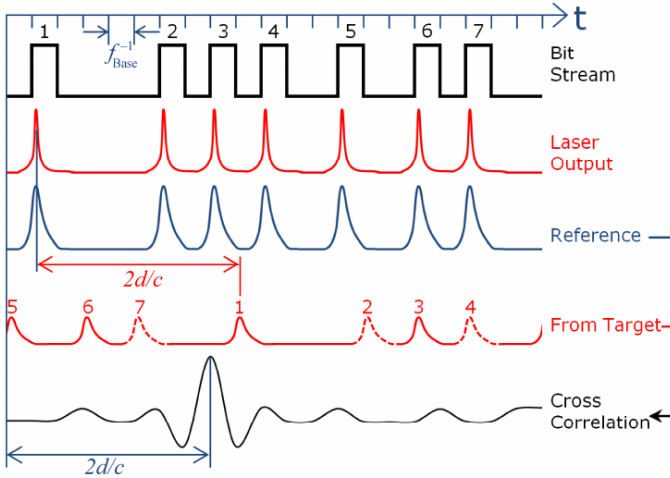


Figure 1.3: Schematic illustration of the principles of RM-CW LiDAR from the transmitted and delayed PRBS signals. From up to bottom: the PRBS, the laser output modulated by the PRBS, the signal of reference, the attenuated back reflection from the object and the cross-correlation between the reference and echo-signal [69].

Over the last years, LiDAR systems have still been an object of intense research and new ranging techniques using chaotic lasers (CLiDAR) have been designed. Although, the principles for the range finding supporting CLiDAR are essentially the same than those for RM-CW LiDAR –the correlation of the back-reflected signal from the target with a reference waveform–, the use of chaotic lasers offers important advantages. Among them, it is found that chaotic dynamics can be easily generated in many different setups containing laser diodes under proper operating conditions including optical feedback, optoelectronic feedback or optical injection showing noise-like output waveforms with a  $\delta$ -type autocorrelation trace (see Figure 1.4 and Figure 1.5) [72]. In addition, while conventional LiDARs show resolutions in the order of the meters, the broad bandwidth of chaos makes possible to achieve resolutions in the range of the millimeter (see Figure 1.6). Furthermore, the unrepeatability of a chaotic waveform solves the ambiguity caused by the limited length of pseudo-random codes and does not require modulation electronics or high-speed code generation [72, 73].

The usual criterion for the evaluation of the performance and efficiency of LiDAR systems is based on the assessment of the Signal-to-Noise Ratio (SNR) at the photodetector output which is a comprehensive parameter to evaluate the efficiency of the

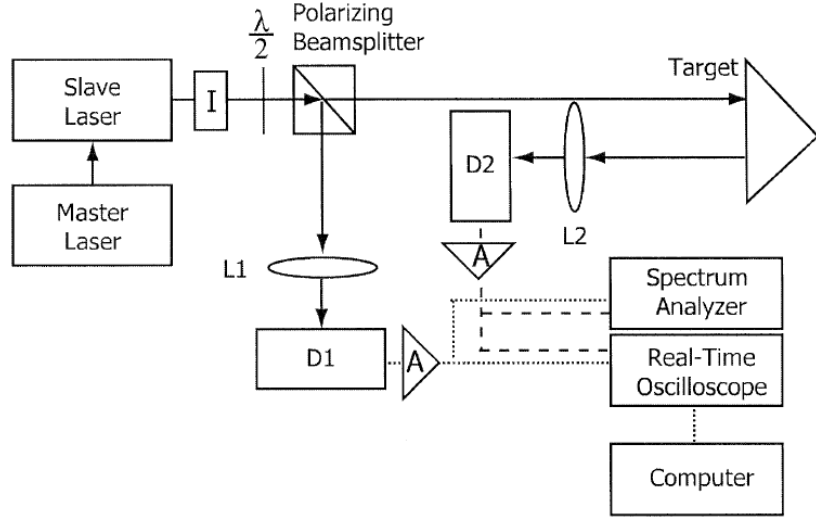


Figure 1.4: Schematic setup of a CLiDAR system with an optically injected semiconductor laser [72] ©2004 IEEE.

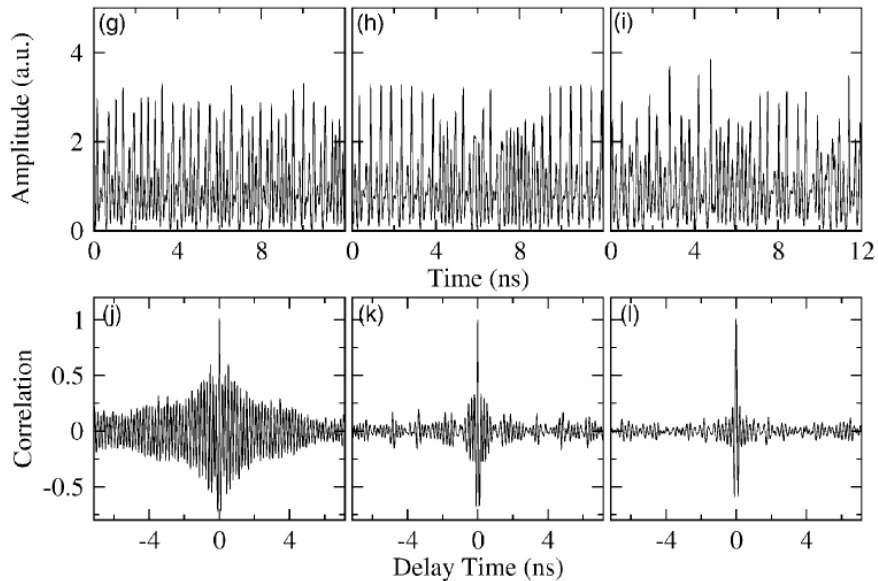


Figure 1.5: Three irregular (possibly chaotic) states obtained experimentally with decreasing injection strengths. (g)–(i) Time series. (j)–(l) Autocorrelation traces [72] ©2004 IEEE.

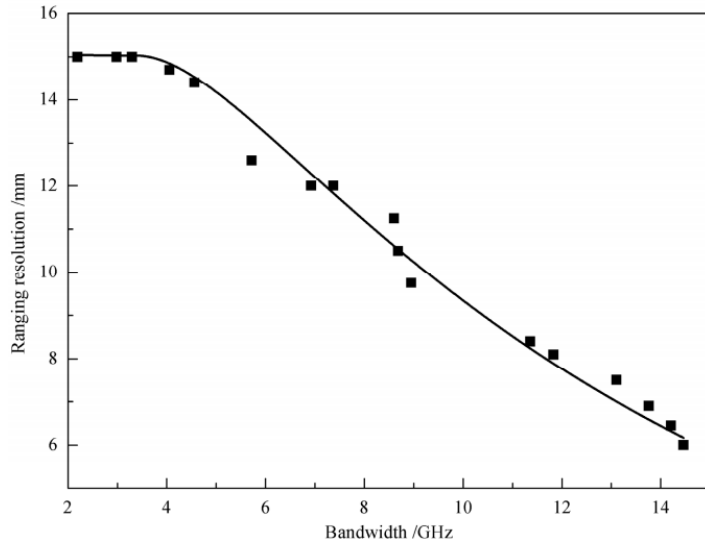


Figure 1.6: Ranging resolution plotted as a function of chaos bandwidth. Squares correspond to experimental points and the solid curve is the regression [73]

instrument [74]. However, SRN has to be carefully controlled as it may also obscure some characteristics of the measurements if any increase or reduction on it occurs due to uncontrolled background conditions or changes of the propagation of the signal, what may translate in a detrimental impact in the capabilities of the system. In fact, the effective detection of ultra-short pulses in LiDAR systems requires a rather broad transmission band of the receiver which may increase the noise level and cause the prejudicial detection of the retro-illumination from distant targets [75].

Hence, much of the research efforts nowadays in the field of LiDAR systems are directed towards both the improvement of the SNR and resolution. As it was previously mentioned, it is possible to obtain high-resolution LiDAR measurements by using CW systems under the phase-shift method although this technique presents as a drawback the ambiguity in the measure due to the  $2\pi$ -modulo of the phase [66]. However, this limitation can be overcome by the modulation of the phase or the frequency of the signal. In this context, Frequency-Modulated Continuous-Wave (FMCW) LiDAR is a technique in which a spectrum of range-frequencies is selected after the echo-signal from the target and the local heterodyne optical signal interact on the sensitive area of the photodetector allowing for a receiver with a narrower frequency band, noise re-

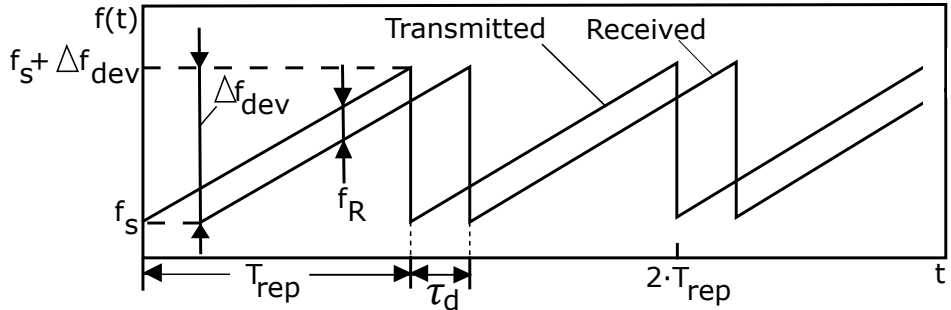


Figure 1.7: Illustration of the general principles of FMCW LiDAR operation where the frequency shift in the delay time between the emitted and received signals allows for determining the range distance to the object [75] (adapted).

duction and good resolution. FMCW LiDAR supports on imposing an asymmetrical linear frequency modulation to the light emitted by the laser towards the target (see Figure 1.7). The slope of the linear frequency modulation,  $\gamma$ , is constant during the repetition period of the modulating signal,  $T_{\text{rep}}$  and is determined by  $\gamma = \Delta f_{\text{dev}}/T_{\text{rep}}$ , where  $\Delta f_{\text{dev}}$ , is the frequency deviation of the laser transmitter. Hence, the frequency shift in the time lapsed between the detection of the emitted signal and the reflected echo,  $\tau_d$ , originates a beat note that allows to uniquely determine the distance to the target as  $f_R = \gamma\tau_d = 2R\Delta f_{\text{dev}}/cT_{\text{rep}}$  where  $R$  is the ranging distance and  $c$  is the speed of light. As mentioned before, the presence of some heterodyning method is required for the selection of a narrow frequency band that allows the improvement of the SNR. The resolution of FMCW LiDAR is given by  $\Delta R_{\text{FMCW}} = c\Delta f_r/2f_{\text{rep}}\Delta f_{\text{dev}}$ , where  $\Delta f_r$  is the filter pass-band. The setting of the filter to the value of the repetition frequency allows for the reduction of the noise and determines the potential resolution that can be obtained under this scheme which is given by  $\Delta R_{\text{FMCW}}^{\text{pot}} = c/2\Delta f_{\text{dev}}$  [75]. The use of linearly chirped light by means of FMCW has demonstrated the capability to perform measurements with sub-millimeter resolution and unambiguous range determination for an object placed at 10 km by the use of a Chirped Fiber Bragg Grating (CFBG) applied to pulses emitted at a repetition rate of 20 MHz [76]. In this situation, lines separated by 20 MHz conform the optical spectrum showing a spectral envelope of width 1 THz. The CFBG imposes a linear wavelength-dependent delay to each of these spectral components stretching the pulses up to 10 ns of duration. However, the stretched pulses do not fill the entire pulse period causing dead zones due to the lack of pulse overlap which can be overcome using CFBG with higher dispersion, lasers with larger optical bandwidth or higher repetition frequency.

In addition to the previously mentioned techniques, another possibility for the improvement of the resolution in LiDAR systems consists in the reduction of the pulse duration as it determines the potential resolution of systems based on TOF techniques (optical pulses shorter than 6.7 ps of Full Width at Half Maximum (FWHM) are required in order to obtain spatial resolutions of 1 millimeter). Thus, the research on ultra-short pulses to be applied in LiDAR systems constitute a hot topic nowadays. However, narrow pulses require more bandwidth with the direct consequence of the increase of noise in the receiver and, therefore, a higher pulse power for achieving a good SNR. Furthermore, aliasing of the received pulses limits the maximum range in these simple TOF LiDAR systems what obeys to the use of low pulse repetition frequencies for unambiguous long-range measurements.

### **1.3 Semiconductor lasers in LiDAR systems: use and advantages**

As referred in Section 1.1, lasers are the cornerstone of any LiDAR system. The basic operation of a laser consists in the amplification of the stimulated emission of photons by a gain medium in a cavity. Hence, one possible classification of lasers rests on the nature of the gain medium used what makes possible to find different kind of LiDAR systems based in gas lasers [77–79], solid-state lasers [80–83] or dye lasers [84–86].

Semiconductor lasers are optoelectronic devices based on the electrical pumping of the p–n junction of semiconductor material. The development of the optical communication technology has recently brought to the stage a new generation of high speed and high power semiconductor lasers in the eye-safe region of 1.5  $\mu\text{m}$ . These cheap and highly efficient light sources can represent an interesting alternative to the traditional laser sources and have attracted the attention towards its use in LiDAR systems [87–93] especially for its incorporation in an aircraft or a satellite.

The advantages offered by the performance of these lasers make of them an interesting light source for ranging techniques such as RM-CW LiDAR where the capability of direct modulation of semiconductor lasers and its relatively high average power fit very well to the requirements of this technique. However, the lack of the extremely high peak power convenient for long range pulsed systems slightly reduces the SNR in comparison with pulsed systems although this can be compensated by the higher average power [94]. Although the resolution of an RM-CW LiDAR is limited in principle by the ADC sampling rate and the PRBS bit width, studies applying new interpolation techniques in systems using semiconductor lasers have overcome this drawback reaching resolution values of centimeters over distances around 10 meters [71].

As mentioned, CLiDARs systems have also been reported using semiconductor lasers emitting in a chaotic regime due to optical injection of another laser or to optical feedback from the same laser [72, 73]. Semiconductor lasers are able to emit chaotic pulse trains with several desirable properties for CLiDAR applications such as a rapid decorrelation leading to unambiguous range measurements, short pulse widths and high average pulse repetition frequencies [95]. Furthermore, the capability of noise filtering due to synchronization has made possible to develop a synchronized CLiDAR showing a better detection performance [96]. Recently, a promising technique for achieving higher range resolutions in CLiDAR systems consisting in the enhancement of a chaotic signal when applying optical injection and feedback simultaneously to a semiconductor laser has been developed [97].

FMCW techniques for LiDAR have also benefited from the use of semiconductor lasers demonstrating their potential for very high-resolution measurements using frequency-swept semiconductor lasers as emitters. In particular, a spatial resolution as low as 250  $\mu\text{m}$  for a target distance of 4 cm has been demonstrated by means of current modulation at 100 Hz and a thermally-induced wavelength shift [98].

## 1.4 Generation of pulses by mode-locked semiconductor lasers

As stated in Section 1.2, the reduction of the length of the pulses conveys an improvement of the resolution in LiDAR systems. Mode-Locking (ML) is a technique for the generation of very short and energetic pulses at repetition rates determined by the round-trip time of light in the laser cavity. It is based on the simultaneous oscillation of a high number of longitudinal modes of the cavity sharing a fixed phase relationship [99]. When these modes interfere constructively, they allow for the emission of the light as a train of pulses and it is said the laser is *mode-locked* (see Figure 1.8). The number of modes participating in the locking is fixed by the cavity dispersion and the spectral width of the gain which, in turn, determines the temporal width of the pulses. Hence, the broad gain curve exhibited by semiconductor lasers makes them serve as natural candidates for the generation of ultrashort pulses by ML.

ML can be achieved either actively or passively [101]. On the one hand, Active Mode-Locking (AML) can be obtained by imposing a modulation over one of the parameters of the system (usually the gain or losses) at a frequency corresponding to the inverse of the cavity round-trip or a sub-harmonic of it. On the other hand, Passive Mode-Locking (PML) relies on the presence of some intra-cavity element producing power-dependent losses and favoring the pulsed emission. PML of semiconductor

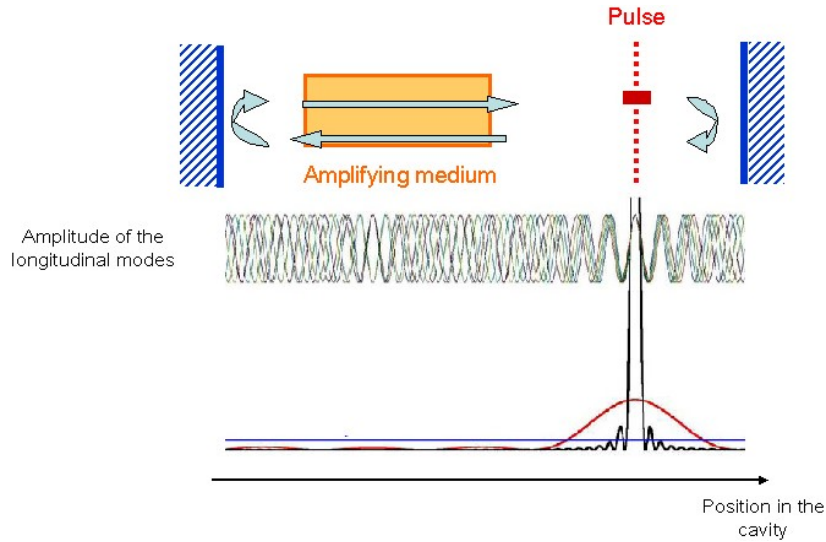


Figure 1.8: Illustration of the mode-locking mechanism for the emission of pulses. The different sinusoidal curves represent the amplitude of the electrical field for different modes of the cavity [100].

lasers is usually achieved by incorporating a saturable absorber which presents a high absorption when receiving low optical intensities and vice versa [102] or by a reverse-biased section that acts as a saturable absorber. This technique results in the emission of pulses with a duration in the range of the picosecond or longer [103, 104], although they can be further reduced down to hundreds of femtosecond by compressing the pulses. Other mechanisms inducing mode-locked pulses may also be found in the literature like the combination of active and passive ML in the so-called hybrid ML [105] the Kerr-lens ML [106] or the nonlinear polarization rotation [107].

One of the advantages of semiconductor lasers is the possibility to integrate the laser in a monolithic cavity. However, while PML in these devices shows typical values of the repetition frequency in the order of the hundreds of GHz, AML is limited in the range of the tens of GHz [101]. The demands required in different applications have motivated lots of research towards the extension of these repetition frequencies to higher values and also lower values as in the case of remote sensing. The pulse repetition rate can be controlled by an appropriate cavity design. Long-cavity designs can be used to lower the fundamental repetition rate down to  $\sim 1$  GHz, but in this case, the pulse duration usually exceeds 10 ps [108, 109]. Colliding-Pulse ML at twice the fundamental repetition rate is obtained by placing the Saturable Absorption in

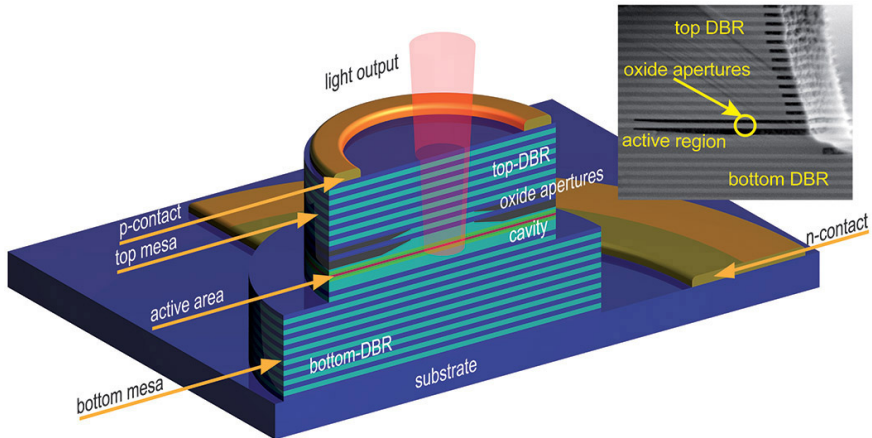


Figure 1.9: A typical gallium arsenide-based vertical-cavity surface-emitting laser (VCSEL) structure. The design features an active region that contains quantum wells sandwiched between two multilayer mirrors which creates a planar cavity. Carriers are injected through the metal contacts at the top and bottom of the structure, and light is emitted from the top [115].

the center of the cavity [110], and a further increase is still possible by choosing other locations, but with increasingly stringent requirements on the placement and length of the Saturable Absorber section. In turn, the pulse repetition rate can be reduced by using long cavity designs [108] or external-cavity configurations [111], but when the cavity length exceeds the recovery time of the gain, different harmonic states of the fundamental mode-locked regime can be obtained due to the background instability associated with their short gain recovery time (in the nanosecond range) [112].

#### 1.4.1 Vertical-cavity surface-emitting lasers

Among semiconductor lasers, the Vertical-Cavity Surface-Emitting Laser (VCSEL) represents one of the main advances in the field in the last decades [113, 114]. The configuration of a vertical cavity, in which the light is emitted perpendicularly to the plane of the active region (see Figure 1.9) [115], was first proposed by Kenichi Iga in 1977. Devices operating as a continuous wave at room temperature were first obtained in 1989 and began to be commercialized in 1996 [114]. A lot of unique features characterize these lasers, such as low cost, low power consumption, wafer-level testing for low-cost manufacturing, narrow circular beam for direct fiber coupling, the capability

of integration in large-scale two-dimensional arrays, and high-speed modulation with low driving current [113]. Other advantages include ultra-low-threshold currents, high wall-plug efficiency above 50% and optical power ranging from few milliwatts to several watts for emission in a broad range of wavelengths and covering multiple applications. However, although the development of VCSELs operating at 1550 nm for telecommunication purposes has been slow due to some technical challenges –such as those linked to the fabrication of mirrors of high reflectivity and low electrical resistivity allowing the pass of current or those related to the design and growth of the active region in some semiconductor materials [116]–, it has been recently demonstrated their use for telecommunications purposes reaching transmission rates up to 115 Gb/s [117–120].

VCSELs are also used in various optical sensor applications due to their high efficiency for battery-powered applications, single optical wavelength, flexible packaging options, high radiance, and reliability [118]. Reflective, transmissive, absorptive and scattering sensors have been reported using VCSELs as well as self-mixing sensors in which a weak signal is fed back into the laser from a distant reflector. Self-mixing sensors can be used to measure position and velocity using the Doppler shift in the laser [121, 122]. Very recently, attention has been paid to exploit the vectorial nature of light for self-mixing sensors and rotation sensors based on the polarization properties of VCSELs under polarization-rotating optical feedback have been recently demonstrated [123].

Under proper perturbations, a single-mode VCSEL can exhibit highly complex dynamical characteristics ranging from stable, narrow-linewidth oscillation to broadband chaos. In recent years two main approaches have been invoked to obtain complex nonlinear dynamical states in single-mode VCSELs: optical injection and optical feedback. Optical injection is a technique that improves the performance of VCSELs in optical communication systems reducing the chirp and extending the modulation bandwidth, even beyond 100 GHz [124]. Period-one oscillation obtained by optical injection on a VCSEL has also been used for Doppler-LiDAR detection using a dual-frequency source [125]. The dual frequency source is characterized by a single-sideband nature of the optical spectrum, typical of period-one oscillation. The dual-frequency beam emitted by the VCSEL is divided into two parts with a beam splitter: the transmitted part of the beam is detected by a photodiode while the reflected part is directed to a remote moving target. The backscattered light from the target is detected by a second photodiode and the microwave envelope of the target arm experiences a Doppler shift. The velocity of the target is related to that shift, which is extracted by mixing the signals of the two photodiodes with a microwave mixer. This dual-frequency Doppler-LiDAR system showing 17 GHz period-one oscillation has been used to measure velocities as small as 26  $\mu\text{m/s}$  at a range of 15 m. Period-one oscillations with similar frequencies

have been obtained in 1550 nm single-mode VCSELs subject to optical injection [126].

An increasing injected power is required for achieving higher frequencies. Double optical injection in multi-transverse mode VCSELs can increase significantly the frequency of period-one oscillations [127, 128] without using large values of injected power: the injection of a multimode VCSEL on a similar multimode VCSEL can produce a period-one oscillation at a frequency given by the separation between transverse modes (typically larger than 100 GHz). These high-frequency oscillations can also find applications in Radio-over-Fibre transmission [129, 130]. Broadband chaos in 1550 nm VCSELs has been obtained by using optical injection [126], optical feedback [97], or both simultaneously [97].

ML of VCSELs requires an external-cavity configuration since their short monolithic cavities originate highly separated frequency modes, with few of them under the gain curve, what makes necessary to enlarge the external cavity to operate efficiently the mode-locked regime. Furthermore, although the ML of the transverse modes is feasible [131], it is troublesome due to overlapping effects and the irregularity of the modal frequencies [132]. PML of the external cavity modes has been demonstrated [133, 134] by using a Semiconductor Saturable-Absorber Mirror (SESAM) [135], delivering optical pulses of widths in the 10 ps range and repetition rates up to 20 GHz. VCSELs can also provide passively mode-locked operation by exploiting cross-gain modulation between the two polarizations [136, 137] which allows eliminating the SESAM. As pointed before, remote sensing applications demand lower repetitions frequencies which can be achieved by using long cavities. For VCSELs in external cavities, it has been recently demonstrated that quite low repetition rates (in the order of tens of MHz) can be achieved in certain circumstances [138]. In this regime, a large number of stable lasing states that differ in the number of pulses per cycle and their position within the cycle are available. Under this situation, the optical pulses become independent entities known as temporal localized structures, that can be individually addressed to generate almost arbitrary pulse patterns with the potential to improve the performance of CW-RM LiDAR systems.

#### **1.4.2 Semiconductor-based fiber lasers**

Although the origins in the development of pulsed laser sources relied on solid-state lasers [139], fiber lasers have emerged as a reliable alternative to bulky solid-state lasers for optical pulse generation [140] providing compactness, high beam quality with high efficiency and mechanical robustness of the fibered cavity. However, dispersion management is more problematic in fiber lasers due to fiber dispersion, and the optical powers that can be achieved in fiber lasers are usually lower than those obtained

in solid-state lasers. Most fiber lasers rely on a fiber section doped with rare-earth ions, which provide gain upon optical pumping but fiber lasers using a Semiconductor Optical Amplifier (SOA) as the gain element have also been developed since they offer the simplicity of electrical pumping, high nonlinearity, rapid tuning, and a broad gain bandwidth [141–145].

AML of SOA-based fiber lasers in unidirectional ring cavities has allowed obtaining optical pulses with a duration of 15 ps [146], which can be further amplified and compressed down to 50 fs [147]. PML has been achieved in different SOA-based fiber lasers exploiting the nonlinear polarization rotation where a power-dependent polarization change is converted into a power-dependent transmission through a polarizing optical element. Thus, 800 fs pulses at the fundamental ML frequency of 14 MHz in a unidirectional SOA-based fiber laser have been obtained [148]. In addition, dark and bright pulses can be obtained in a similar configuration [149]. In this case, the pulses arise from a square-wave intensity modulation that can be quite slow and that can be useful for generating optical clocks with high duty cycle, and the repetition rate of the pulses can be increased by operating the device in the harmonic ML regime.

Another way to implement a mode-locked emission in fiber lasers is by means of nonlinear loop mirrors which can act as artificial saturable absorbers triggering and stabilizing the pulsed emission [150, 151]. In a linear fiber loop, the ports of one side in a two-by-two fiber coupler are connected to each other. In this situation, the signal sent to one input port is split in two counter-propagating waves traveling along the loop and the interference between these waves, when they meet again at the coupler, determines the power of the light sent back into the input and the remaining port. Assuming the simplest case with a coupler presenting fibers of equal lengths a coupling ratio of 50% and in the absence of losses or nonlinear effects the interference conditions are such that all injected power goes back to the port into which it was injected and the loop operates as a perfect mirror [152].

On the contrary, the deviation from this ideal case of any of the previously mentioned parameters causes the reduction of the reflectivity of the loop (see Figure 1.10). In particular, it is possible to find variations of such a fiber loop showing non-symmetrical designs in which the coupling ratio differs from the 50% (named Nonlinear Optical Loop Mirror (NOLM)) or configurations in which light propagating along the loop is amplified by means of a rare-earth-doped fiber or a SOA (named Nonlinear Amplifying Loop Mirror (NALM)). In case of ultra-short pulses with substantial peak power, the nonlinear phase changes in the loop are stronger for light propagating in one direction than in the other since one arrives earlier to the gain medium and is amplified first and then travels through the long passive fiber. Light in the opposite direction propagates with a lower power level for most of the length. As a result, the interference conditions

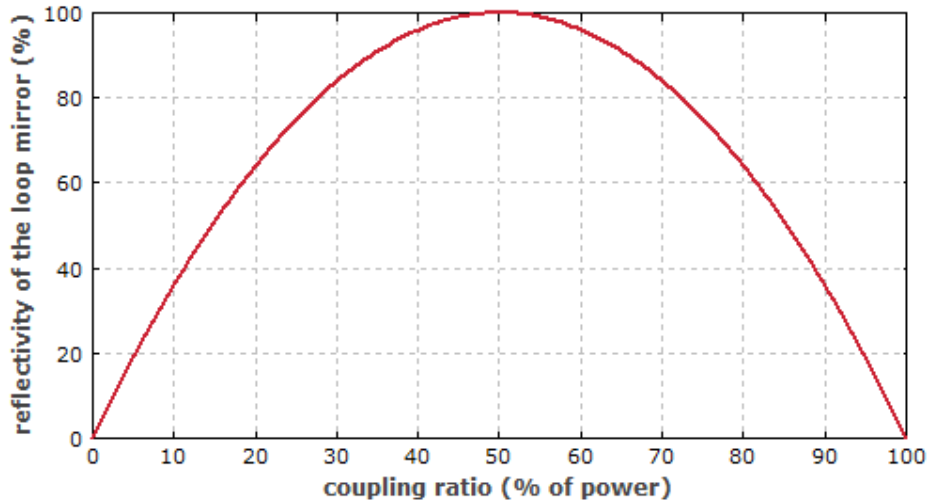


Figure 1.10: Power reflectivity of a linear fiber loop mirror as a function of the coupling ratio of the used fiber coupler [152].

are affected such that a power-dependent fraction of the input light reaches the output port. This setup acts like the combination of some laser gain with a saturable absorber, favoring the peak of a circulating pulse against the low-power background light. This artificial saturable absorber generates a single pulse circulating in the resonator and thus a pulse train emitted at the lower left port [152].

One common configuration using NALMs for the production of pulses in fiber lasers is the known as Figure-of-Eight Laser (F8L), first reported in the early 1990s, consisting on a NALM coupled to a main fiber resonator through a four ports coupler in an *eight* shape [153, 154]. The extreme simplicity of such a configuration together with its capability of producing ultra-short pulses in the range of the picosecond or lower represent one of the main advantages of F8Ls. Typically, F8Ls setups count with polarization controllers to trigger the pulsed emission by nonlinear polarization rotation [155–158] although also polarization maintaining versions in rare-earth-doped F8Ls with external light pumping have been developed producing pulses as short as 427 fs and with a tunable repetition rate ranging between 16 and 32 MHz [159]. Furthermore, SOA-based F8Ls have also been recently developed operating at 1.06  $\mu\text{m}$ , with pulses of 29 ps duration and reaching repetition frequencies up to 12 GHz which can be selected by changing the bias current in the SOA [160].

### 1.4.3 Pulses as localized structures in semiconductor lasers

One of the hottest topics in nonlinear optics during the last decades, and still today, is related to the spatial and temporal localization of light [161, 162]. The control of light and pattern formation constitutes a highly interesting research field due to their perspective of application for the encoding and treating of optical information in real telecommunication systems [163]. In the origins, the efforts were placed on the research of spatial pattern formation in the structure of the electromagnetic field in the transverse sections of broad-area radiation beams interacting with nonlinear media but unfortunately, although such optical patterns displayed an array of light spots, these intensity peaks could not be independently manipulated given the strong correlation with one another that they exhibited [164].

Thus, the challenge of the individual addressing of light spots became feasible using a kind of amazing entities known as Localized Structures (LS) appearing in many nonlinear dynamical systems in the fields of hydrodynamics [165], chemistry [166] or gas discharge systems [167] to cite just a few of them. LS show the property of bistability or, in other words, the coexistence with a homogeneous state and a patterned stationary state for the same set of parameters values. As a consequence, LS are intermediate between these two states and they can coincide either with the first or the second one. LS are also often referred to as solitary waves or solitons –wave packets maintaining their shape while propagating at a constant velocity– and their properties largely define the behavior of the nonlinear system under study. Traditionally, the emphasis was placed on LS appearing in conservative systems, but it has been lately demonstrated that dissipative LS can also arise in non-conservative systems as a consequence of the equilibrium between gain, loss, linear and nonlinear effects, and resulting of great attraction for specific research due to their practical applications [168]. Although purely dissipative LS are usually related to Dissipative Solitons (DS) [169, 170], it is worth noting that the link between LS and DS should be used with care as it is often a source of misunderstandings given their different nature and physical properties. For example, DS are not required to feature the property of individual addressability while LS are operatively defined based on it as it is explained below [171].

By definition, a light spot must exhibit several properties to be assessed as a LS. In the first place, they must have a specific shape which does not depend on the boundary conditions but on the nonlinearity in the medium. Second, they must be writable and erasable individually and, third, they may be written at random positions in the medium (see [172] and references therein). Furthermore, an interesting feature of LS is that, once that they are *written*, for example by the injection of a laser pulse, they can be also *erased* by injecting another pulse in the location where the previous

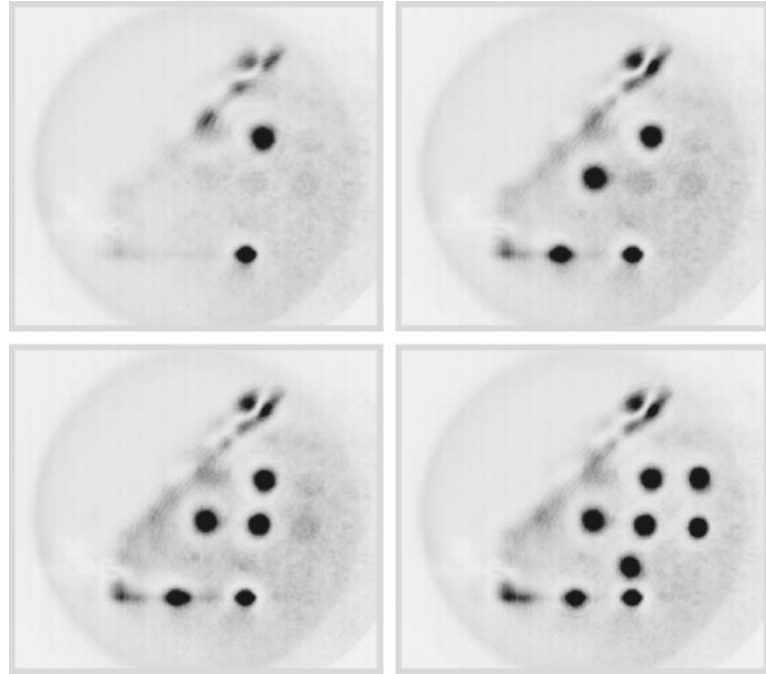


Figure 1.11: Near field of a VCSEL in which different LS have been independently written as binary pixels using a phase mask at different current values (from left to right and top to bottom,  $I_{bias} = 557, 563, 565, 567$  mA) [175].

LS laid as long as the injected perturbation overcomes a certain threshold [173, 174]. Another feature presented by LS is their ability to drift across the transverse section of an optical system under the action of an amplitude or phase gradient causing the LS to shift to the closest local maximum of the modulated profile [164]. All these promising features relatives to the control of LS confirm their potential applications in the optical treatment of the information and, in fact, they have already been straightforwardly manipulated and used as means of encoding information in the transverse plane of optical systems creating reconfigurable arrays of LS which act as binary pixels as shown in Figure 1.11 [175, 176].

Thus, in particular, in the field of telecommunications, the control of optical LS is of fundamental importance for applications and the switch-on and switch-off duration of LS is an essential parameter to control as it determines the speed at which information can be written and processed. In this sense, semiconductor lasers emerge as

appealing devices to achieve such goal given their rapid response which allows for the fast manipulations of LS [177]. For these reasons, the switching of LS in semiconductor devices has been –and still is– the subject of several theoretical and experimental studies which propose different models and techniques depending on the system under consideration [174, 178].

From the point of view of dynamics, it has been shown in one dimension systems that LS are formed by fronts connecting two coexisting solutions, this is to say, the previously mentioned homogeneous and patterned states [179, 180]. More precisely, these fronts are homoclinic orbit passing close to the pattern states and converging back to the homogeneous state. When a single-peak LS exist, also more complex states with two-peaks, three-peaks and N-peaks of LS may exist and, accordingly, the bifurcation diagram of localized states results in two transcendental curves (one for LS with an even number of peaks, the second for LS with an odd number of peaks) upraising in intensity with the number of peaks of the LS and zig-zagging within a common parameter range [181]. This peculiar bifurcation diagram has been named homoclinic snaking and describes the coexistence of almost an infinity of localized structures [182], each one formed by stable fronts linking arbitrary portions of the pattern solution with the homogeneous one [179, 183, 184]. It is precisely when the pattern becomes fully decomposable in each period when LS can be considered as independent units of the pattern [171, 185].

On the other hand, when two dimensions systems are considered, localized states can form in spatially extended media having a large aspect ratio and this idea have also been extended to the case of delayed dynamical systems. For semiconductor lasers, this can be achieved by placing a mirror in front of the laser causing light to be reinjected into the laser after a while. Theoretically, this is modeled by the addition of term of delay representing this optical reinjection delayed into the nonlinear medium which, from the dynamical point of view, can be considered as a nonlinear node. When the nonlinear node is located close to a supercritical Hopf bifurcation, it can produce convective type instabilities in the presence of delayed feedback [186] while, in the vicinity of a saddle-node on a circle bifurcation, both elastic collisions as well as the interaction of repulsive and attractive forces have been experimentally assessed [178, 187, 188]. However, a general theory describing the formation of LS in two-dimensional systems has not been yet developed [181] although numerical simulations have shown that in 2D systems LS bifurcation could be described in a very similar way to the homoclinic snaking [189].

Even if some general questions concerning LS remain open, theoretical and experimental studies are in tirelessly development and intensive studies are performed on laser systems. In this sense, and as previously mentioned, a great amount of these

research efforts are placed on semiconductors laser as they represent one of the most important goals in the generation of LS provided their potential applications to information technology [190]. Among semiconductor-based optical systems, LS can be accomplished in a multitude of ways and the presence of optical localized states in several optical systems has been proved experimentally, including those where an external forcing is applied [191] or those containing a saturable absorber [192]. Spatial LS have been observed in the transverse section of broad-area VCSELs injected by a coherent electromagnetic field [191], which are commonly named as *cavity solitons* [193]. Moreover, spatial LS have been observed in laser systems without requiring the presence of an injected field but, instead, arising from spontaneous emission noise [192, 194] and they are referred to as *laser solitons*. As they appear in a phase invariant system, their dynamical ingredient, properties, and formation mechanism are different from the ones of cavity solitons appearing in driven resonator [195, 196].

More recent works have also extended the concept of LS from the spatial domain to the time domain (see [197] and references therein). In this case, the large aspect ratio of the system refers to timescales for the active materials which are much shorter than the cavity round-trip time [178] or, in other words, to the propagation direction of the electromagnetic field where LS appear in the form of pulses of light. The generation of temporal LS in VCSEL-based systems mounted in an external cavity configuration through the rotation of the polarization or mode-locking by coupling to an RSAM has been demonstrated. For the last case, while the building of a cavity round-trip shorter than the gain recovery time of the system allows to achieve the emission of a standard passive ML with a pulse per round-trip (or harmonic mode-locking if either the cavity length or electrical pump is increased) showing a single pulse per round-trip (fundamental mode-locking) [138].

However, if the cavity is modified making the round-trip time much longer than the gain recovery of the semiconductor material, the bifurcation scenario is modified and the ML solution becomes subcritical leading to the coexistence of this solution with the zero-emission one (off state). In this case, the fundamental ML solution is stable and the maximal order harmonic mode-locked solution becomes fully decomposable allowing the existence of a large number of pulsing solutions with different number and arrangement of pulses per round-trip which can be set on or off for the same set of parameter values. Such a scheme has shown the capability to store information in the cavity with a bit rate limited of approximately 1 Gb/s [138].

Nevertheless, both the control on the repetition rate in combs of LS as their arbitrary addressing is a demanding task not only for the complex technical methods that it involves like fast detection, microwave signal processing, and fast cavity actuation, or novel approaches such as pulsed [198, 199] or counter-propagating pumping [200], or

heterodyning with coupled microresonators [201] but, even from a more basic aspect, due to the appearing of small scale material defects during the fabrication process of semiconductor materials. These defects are caused by local spatial variations of the semiconductor resonator characteristics thickness, electrical or optical properties or optical gain [202, 203] which induce the spontaneous formation of LS at undesired positions as well as their trapping or annihilation [175, 204, 205].

Still, good control of LS has been observed in electrically biased broad-area VCSELs below the threshold [191], optically pumped VCSELs [206], and in electrically biased VCSELs above the threshold by a rather fine control in terms of the detuning between the VCSEL cavity resonance and the injected field frequency [163]. The LS switching time in these devices has been also characterized showing time responses in the order of the nanosecond or lower [207, 208]. Also, a single-mode VCSEL enclosed in a polarization-sensitive double external cavity has demonstrated the capability to emit vectorial LS consisting in time-localized rotations of the polarization orientation of the light which have been controlled by exploiting the two different times of flight as well as the polarization selectivity of the cavity [209].

Besides VCSELs, passively modelocked fiber lasers have revealed as outstanding devices to research both the generation as the dynamics of LS by means of common mode-locked techniques like the use of SESAM [210, 211], Nonlinear Polarization Rotation (NPR) [107, 212], Nonlinear Optical Loop Mirror (NOLM) [213], and Nonlinear Amplifying Loop Mirror (NALM) [153]. The high peak power shown by passively mode-lock lasers is a useful platform to investigate the nonlinear dynamics of mode-locked pulses. Normally, a single mode-locked pulse propagates in the cavity of fiber lasers although multiple pulses may also emerge in the cavity when the pumping is high enough [214–216] allowing the research on the evolution and interaction among the multi-LS regime via skillfully selecting the cavity parameters [217, 218]. The emission of multiple LS has been observed under different fiber laser cavity conditions being possible to find them regularly spaced in the laser cavity as in the harmonic mode-locking regime [219–221], forming cluster of pulses tightly spaced [222, 223], randomly spaced [224] and also as a rain of LS [225, 226]. Although the previously reported multi-LS operation generally focused on the scalar characteristics, the vectorial nature of LS can also be considered when they propagate in single-mode fiber due to their birefringence as they allow the transmission of the two orthogonal polarization modes and showing complicated polarization dynamics [227–240]. Therefore, in those cases in which the evolution of polarization degree of freedom needs to be minimized, polarization-maintaining fibers should be used as they keep the polarization state of light that transmits along the principal axes of the fiber.

Also, fiber lasers under a F8L configuration have been suggested for the research of

various types of LS emitted based on a NALM or a NOLM [241]. The use of intra-cavity PC under this F8L scheme offers one more degree of freedom to adjust the laser emission of LS in comparison to the mode-locking fiber lasers based on a SESAM [242, 243], and it allows the generation of LS which are able to show both a locked polarization state as a rotating polarization state, as it is shown in Figure 1.12 [244]. Hence, according to all what has been previously exposed, pulsed fiber lasers can be considered as an excellent platform in the research of the multiple physical features of different types of LS as well as a useful tool for the achievement of the goal of encoding information in optical telecommunication systems.

## **1.5 Overview of this thesis**

The aim of this thesis is the experimental generation of ultrashort pulses by means of semiconductor lasers, of type VCSEL and fibered, that can be applied to improve the performance of LiDAR systems.

Hence, Chapter 2 is devoted to the generation of pulses by PML of a VCSEL coupled with a saturable absorber mirror in an external cavity. It is shown that the number and location of the train of pulses can be controlled electrically by modulation of the bias current of the laser.

Chapter 3 shows the adaptation of the experimental scheme VCSEL–saturable absorber in which light propagates through the air to a unidirectional fiber ring laser using a SOA as the gain medium and a fibered saturable absorber mirror. A study on the effects of varying the polarization reinjection on the emission of the laser is performed.

Chapter 4 presents the studies accomplished on an extremely simple and self-starting all-polarization maintaining SOA-based F8L. The setup is described and the pulsed emission is characterized in terms of the repetition frequencies and pulse width achieved.

Chapter 5 demonstrates the nature as localized structures of the pulses emitted by the mentioned F8L. It is shown that the optical reinjection of a single of the generated pulses allows the erasure of any other pulse on the train and makes possible to modify at will the original pulse train and generate an arbitrary pattern of bits.

Finally, Chapter 6 summarizes the procedures followed throughout the thesis and highlights the most relevant theoretical and experimental results.

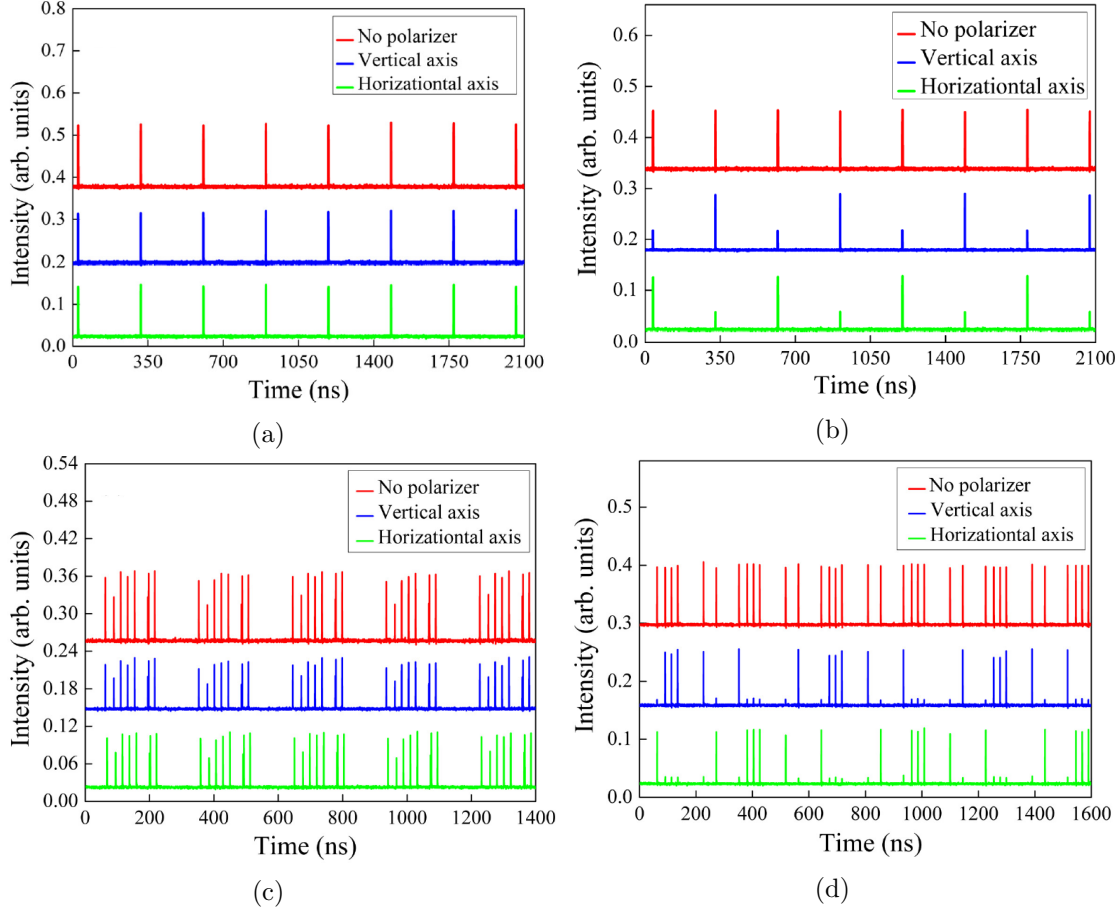


Figure 1.12: Localized structures generated by a F8L containing a polarization controller which presents different pulsing states of locked and rotating polarization. a) Fundamental emission of polarization locked LS. b) Fundamental emission of polarization rotating LS. c) Random static distribution of LS in the polarization locked regime. d) Random static distribution of LS in the polarization rotating regime [244].



## Chapter 2

# Generation and control of pulses in a passively mode-locked VCSEL in an external cavity

The present chapter is part of this thesis as a result of the collaboration between the Institut Non Linéaire de Nice–Sophia Antipolis (INLN) and the University of the Balearic Islands (UIB). Based on previous results from such a collaboration on the generation of ultrashort pulses by means of a VCSEL and a Resonant Saturable Absorber Mirror (RSAM) in an external cavity configuration, the contribution of the work presented in this chapter of the thesis consists in the implementation of a temporal modulation on the VCSEL bias current allowing to achieve the stabilization of the mentioned system, the controlled nucleation of pulses and the manipulation of the number of pulses as well as the control of their temporal localization within the round-trip.

The present chapter describes the results obtained after a three months internship in the INLN which were published in the article “Control and generation of localized pulses in a passively mode-locked VCSEL”, authored by Mathias Marconi, Julien Javaloyes, Patrice Camelin, **Daniel Chaparro**, Massimo Giudici and Salvador Balle in the Journal of Selected Topics of Quantum Electronics, volume 21, issue 6, pages 30-39 in December 2015 (Article number 1101210, DOI: 10.1109/JSTQE.2015.2435895).  
©2015 IEEE.

### 2.1 Antecedents to the study

As expounded in the general introduction of this work, VCSELs allows for the generation of pulses by PML when used in external cavities configurations. Some of the common techniques used for this purpose include the exploitation of their polarization degree of freedom or the presence of saturable absorbers in the cavity.

Concerning to the first technique, although the difficulties of controlling the polarization of VCSELs due to the isotropy given by their symmetry around the cavity axis is widely known, procedures such as the injection of external optical feedback have

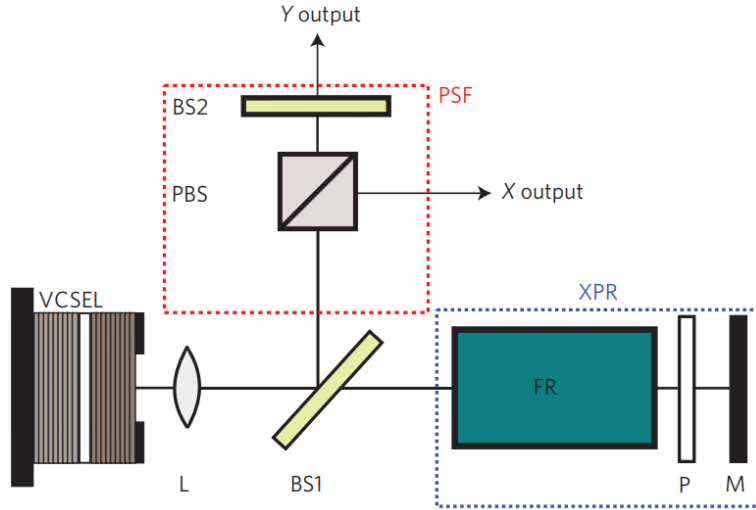


Figure 2.1: Experimental setup for the implementation of Crossed Polarization Re-injection (XPR) and Polarization Sensitive Optical Feedback (PSF) in a VCSEL emitting at 850 nm. L: lens, BS: beam splitter, PBS: polarizing beam splitter, FR: Faraday rotator, P: polarizer, M: mirror [209].

demonstrated the capability to pin the polarization of these devices [245]. However, the usual presence of two polarization modes with orthogonal polarizations allows for the polarization switching between them and the obtaining of complex polarization dynamics, waveforms ranging from square waves to sinusoidal oscillations or even optical pulses when optical feedback or optical injection are applied [246–248].

Marconi et al. have demonstrated the bistable coexistence of two orthogonal linear polarization states in a VCSEL emitting at a wavelength of 850 nm and its all-optical switching, control and buffering by means of both Crossed Polarization Reinjection (XPR), Polarization Selective Optical Feedback (PSF) and the injection of external laser beam pulses [249]. Furthermore, when the VCSEL is simultaneously subjected to both XPR and PSF (see Figure 2.1) at high enough feedback levels, it is possible to achieve the antiphase oscillations of the two polarization components leading to a robust square-wave signal which is weakly affected by parameters changes [250]. Even more interesting is the capability of such a polarization dynamics in the VCSEL to generate two antiphase trains of passively mode-locked independent optical pulses presenting a FWHM of 50 ps which have been identified as vectorial dissipative solitons [209]. Each of these two pulse trains corresponds to one of the two orthogonal po-

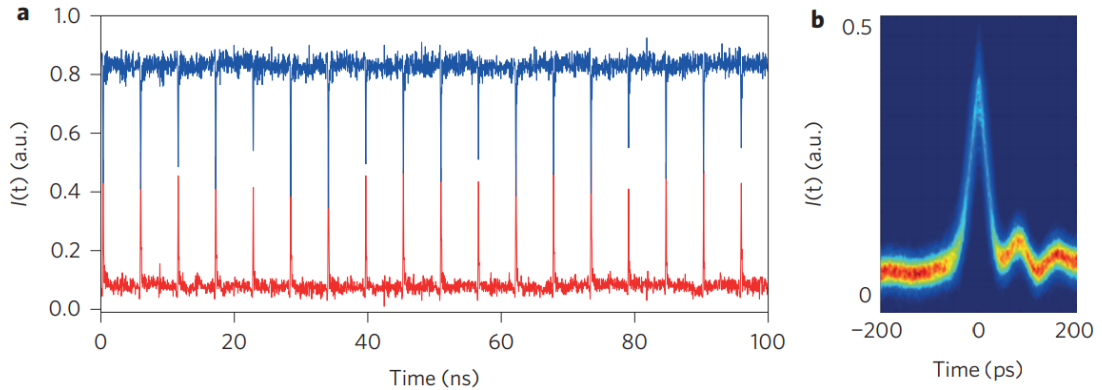


Figure 2.2: Pulsed emission of the VCSEL due to the polarization dynamics originated from XPR and PSF. a) Time traces of each of the two polarization components. b) Persistency diagram after the superposition of  $18 \cdot 10^3$  pulses showing a FWHM of 50 ps. Adapted from [209].

larizations present in the VCSEL and their temporal traces consists in bright or dark pulses depending on the particular polarization component observed (see Figure 2.2). The representation of these time traces can be realized in the so-called *space-time* diagrams consisting in a folding of the temporal trace at intervals equal to the round-trip time [251] which allows to assess the independence of the pulses to each others by tracking the variations on their positions under pseudo-time and pseudo-time variables (see Figure 2.3). Under certain conditions, some pulses may interact forming a bound state or *molecule*. Although these bound pulses are not independent of each other anymore, the global molecule remains independent from other individual pulses or molecules at least until a new interaction occurs. Moreover, the spontaneous nucleation of pulses has been experimentally observed for such a system which suggests the possibility of their individual addressing. Unfortunately, this spontaneous nucleation remains uncontrolled as it usually occurs by mechanical perturbations of the optical table. Hence, achieving an accurate and efficient control on the activation and deactivation of these independent pulses at will constitutes a major aim for the construction of an arbitrary pulse pattern generator which would result greatly useful for LiDAR ranging techniques such as the RM-CW LiDAR.

A second manner for generating mode-locked pulses using a VCSEL in external-cavity configuration supports on the presence of saturable absorber materials in the experimental setup which, among others, offers the benefit of the passive generation of much shorter pulses and higher peak powers. Under this scheme, pulse widths in the

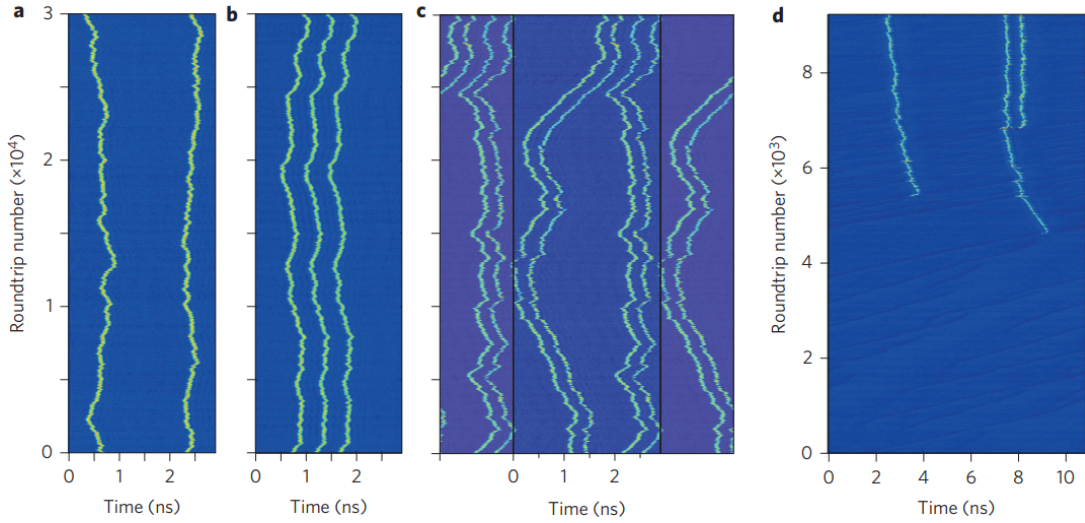


Figure 2.3: Space–time diagrams of different coexisting situations. a) Two independent pulses. b) 3 bound pulses. c) Two independent molecules containing 2 pulses each interacting to form a bound state of 4 pulses. d) Spontaneous nucleation of pulses [209].

order of the femtosecond with peak powers in the kilowatt range and repetition rates around the gigahertz have been achieved [252]. Marconi et al. have also demonstrated that a broad-area VCSEL with a wavelength emission of 980 nm is able to generate trains of pulses when coupled to an RSAM for the same wavelength in an external cavity configuration [253]. In this case, the particular placement at which the VCSEL and the RSAM need to be placed with respect each other for the emission of pulses is of substantial importance and corresponds to a very particular imaging condition in which the RSAM is placed in the Fourier transform plane of the near field of the VCSEL. Hence, after a round-trip in the cavity, the VCSEL near field profile is imaged onto itself but inverted. Such a configuration leads to the generation of two opposed tilted wave planes circulating within the external cavity which are tightly focused on the surface of the RSAM allowing its saturation and, as a consequence, the modulation of the losses in the cavity and the opening of a net gain window for the amplification of the pulses. Each of these two tilted waves generates a pulse train with a pulse delay given by the cavity round-trip so the presence of both of them in the cavity gives, as a result, a pulse train of twice the cavity round-trip (see Figure 2.4). The properties of this so-generated pulses show a width of less than 12 ps of FWHM –almost five times

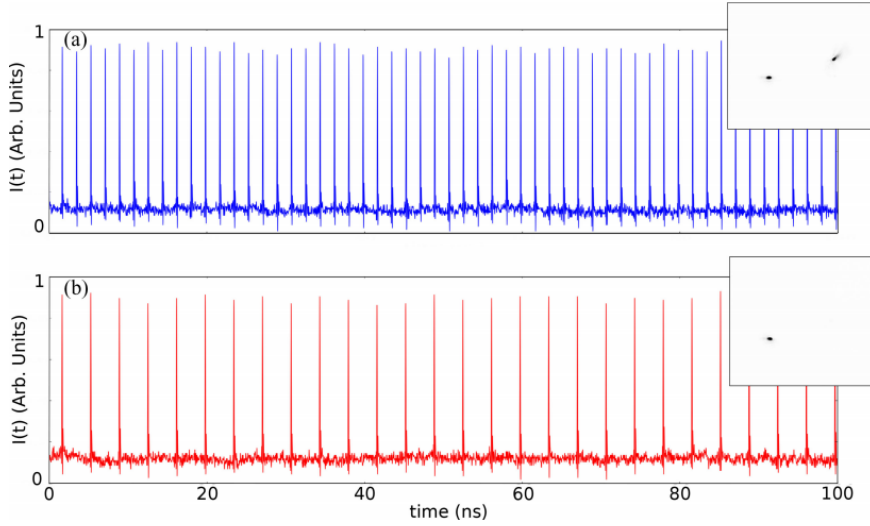


Figure 2.4: Temporal signal obtained when detecting simultaneously the two spots (panel a) of the far-field emission of the VCSEL or a single spot (panel b). The insets represent the detected spots in the far-field [253]. ©2014 IEEE.

shorter than the previous pulses generated by polarization dynamics – and a peak power of approximately 1 W. However, such a configuration is extremely sensitive with mechanical perturbations being possible to turn the pulses on or off by gently hitting the optical table.

Under this VCSEL–RSAM configuration, it has also been shown that the length of the cavity does not only have the straightforward effect of increasing the round-trip time of the pulses but, moreover, have a strong impact on the pulsation dynamics. While for short cavities the system’s pulses in the usual regime of PML, when the cavity length is increased above a certain limit, the pulses become independent, as occurred in the XPR–PSF system. In this situation, the system becomes multistable and a multiplicity of emission states with a different pulse number and arrangement coexist, from 1 up to 19 pulses per round-trip (see Figure 2.5) [138]. The origin of the independence of these pulses has been explained by the simulation of the system according to a generic delayed differential equation model [254] and the representation of bifurcation diagrams for different cavity lengths (see Figure 2.6). For very short cavities, the fundamental mode-locked regime –with a single pulse per round-trip and a round-trip time corresponding to the double of the cavity length– exists only above

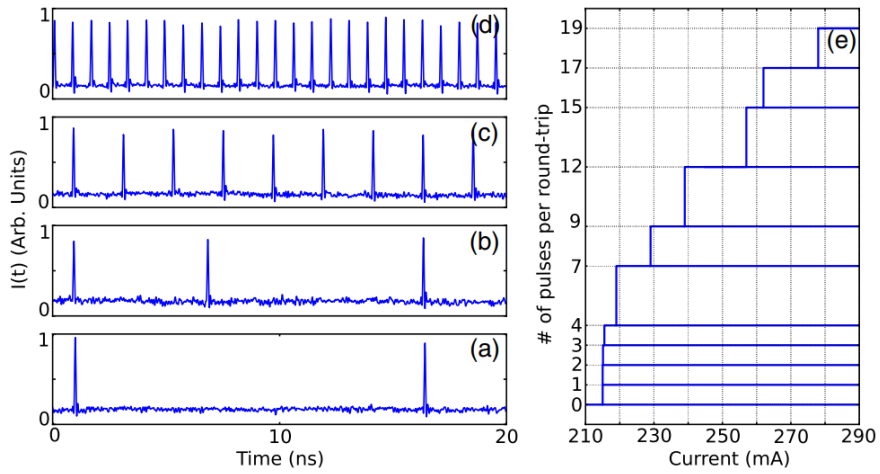


Figure 2.5: From a) to d), coexisting time traces with different pulse number. e): bifurcation diagram for the number of pulses per round-trip [138].

the bifurcation point. If the cavity length is increased, a folding of the bifurcation branch occurs and the fundamental state coexists with the CW emission what makes possible the existence of the fundamental state below the bifurcation point. For even longer cavities, the folding is even more pronounced such that not only the fundamental state coexists even with the off state and the system may become multistable with several possibilities of coexistence among states with different number of pulses [138]. This condition of independence of the pulses, as mentioned when the results from the XPR-PSF system were described, is of great interest in the research community as they constitute a basis over which it would be possible the construction of an arbitrary pattern generator with potential applications and improvements in many fields, including LiDAR.

At this point, the contribution of the work presented in this chapter of the thesis to the scenario presented before on the system VCSEL-RSAM consists in the implementation of a temporal modulation on the VCSEL bias current to achieve the controlled nucleation of pulses and the manipulation of the number of pulses and their positions within the round-trip. This results will be compared with simulations obtained from the general delayed differential equation model used for this setup in previous studies.

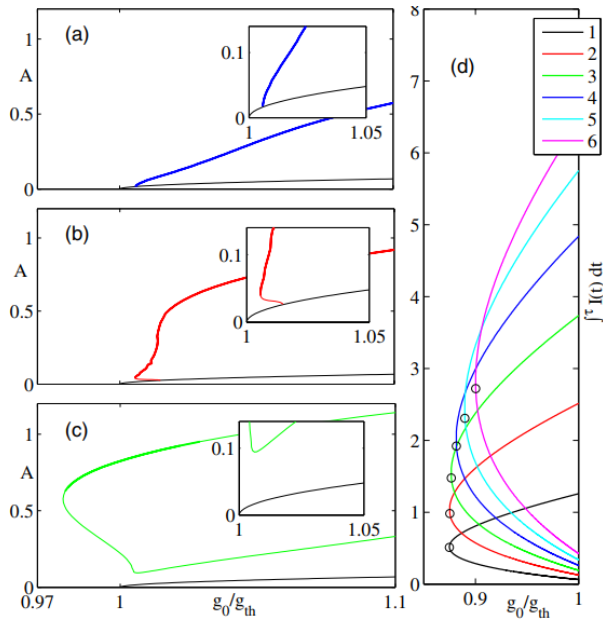


Figure 2.6: Bifurcation scenario as a function of the gain for different values of the delay: a)  $\tau = 1.2\Gamma^{-1}$ , (b)  $\tau = 2\Gamma^{-1}$  and (c)  $\tau = 4\Gamma^{-1}$ . (d) folding of several PML solutions with different number of equispaced pulses per round-trip for  $\tau = 16\Gamma^{-1}$  [138].

## 2.2 Description of the experimental setup

The setup used for the application of the modulation is that one used by Marconi et al. in the studies previously mentioned [138, 253] (schematically shown in Figure 2.7). The main two constituents are the VCSEL and the RSAM which are coupled in a Fabry-Pérot configuration cavity. The VCSEL is a broad-area type of 200  $\mu\text{m}$ , from ULM Photonics, emitting at a wavelength of 980 nm with the temperature managed by means of a temperature controller and pumped by electrical current.

By increasing the current of the solitary VCSEL, the threshold appears around  $I_{\text{sth}} = 380$  mA, where a ring-shaped lasing begins to emerge from the contour of the device up to approximately  $I = 850$  mA. Concerning to the RSAM, from BATOP GmbH, it presents dimensions of 4 x 4  $\text{mm}^2$  and its reflectivity varies from 1% when unsaturated, up to 60% when it is saturated. The RSAM shows the resonant wavelength also at 980 nm with a FWHM of 16 nm (while the VCSEL shows a peak with 1 nm of FWHM for its resonance) and it is thermally stabilized through a second

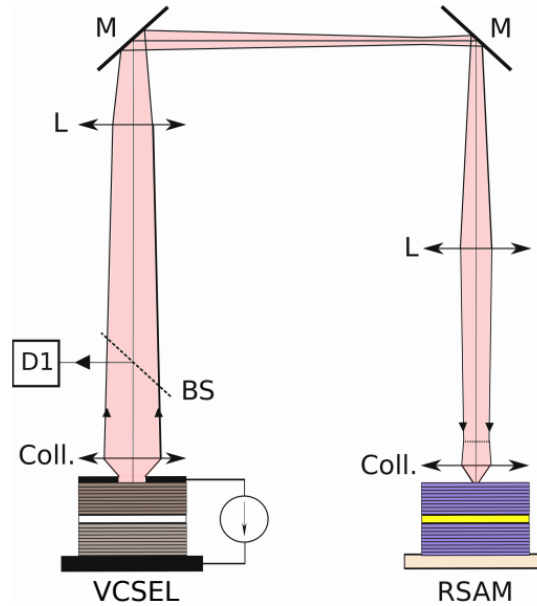


Figure 2.7: Experimental setup for the passive mode-locking of pulses through the coupling of a VCSEL and an RSAM. Coll.: Aspheric lens, L: lens, BS: beam splitter, M: mirror, D1: detection branch. ©2015 IEEE.

temperature controller. The variation of its temperature in a range from 10°C to 50°C allows for the fine-tuning of the resonant wavelength in a range of 3 nm [255].

The system also contains two aspherical lenses with a numerical aperture of 0.68 which are placed in front of both devices in order to collimate the output light from the VCSEL and focus the incoming light to the surface of the RSAM. In order to make a long enough external cavity allowing for the emission of independent pulses, light is deflected by two reflecting mirrors and two convergent lenses are placed to fulfill the required Fourier imaging condition. Under this situation, the total cavity length is 2.25 meters which corresponds to a round-trip for the pulses of 15 ns or, in terms of repetition frequencies, 66.6 MHz.

Furthermore, a beam splitter is located in front of the VCSEL for the transmission of a 90% of the light towards the RSAM and the extraction of a 10% of the light out of the cavity which is used for monitorization and detection. The monitorization is performed by two CCD cameras for the recording of both the near and far field profiles of the VCSEL while the former detection of the pulses is performed by a 10 GHz detector and a 33 GHz oscilloscope.

## 2.3 Pulse addressing and multi-pulse pattern generation

As mentioned before, achieving high accuracy on the control of the pulses is essential for the development of an arbitrary pulse pattern generator useful for LiDAR applications. Better control on the pulses generated by the VCSEL–RSAM system might be accomplished by a proper perturbation of the bias current of the VCSEL. Nevertheless, some restrictions arise related to the limited frequency modulation which can be imposed given by the low frequency cut-off in the response of the VCSEL to a modulated signal when coupled to a bias-T (below 300 MHz for the VCSEL used here) and rendering inefficient the use of electrical pulses for this purpose due to the long rise time of the perturbation.

However, it is observed the possibility of activating pulses by imposing to the VCSEL a sinusoidal modulation if two conditions are fulfilled. First, the modulation signal applied to the VCSEL has to present a frequency equal to the cavity round-trip and, second, the amplitude of such a modulation has to be comprised between a low value, for which only the off solution is shown, and a high value, where the maximum number of 19 pulses per round-trip appears. If these two requirements are satisfied, whenever the sinusoidal modulation is activated, a section of this completely filled pattern of pulses emerges and is repeated according to the imposed modulation frequency derived from the cavity round-trip. When the modulation is deactivated, some of the pulses may also turn off and the previously created pattern evolves towards a new pattern containing one, two or more pulses per round-trip.

The experimental acquisition illustrating such behavior for the system can be observed in Figure 2.8. For obtaining such experimental data, the VCSEL is initially in the off pulsed state although it is biased at a DC current of  $I = 215$  mA for which, according to Figure 2.5, only one independent pulse per round-trip would appear on the temporal trace. At this point, the sinusoidal modulation with an amplitude peak-to-peak of 460 mA is activated and six independent pulses are created in the temporal trace with an interpulse delay of 800 ps which corresponds to the pulse separation of the 19 pulse pattern. Next, when the modulation is turned off (see Figure 2.5e), the DC value of  $I = 215$  mA is too low for supporting the presence of the six localized pulses and the system relaxes towards a state with a more reduced number of pulse per period.

The exact number of surviving pulses depends on the DC value of the bias current and on the size of the filled pattern excited. For the case presented here, as the DC value  $I = 215$  mA is able to allow the existence of a single pulse per round-trip in a stable way, only one pulse of the six previously generated remains active and this situation persists until the system is turned off or the parameters are varied.

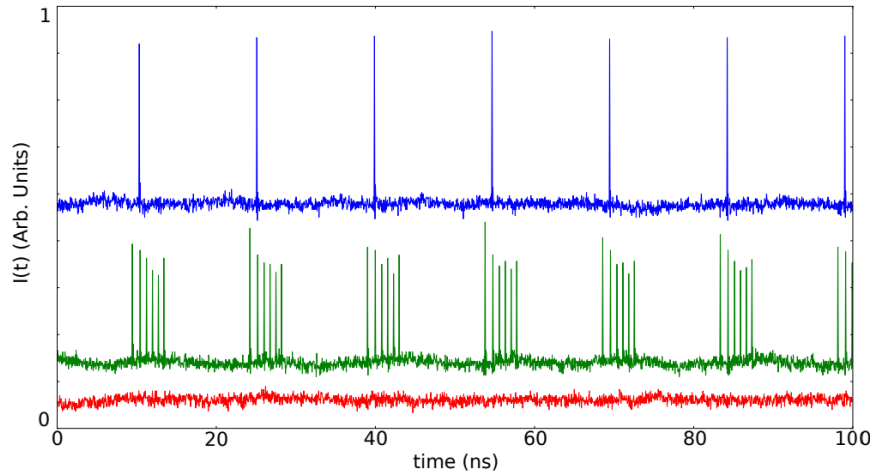


Figure 2.8: Time traces showing the experimental process for pulse generation via current modulation. First, the laser is in the off state without modulation (red, bottom line) and  $I = 215$  mA. Then, modulation is applied with a peak-to-peak amplitude of 460 mA and 6 pulses appear close to the peak of the modulation (green middle line). When we switch-off current modulation, only a single pulse remains in the cavity (blue, top line).  
©2015 IEEE.

The results presented above, settle the current modulation as a feasible method for the generation of a pack of independent pulses. The number of excited pulses appearing in the temporal trace is determined by the DC value of the bias current together with the amplitude of the modulation as they establish the gating time interval during which the system is driven within the state of maximum number of pulses. It is important to note that, in order to achieve a stable pulse train, the modulation frequency imposed to the bias current needs to be carefully set to the inverse to the cavity round-trip as mismatches exceeding the 10 kHz cause the loss of the signal.

Hence, taking the previous remarks under consideration, this technique has been applied for the implementation of a pulse pattern generator and five pulses can be consecutively written by increasing the depth of the peak-to-peak modulation amplitude (see Figure 2.9). With the system biased in the off pulsed state at  $I = 210$  mA, a single first pulse appears on the temporal trace after imposing a value of the modulation amplitude of 297 mA. Successive pulses are created while increasing the modulation amplitude up to a value of 454 mA where a fifth pulse appears completing a five pulses

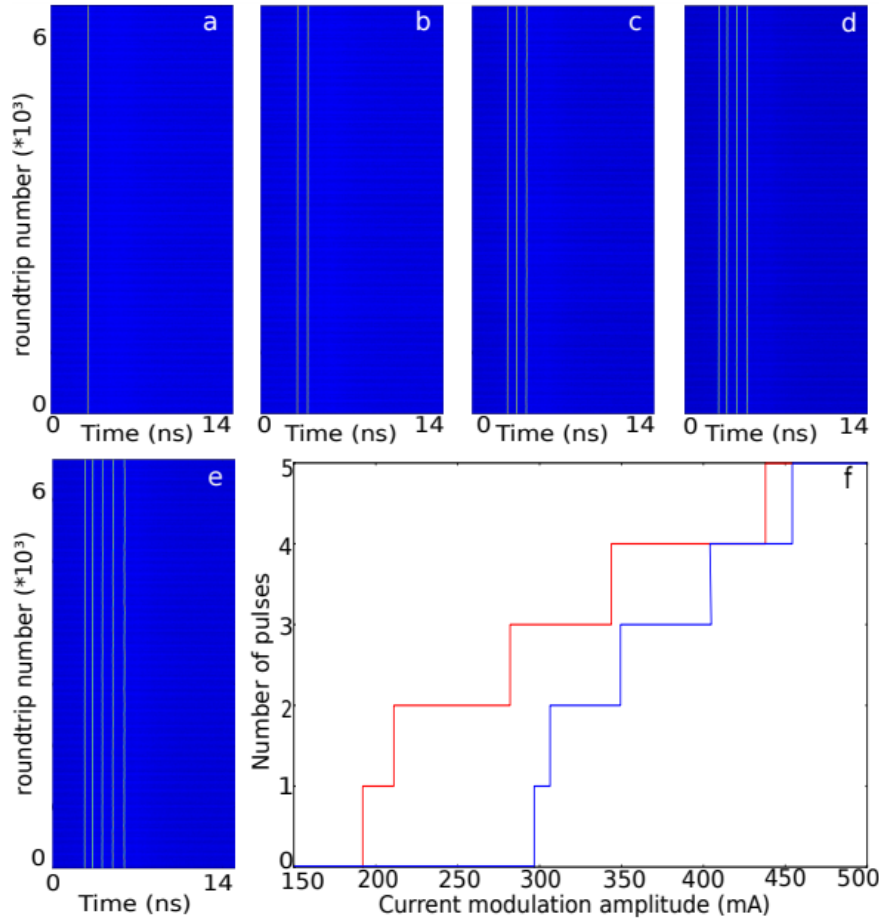


Figure 2.9: Addressing of independent pulses by applying a sinusoidal modulation to the bias current of the VCSEL. The number of pulses is incremented by one when the peak-to-peak amplitude of the modulation is increased to the values a) 297 mA, b) 306 mA, c) 349 mA, d) 405 mA and e) 454 mA. f) Diagram of the pulse number as a function of the modulation. The lower (blue) curve corresponds to an increasing amplitude while another sequence appears when decreasing the modulation amplitude in the upper (red) curve. The modulation value at which transition from  $N-1$  pulses to  $N$  pulses happens is slightly different with respect to the modulation value at which the inverse transition from  $N$  pulses to  $N-1$  occurs, thus indicating multistability. ©2015 IEEE.

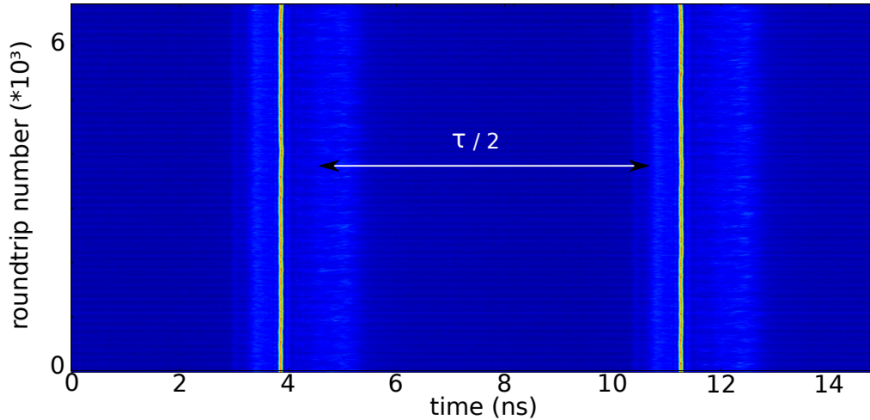


Figure 2.10: Writing the pulse is possible even when the modulation period is set to half the round-trip. The bias current is  $I = 210$  mA, and the modulation amplitude 297 mA. ©2015 IEEE.

pack and remaining stable for an indefinite time. It is equally possible to erase the created pulses by reducing the modulation depth, as shown in Figure 2.9f), although some degree of hysteresis is observed and unveils the existent multistability between the previous situations.

Furthermore, starting again from the off state, if the frequency of the sinusoidal modulating signal is doubled, it allows for the simultaneous activation of a state with two pulses within a round-trip separated by half a round-trip (see Figure 2.10). From this, the future generation of more elaborated pulse patterns could be expected which may include the use of more complex modulation although their wider spectral band will require overcoming the limitation in the electrical coupling in the VCSEL. As a matter of fact, the proof-of-principles demonstrated by the set of results obtained in this study have recently served as a trampoline for a more detailed study on the tweezing and movement of these independent pulses based on the use of a more complex modulation by squared, triangular or pulsed signals [256].

## 2.4 Theoretical evaluation of the generated pattern

A theoretical insight for the assessing of these experimental results has been performed by the co-authors of the article. As previous studies have demonstrated [138], a valid model for the description of the setup used here consists on a delay differential equation

model which comprises both the steady and the pulsating regime and generalizes the Haus' model [254].

The particularization of this model for the case under study here includes a term accounting for the modulation of the gain. Hence, the model reads:

$$\frac{\dot{A}}{\gamma} = \sqrt{\kappa} \exp \left[ \frac{(1 - i\alpha) G_\tau - (1 - i\beta) Q_\tau}{2} \right] A_\tau - A, \quad (2.1)$$

$$\dot{G} = g_0 + \Delta g \sin \left( \frac{2\pi t}{\tau_m} \right) - \Gamma G - e^{-Q} (e^G - 1) |A|^2, \quad (2.2)$$

$$\dot{Q} = q_0 - Q - s (1 - e^{-Q}) |A|^2. \quad (2.3)$$

In this set of equations,  $A$  represents the amplitude of the optical field,  $G$  the gain provided by the semiconductor material (the subscript  $\tau$  indicates a delayed value of the variable  $x_t = (x - \tau)$ ),  $Q$  the losses related to the saturable absorber,  $\alpha$  and  $\beta$  stand for the linewidth enhancement factor of the gain and absorber sections respectively,  $\kappa$  is the fraction of the power remaining in the cavity after each round-trip,  $g_0$  is the pumping rate,  $\Delta g$  and  $\tau_m$  are the amplitude and the period of the modulation of the gain,  $\Gamma$  is the gain recovery rate,  $q_0$  is the value of the unsaturated losses which determines the modulation depth of the saturable absorber,  $s$  is the ratio of the saturation energies of the gain and of the saturable absorber sections and  $\gamma$  is the bandwidth of the spectral filter. In the model, the time has been normalized to the saturable absorber recovery time.

Although within the framework of this simplified model it is difficult to relate precisely the parameter values to the experiment for obtaining a quantitative assessment of the results, still a qualitative explanation can be provided by imposing numerical values to the previous parameters which are similar to the experimental working conditions. Hence, the extraction of the 20% of the light at each round-trip (due to the double pass through the 10% beam splitter) is represented by the parameter value  $\kappa = 0.8$ . By setting the rest of parameter values as  $s = 15$ ,  $g_0 = 0.3$ ,  $\Gamma^{-1} = 66.66$  and  $\gamma = 3$ , it is possible to match closely the experimental conditions with a SA recovery time of 5 ps, a gain recovery time of 333 ps, a time delay of 15 ns and a filter bandwidth with 400 GHz of FWHM. Moreover, the phase amplitude couplings are set by  $\alpha = 1.5$  and  $\beta = 1$  and the lapsed time by  $\tau = 3000$ .

Under this scheme, when the modulation period parameter is set to a value very close to the repetition frequency of the pulses, the simulations performed reveal the bistability between the states with one and four pulses per round-trip where the pulses

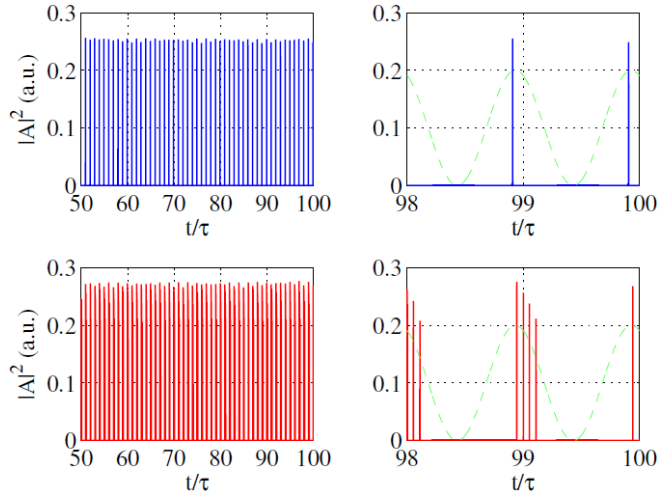


Figure 2.11: Different co-existing time traces of the temporal intensity over several and two round-trips for  $\Delta g = 0.23$  and  $\tau_m = \tau + 0.26$ . The dashed green lines (not to scale) represent the modulation of the gain. ©2015 IEEE.

locate at the region of maximum modulation or, in other words, the region of maximum gain (see Figure 2.11). Furthermore, the inspection of the evolution of the gain for the situations represented in Figure 2.11 enlighten the generation of the pulses. They appear because, during a fraction of the round-trip, the gain surpasses the minimal current required for a single pulse to exist although remaining below the threshold of the system allowing the generation of one or several pulses. This fact, although based in the same principles described in the previous work of Marconi et. al [138], it is explicitly simulated for the case of the modulation of the gain (see Figure 2.12). A close inspection of Figure 2.11 and Figure 2.12 reveals that, for the case of generation of the multi-pulse pattern, the pulses present different heights as they do not generate from the same gain value. This clearly indicates that the pulses are able to interact by means of the gain dynamics.

This interaction is revealing in order to justify the reason why the pulses appear always packed and without the erratic movement observed in cases such as that in Figure 2.3. The reason behind that is the balance between a repulsive interaction between pulses which tend to place themselves in those locations with higher gain [257] and the temporal variation of the gain –down to lower values than the minimal at which independent pulses can exist– which acts as a confining potential and prevent pulses to separate.

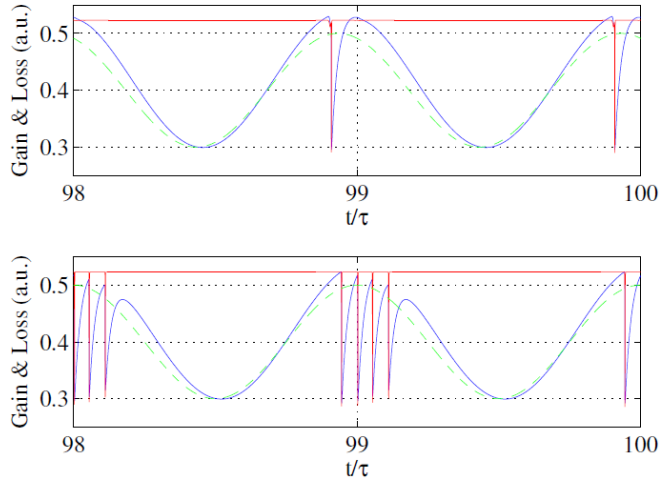


Figure 2.12: Gain and absorption dynamics for the simulations performed over the two co-existing time traces in 2.11. The dashed green lines (not to scale) represent the modulation of the gain. ©2015 IEEE.

In accordance with the experimental observations of Figure 2.9f), the simulation offered by this model also shows a similar multistability stair-like diagram dependent on the modulation of the gain (see Figure 2.13). After a first range around  $\Delta g/g_{th} = 0.2$  where not very clear pulses appear, a jump occurs close to a gain modulation of  $\Delta g/g_{th} = 0.23$  indicating the generation of a first pulse in the cavity. Successive pulses are created by increasing the modulation amplitude. As occurred in Figure 2.9f), by reducing the depth of the modulation of the gain, the simulated curve shows the decrease of the number of pulses present in the round-trip with a high hysteresis.

Finally, as referred in Section 2.3, the modulation period seems to be a very critical parameter for the generation and control of the pulses as detunings of 10 kHz cause the loss of the optical signal. The simulation performed for the sensitivity of the system to the modulation period is in good agreement with the experimental observations as shown in Figure 2.14) where it is shown that there are only independent pulses with non-zero average intensity for a very narrow range of detuning values in good agreement with the experimental results.

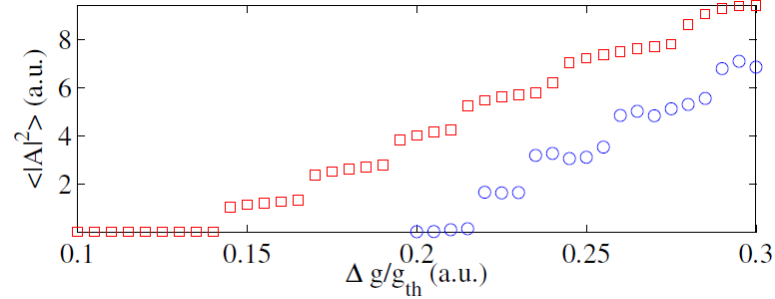


Figure 2.13: Numerical bifurcation diagram for the pulse number as a function of the modulation of the gain. Blue circles (respectively red squares) correspond to an upward (respectively downward) scan of the modulation amplitude. Each jump corresponds to the appearance or disappearance of an additional independent pulse. ©2015 IEEE.

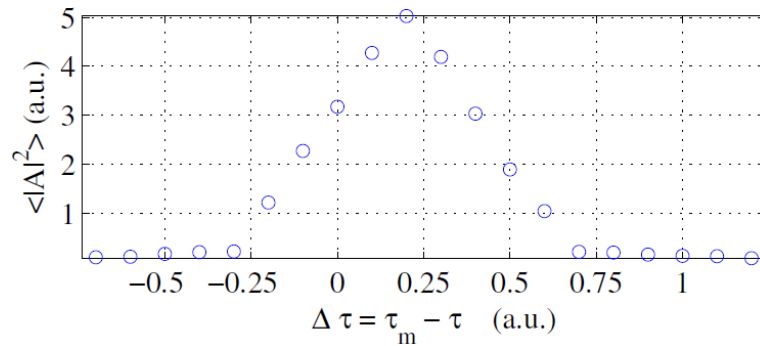


Figure 2.14: Numerical bifurcation diagram for the pulse number as a function of the detuning modulation period as compared to the cavity round-trip. Notice that a maximum number of pulses is obtained for  $\Delta\tau = 0.23$  which corresponds to the effective round-trip in the cavity. ©2015 IEEE.

## **2.5 Conclusions to the Chapter**

In this chapter, it has been presented the scenario over which the generation of trains of pulses is possible using a VCSEL in an external cavity configuration and exploiting methods such as the polarization dynamics and PML. In particular, for an experimental setup based on the PML of a broad area VCSEL emitting at 980 nm and coupled to an RSAM, the experimental observations show strong multistability of the off state and a large variety of pulsating states with different numbers of pulses per round-trip. Based on the experimental observations indicating that the pulses are independent to each other, the hypothesis on the feasibility of the controlled generation of these pulses has been formulated with the purpose that they serve to improve the performance of LiDAR ranging techniques such the RM-CW LiDAR. In order to achieve control over the generation of these pulses, the method proposed consists on the modulation of the bias current of the VCSEL. The experimental results evidence that the control over this parameter offers a satisfactory degree of control on the management of the number and location of the pulses traveling within the cavity, as well as the possibility of generating multi-pulse patterns of these pulses. Besides, the experimental results have been compared with the theoretical simulations derived from a delayed differential equation model which allows the qualitative explanation of the phenomena observed. The generation of the pulses is justified by a temporal surpass of the modulated gain above the value at which a single independent pulse can exist. This modulation of the dynamics forces the pulses to place themselves at the regions of maximal gain and fixes the spacing between pulses. The multistability observed experimentally between different states with different pulse numbers has been theoretically reproduced by a bifurcation diagram with similar performance and the critical value range of the detuning parameter has been confirmed.



## **Chapter 3**

### **Generation of pulses in a SOA-based ring fiber laser**

The current chapter is devoted to the design and experimental study of a SOA-based fibered laser for the generation of optical pulses and it is founded in the adaptation from the propagation of light in air to optical fiber of the experimental setup presented in Chapter 2. The benefits from this conversion will be explicitly justified and the mechanisms inducing pulses such as the use of a saturable absorber as well as the cross-polarization reinjection exposed in the mentioned Chapter 2, will be explored under this fibered scheme.

In each case, slightly modified versions of the same basic setup will be designed and characterized in order to manage and evaluate the impact of the different parameters in the study. The resulting features of each of the two mentioned techniques for the obtaining of pulses will be analyzed and their strength and weakness discussed in separated sections of this chapter. Finally, a proof of principles on the use of the pulses generated by the SOA-based fibered laser proposed will be demonstrated.

#### **3.1 From an air-based VCSEL arrangement to a fiber-based SOA design**

As it has been referred in the previous chapters, the length of the cavity plays a crucial role in the generation of certain pulsating regimes which may serve to reach the ultimate goal of the creation of an arbitrary pulse pattern generation for LiDAR applications. As mentioned, cavity lengths much longer than the gain recovery time of the amplifying medium allows for the appearance of pulsating regimes different from the fundamental state with a single pulse per round-trip, such as the harmonic mode-locking [112] or the coexistence of a multiplicity of states characterized by a different number of pulses per round-trip which are independent to one another. These pulses –also known as Localized Structures (LS)– are characterized by a correlation range much shorter than the size of the system which allows them to place themselves very close to each other. Based on this feature, the capability of LS to form bound states

of pulses and even the feasibility of the control on their independent nucleation or extinction have been experimentally demonstrated [138, 209, 256].

In this sense, the possibility of creating very long optical cavities is interesting in order to increase the number of independent pulsating states as well as to allow the study of new possibilities on the interaction between the pulses. However, the cavity lengths that can be achieved in standard-sized laboratories rooms present intrinsic limitations. Although the optical path in air-based systems can be deflected by optical mirrors to enlarge the cavity length, it would be practically impossible to reach arbitrarily long cavity lengths. Hence, it is at this point where it is possible to benefit from the properties of optical fibers which, in addition of allowing the propagation of light with very low losses, permit the possibility of rolling the fiber up to hundreds of kilometers and overcome the limitations of air-based systems in terms of the cavity lengths achievable in the laboratory.

Furthermore, in accordance with that exposed in Chapter 1, the temporal width of the pulses shares a direct relation with the resolution of LiDAR systems: the shorter, the better [66, 67]. Hence, given the very broad gain spectra shown by semiconductor materials, these devices entail an adequate choice for the generation of ultra-short pulses. Until recently, the most widely used semiconductor devices in fiber optics systems for the generation of pulses consisted on erbium-doped fibers operating at around 1550 nm what constitutes a key emission wavelength in telecommunications attracting much attention for long-span terrestrial and undersea transmission links [258]. In addition, in comparison with fiber systems working at the wavelengths emitted by the VCSELs described in Chapter 2, systems operating at 1550 nm provide a lower attenuation and a higher responsivity (see Figure 3.1). In agreement with this, SOAs emitting at a wavelength of 1550 nm have also recently made a place for themselves in the generation of ultra-short pulses given their potential and inherent advantages such as the simplicity of the electrical pumping or the broadness of the gain.

According to the reasons just exposed, the choice made in this chapter as the gain medium to use for the generation of pulses in a fiber laser has been a SOA (model 1004P from Thorlabs) consisting on a InP/InGaAsP quantum well showing layer structure and a ridge waveguide whose facets are coupled to two pigtailed Polarization Maintaining (PM) fibers –1.5 m length each– with Fiber Connectors exhibiting Angled Physical Contact (FC/APC). The gain of such a SOA, which holds the electronic chip containing quantum well in a butterfly package (see Figure 3.2), is highly dichroic presenting a difference of 21 dB between the Transverse Electric (TE) and Transverse Magnetic (TM) polarizations and displays a nominal emission wavelength centered at 1550 nm, a broad bandwidth of 85 nm, a high saturation output power of 15 dBm and a typical gain of 27 dB for the TE polarization. This package allows for the electrical pumping

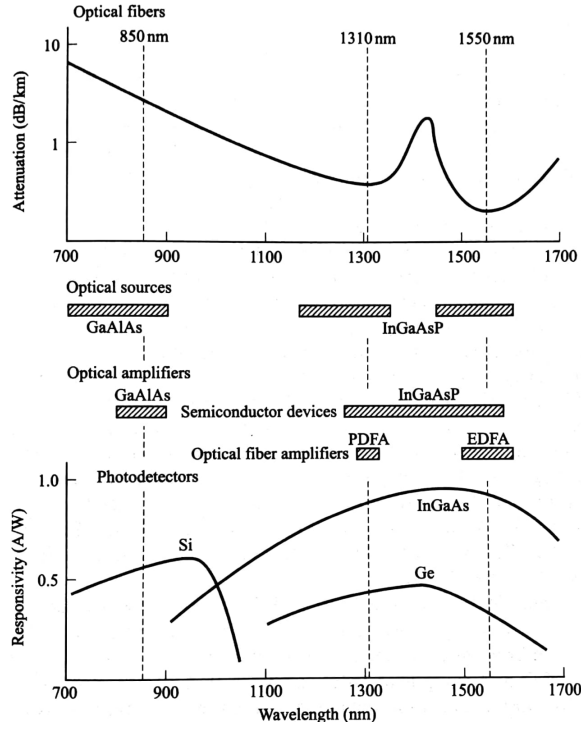


Figure 3.1: Operating range of optical fiber systems and the characteristics of the four key link components (optical fiber, light sources, photodetectors, and optical amplifiers). The dashed vertical lines indicate the centers of the three main operating windows of optical fiber systems [258].

of the gain medium by a Laser Driver (LD) (Thorlabs LDC205) owning an integrated Thermoelectric Cooler (TEC) (Thorlabs TEC2000) and a thermistor for the nominal setting and controlling of the temperature (given that the Joule effect may slightly perturb the selected temperature).

Additionally, for the induction of pulses by passive mode-locking by saturable absorption, a fibered version for the RSAM has been selected. It consists of a chip containing the RSAM (from BATOP GmbH) which is fixed to a 1 m long single-mode non-PM fiber (see Figure 3.3). According to the characteristics offered by the manufacturer, the RSAM chosen here to induce the pulsed emission of the laser shows a nominal resonant wavelength located at 1550 nm, a FWHM of 15 nm and absorption at low intensity of 98% [261]. Furthermore, the fiber ferrule containing the chip is

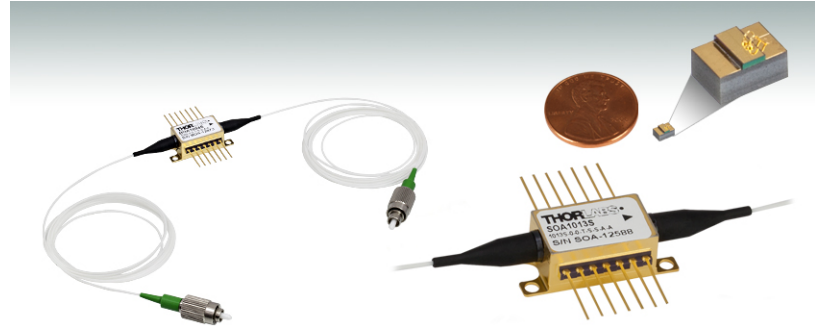


Figure 3.2: Fibered SOA containing an InP/InGaAsP quantum well inside a butterfly case. The output light is coupled to two PM pigtail fibers with FC/APC connectors [259].

connected to a thermal heat sink which is linked to a thermistor for the control of the temperature through a second TEC [255].

Given the difference between the broad span of the gain and the narrow bandwidth of the RSAM, a fibered tunable bandpass optical filter (see Figure 3.4) is also required to allow the selection of a well-defined band of the spectrum of the SOA while blocking unwanted wavelengths. The purpose is to achieve a precise tuning of the resonance wavelength between the SOA and the RSAM which allows for a high enough saturation of the absorber and ensure a good working condition of the system for the mode-locking.

In addition, for the generation of pulses by means of cross-polarization reinjection, polarization controllers operating in optical fibers are needed in order to perform the management of the polarization. Different fiber and air-based polarization controllers are commercially available (see Figure 3.5). A first kind is known as in-line fiber polarization controllers where a single-mode fiber is looped around two or three spools producing a stress-induced birefringence on the fiber when turned (see Figure 3.5a). As a consequence of the change produced in the birefringence of the fiber, the propagation of the light is affected by a delay that, under proper configuration, allows the paddles of the controller to behave as waveplates with retardation given by the equation

$$\phi(waves) = \frac{\pi a N d^2}{\lambda D}, \quad (3.1)$$

where  $\phi(waves)$  is the resultant retardation in terms of wavelength,  $a$  is a constant depending of the material of the fiber (0.133 for silica),  $N$  is the number of loops,



Figure 3.3: Typical arrangements of RSAM devices. On the left, two gold plate copper mounts holding a squared RSAM placed on the center or the edge of the plate. On the right, the RSAM is mounted on the tip of the ferrule a single-mode fiber [260].

$d$  is the fiber cladding diameter,  $\lambda$  is the wavelength and  $D$  is the loop diameter. Depending on the number of loops in the fiber, it is possible to create two or three independent fractional waveplates causing different retardation for the polarization components of the light. The fast axis of the fiber, which is in the plane of the spool, is adjusted with respect to the transmitted polarization vector by manually rotating the paddles what, ideally, makes possible to transform any input polarization state into any desired output polarization [264].

A second kind of device for the polarization control in optical fibers consists of a single-axis fiber bench where the light propagates in the air (see Figure 3.5b). The input fiber is inserted into a fiber port consisting in a fiber connector and a collimator lens that directs the light towards three rotating waveplates (two half-wave plates and a quarter-wave plate) that allow the variation of the polarization state of light at will. Then, light is later collected by a second collimator and coupled into the output fiber through a second fiber port.

These two polarization controllers, as well as the rest of optical fiber components, were tested in order to ensure the best control and performance of the laser. The characterization of all the optical devices shown here is presented in the following sections.

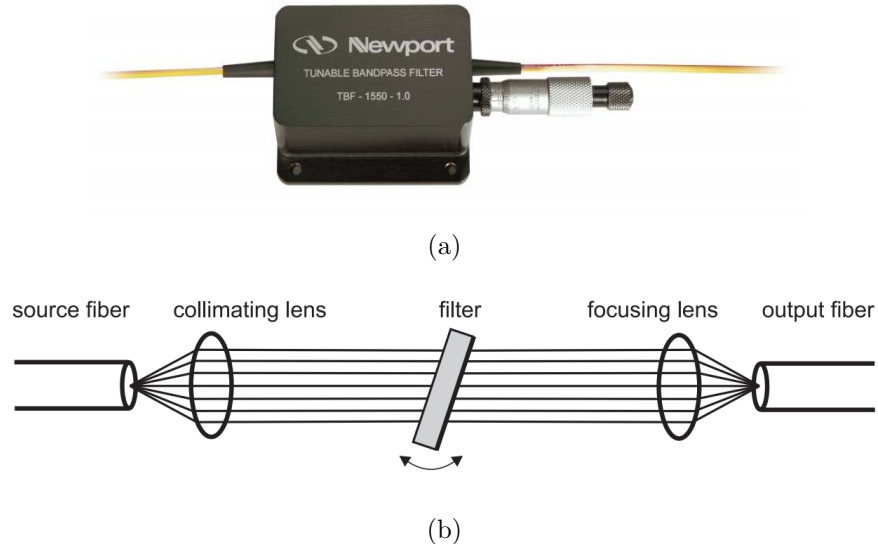


Figure 3.4: Manually tunable bandpass filter. a) typical external aspect of a commercial tunable filter consisting on a case with two coupled fibers and a micrometer for an accurate tuning of the wavelength [262]. b) internally, a thin film coating interference filter blocks the unwanted wavelengths while the micrometer allows the increase of the angle of incidence and the selection of wavelength [263].

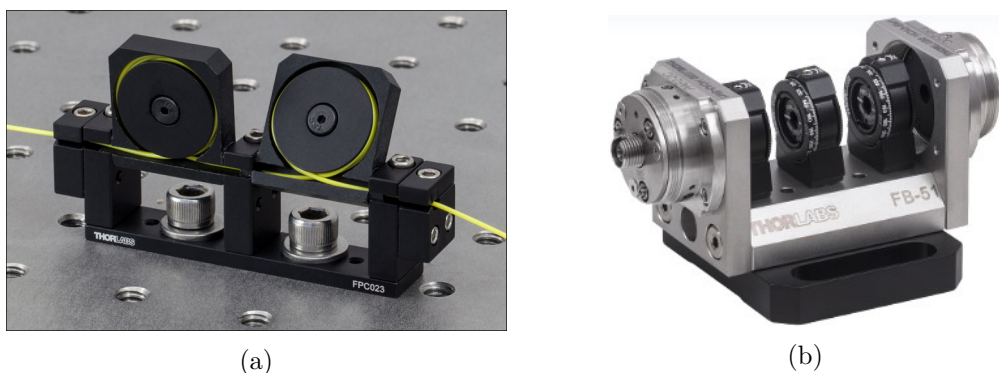


Figure 3.5: Different kind of controllers for the management of the polarization in optical fiber. a) an in-line fibered polarization controller. b) an optical bench for the control of the polarization in air. [264]

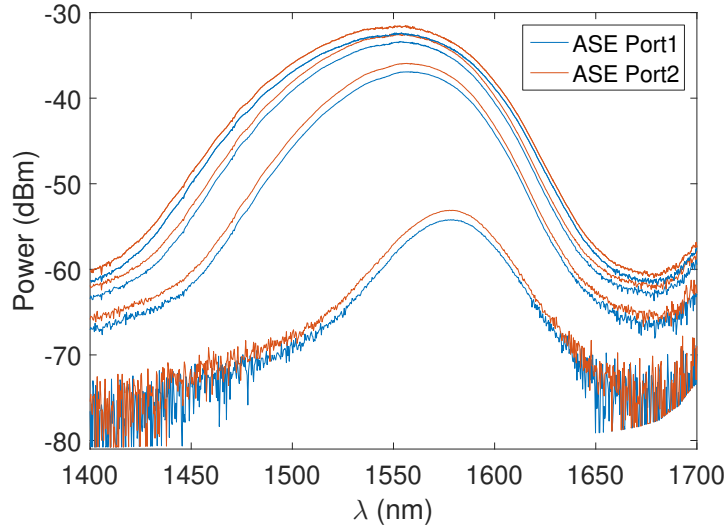


Figure 3.6: ASE corresponding to each of the legs of the SOA. From bottom to top and in blue and red, respectively, the ASE measured for the first and second leg for current values 50 mA, 200 mA, 350 mA, and 500 mA.

## 3.2 Characterization of the optical devices

Prior to the interconnection of all the optical components, each device has been independently characterized in order to assess its correct operation and the existence of possible defects. The first element to be studied has been the SOA given the fundamental role that it plays in the laser. Its characterization has been realized by its direct connection to an Optical Spectrum Analyzer (OSA) to measure its Amplified Spontaneous Emission (ASE) for different values of the control parameters, that is to say, the pumping current and the substrate temperature. Measurements have been performed by varying just one of these two parameters while keeping the other fixed.

As a preliminary test, the outgoing ASE from each of the two connecting ports of the SOA has been measured at a fixed temperature in order to ensure that the optical spectrum is similar in both cases and that the device does not present any damage. The correct operation of the amplifier is shown in Figure 3.6, where the ASE from each leg of the SOA –blue and red traces respectively– at varying current values between 50 mA and 500 mA is represented. As observed, although one of the ports presents a slightly higher gain, both show a regular and similar shape for the ASE curves and the same shifting of the central wavelength when the current is varied.

The shift of the central wavelength does not depend exclusively on the variation of the current but it also does on the changes of the temperature, so the characterization of the performance of the device for these two parameters is required. This has been accomplished by setting the SOA to a constant nominal temperature of 5°C imposed by the TEC while the current is varied from 0 mA up to 250 mA by steps of 25 mA. The same procedure has been repeated also for different temperatures imposed to the SOA ranging from 5°C to 50°C in steps of 5°C. For every operating point given by a pair of values of temperature and current, the data corresponding to the central wavelength and FWHM of the gain curve has been registered.

As a result, this set of measurements allows for the representation of 2D-maps describing the behavior of the device and which are shown in Figure 3.7. The map represented in Figure 3.7a allows visualizing the evolution of the gain curve and central wavelength of the SOA. The color bar indicates the values of the central wavelength between a minimum of 1540 nm (in blue) and a maximum of 1600 nm (in red) while the black contour lines indicate different constant wavelength values. Hence, the information contained in the figure permits the setting of the operation point of the SOA for a given pair of temperature and current values. For example, in order to achieve a central wavelength close to 1550 nm, the temperature and current values should be set at any of the pair of values defining the contour line corresponding to the mentioned wavelength (for instance, a current of 400 mA and a temperature of 15°C). The FWHM of the SOA has also been measured according to the same procedure described above and a similar map showing, in this case, the variations of the FWHM with respect to the current and temperature, is depicted in Figure 3.7b. In this case, the color bar stands for the values of the FWHM between the minimum in blue (50 nm) and the maximum in red (110 nm) and the contour lines indicate constant values of the FWHM. It is observed, in general, that the FWHM broadens for increasing temperatures and currents. However, an unexpected and sudden broadening takes place for low currents at temperatures around 45°C which is attributed to the overheating of the device.

The next device to be characterized is the RSAM. While the SOA presents an emitting spectrum, the corresponding spectrum of the RSAM is absorptive. Hence, it is required to send some emission into it in order to observe the amount of losses introduced by the device. In this case, this is achieved by connecting the SOA and the RSAM by using a three-port single-mode optical circulator (Newport) operating at 1550 nm and working under the scheme 1 → 2 → 3. The ASE of the SOA is sent from port 1 to port 2 where the RSAM is connected. After reflection on the RSAM, light is sent back to the port 2 and transmitted towards port 3. Hence, the light coming out from this port 3 consists in the ASE of the SOA plus the absorption produced by the

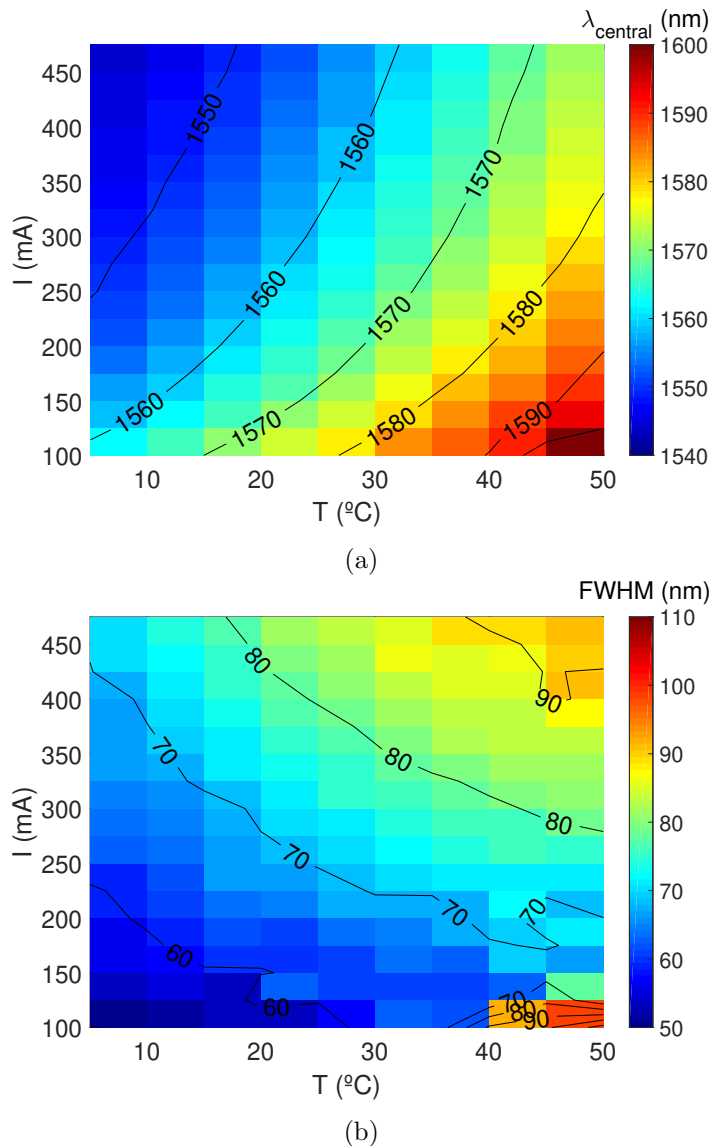


Figure 3.7: 2D-maps for the characterization of the SOA. a) variation of the central wavelength of the gain curve of the SOA with respect to the current and temperature. The color bar stands for the wavelength value. b) variation of the FWHM of the gain curve of the SOA with respect to the current and temperature. The color bar stands for the FWHM value.

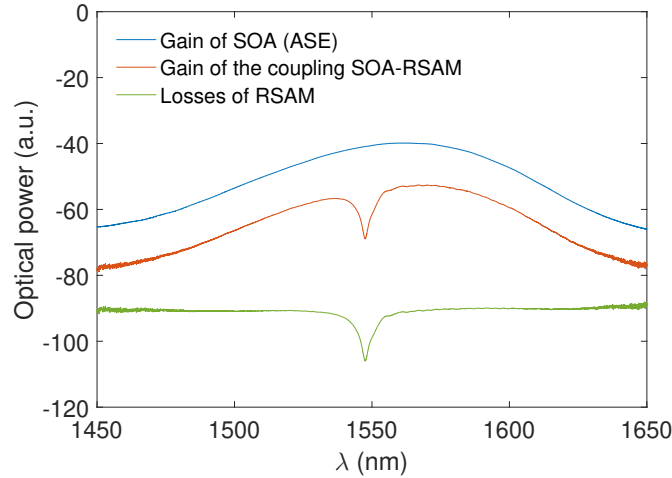


Figure 3.8: Optical spectra corresponding to the SOA and RSAM in different configurations. In blue, the ASE corresponding to the solitary SOA. In red, total optical spectrum when the SOA and the RSAM are coupled. In green, the losses introduced exclusively by the RSAM obtained from the subtraction of the blue and red curves.

RSAM. This total spectrum, which corresponds to the convolution product of each of the respective emitting and absorptive spectra, is sent to the OSA where the losses effects introduced by the RSAM evidence as a deep valley in the ASE of the SOA. Figure 3.8 shows this situation when the temperature of both the SOA and the RSAM is kept at 5°C and the pumping current of the SOA is set to  $I = 100$  mA. The green line in Figure 3.8 corresponds to the losses caused by the solitary RSAM and it has been calculated by subtracting the ASE of the SOA to the total spectrum (blue and red lines respectively in Figure 3.8) and allows for the characterization of the RSAM at different temperatures.

According to this, the behavior of the RSAM at different stabilized temperatures has been assessed at a constant input from the SOA –set at 100 mA and 5°C– leading to an emission around 1560 nm and an input power into the RSAM of 5.6 pW. A redshift of the resonance in the total spectrum of approximately 1.5 nm has been observed while increasing the temperature from 20°C to 40°C as Figure 3.9 illustrates. Temperatures out of the previous range have also been explored from 5°C up to 90°C however, while the shifting of the peak of absorption of the RSAM follows a linear relation, the depth of the peak does not vary in such a linear dependency (see Figure 3.10) but follows the

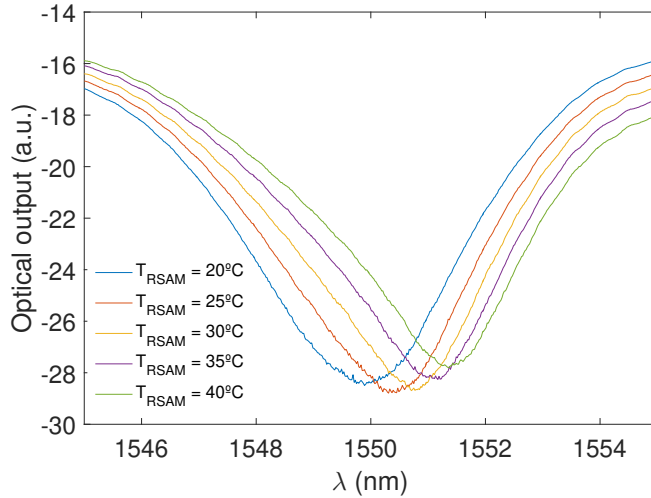


Figure 3.9: Detail of the displacement of the resonance wavelength of the RSAM for different temperatures at fixed current and temperature values of the SOA.

corresponding changes of the unsaturated reflectivity of the RSAM with respect to the variation of the wavelength offered by the manufacturer [261] except for temperatures beyond 60°C due to the overheating of the device.

In order to prevent the damage of the RSAM, the two extremal temperatures of 5°C and 90°C will not be chosen to stabilize the temperature of the device. From the two remaining set of points in Figure 3.10, those between 20°C and 40°C –corresponding to the same values of temperatures of Figure 3.9 –present a higher absorption than those between 60°C and 80°C. Accordingly, the working temperature of the RSAM will be set in the proximity of the room temperature given the better absorption of the device and the selection of softer temperatures that avoid the condensation and deposition of water causing harms in the RSAM.

As mentioned in Section 3.1, other devices as a filter or polarization controllers are required for the generation of pulses and need to be characterized. Provided that different setups for the exploration pulsating regimes have been built –depending on whether the generation of pulses is produced by mode-locking through the RSAM or by cross-polarization reinjection–, different filters and polarization controllers are also used in order to fulfill the conditions of the experiments. Hence, in the belief that the description and of each of these devices will become much clearer in the context of each setup, they will be characterized in the following sections.

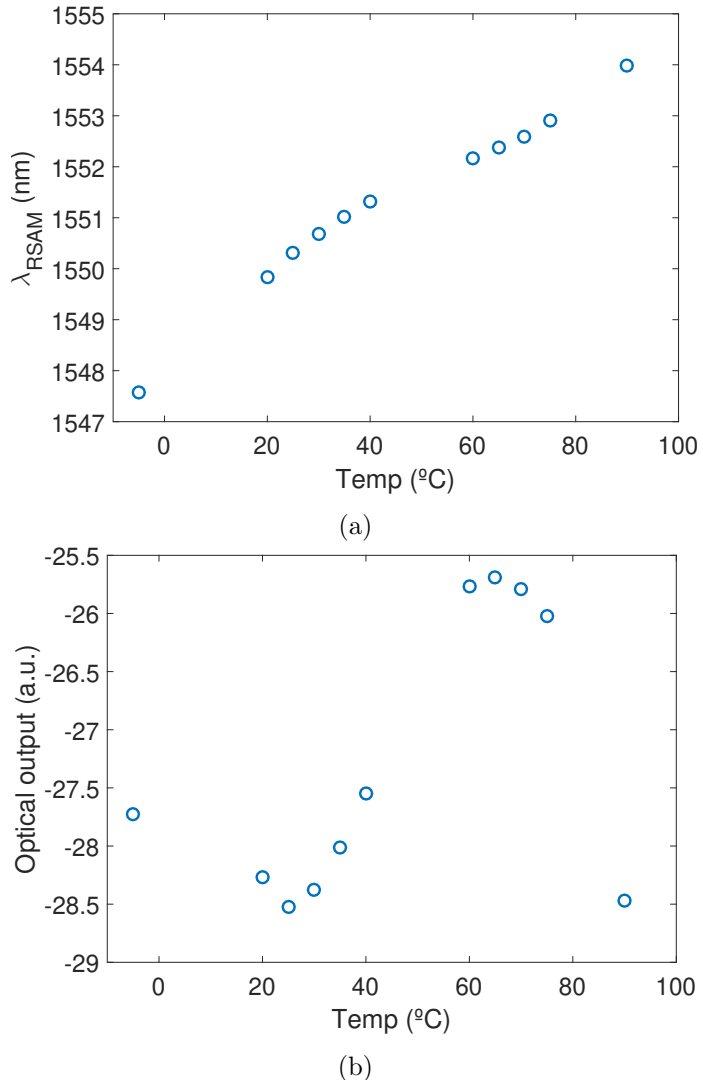


Figure 3.10: Characterization of the absorption of the RSAM when its temperature is varied for constant current and temperature values of the SOA which emits at 1560 nm and sends an input power of 5.6  $\mu\text{W}$  into the RSAM. The variation of the temperature implies in a) a linear growth on the wavelength of resonance of the RSAM while in b) the depth of the peak of absorption follows the curve of unsaturated reflectivity offered by the manufacturer in the datasheet of the device [261].

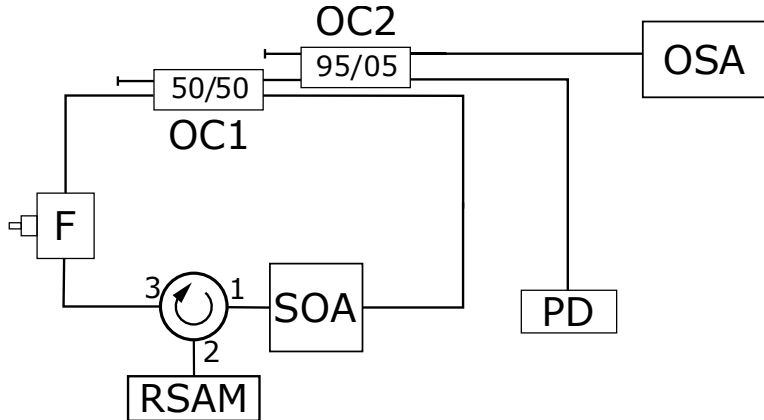


Figure 3.11: All fibered experimental setup for a laser in a unidirectional ring cavity configuration for the generation of pulses by passive mode-locking induced by saturable absorption. OSA: optical spectrum analyzer, PD: photodetector, OC: optical coupler, F: band-pass filter.

### 3.3 Generation of pulses by a SOA-based fiber laser with a saturable absorber

The approach adopted to build in fiber the analogous setup to that described in Chapter 1 is shown in Figure 3.11. While previously for the VCSEL the setup consisted in a Fabry-Pérot cavity, here, the setup consists on the SOA and the RSAM characterized in the precedent section which has been coupled by means of an optical circulator operating under the  $1 \rightarrow 2 \rightarrow 3$  scheme. A filter is also present in the cavity with the purpose described in Section 3.1 of selecting a narrow section of the net gain curve. The interconnection of all the fibered devices conforms a unidirectional ring cavity with an approximate length of 10 meters.

The filter is a 0.8 nm narrow band-pass filter (model TBF-1550-1.0-FCAPC from Newport) showing a tunable center wavelength operating nominally between 1535 and 1565 nm. It is coupled to two non PM single-mode fibers and counts with a micrometer offering a resolution of 0.05 nm. Different locations of the filter within the setup have been explored although the optimal location found in terms of the dynamical response of the system corresponds to that in which the filter is placed after the RSAM, hence, avoiding losses and maximizing the power on the RSAM.

This filter has been tested and characterized to achieve the high-precision tuning of the wavelength. The characterization has been accomplished by coupling only the

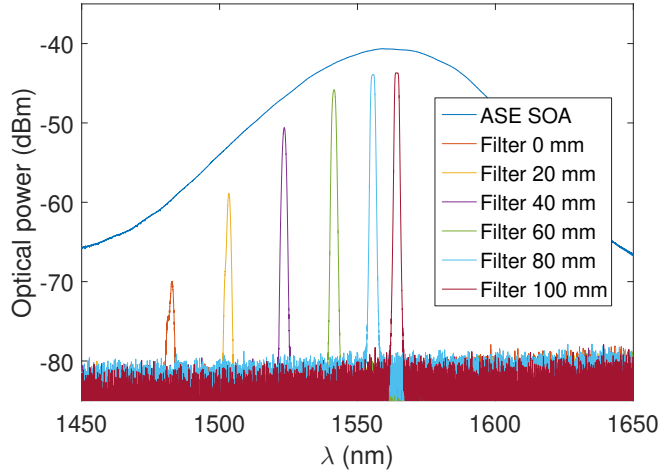


Figure 3.12: Charaterization of the optical fibered filter. The presence of the filter reduces the width of the ASE of the SOA to a small peak with a FWHM of 0.8 nm. The central wavelength of the filter can be set to different positions by varying the micrometer.

SOA and the filter and monitoring the output in the OSA. First, the SOA parameters have been set to a temperature of 5°C and a current of 100 mA and the output trace of the ASE has been acquired as a reference. Next, the filter has been connected to the SOA and its filtering effects have been explored by varying the micrometer from 0.5 mm up to 11 mm in steps of 0.5 mm. The performance of the filter allows to walk through the ASE curve as shown in Figure 3.12, where only micrometers steps of 1.5 mm have been represented for the sake of clarity. It is noticed that the lower range of wavelengths covered by the filter extends beyond the nominal 1535 nm provided by the manufacturer although showing some distortion evidenced as a small lobe on the left side of the monitored signal. On the other hand, the nominal value of 1565 nm really constitutes the upper limit of the filter as the displacement of the operating wavelength is reversed when the micrometer is set beyond 100 mm (not shown in Figure 3.12 for clarity).

Once that all the elements in the setup have been individually characterized, they are interconnected according to the unidirectional ring cavity configuration shown in Figure 3.11 and the exploration of the dynamical behavior of the laser is initiated. In this setup, the light leaves the cavity by means of a 50%-50% fiber coupler and is sent to a second 95%-05% coupler which splits the outgoing signal, directing the 95%

towards a photodetector for the inspection the temporal trace and the remaining 5% to the OSA for monitoring the optical spectrum of the lasing signal.

The temperatures of the SOA and the RSAM have to be chosen to match closely the 1550 nm according to the previous characterization of the gain peak of the SOA and the resonance of the RSAM. However, due to the big losses that occur at 1550 nm caused by the RSAM, the filter is not tuned to be exactly coincident with this resonance in order to prevent that the RSAM may not be saturated enough at that point to produce the pulses. Instead, the filter will be tuned to operate on the range of wavelengths defined by the valley produced by the losses of the RSAM like that shown in the red curve of Figure 3.8. The variable parameter chosen to explore the dynamics of the laser is the current of the SOA while the position of the filter and the temperature of the devices remain fixed.

Initially, the dynamics is explored at temperature values of 0°C for the SOA and 20°C for the RSAM in order to ensure that the operating wavelength of the system remains around 1550 nm when varying the current of the SOA. Under these conditions, the threshold of the laser appears at approximately 81 mA and a clear pulsed dynamics manifests when raising the current between 100 mA and 391 mA with an intracavity optical power in the order of the milliwatt (as a reference, 2 mW were reached at  $I = 260$  mA). However, the output trace obtained does not remain temporally stable and a multiplicity of changing pulsing states are observed for the same temperature and current parameters values, that is,  $T_{SOA} = 10^\circ\text{C}$ ,  $I_{SOA} = 325$  mA and  $T_{RSAM} = 20^\circ\text{C}$  (see Figure 3.13).

In all cases, a common repetition time of approximately 53.5 ns is observed in each trace indicating a cavity length close to 10.71 meters according to the simple relation between space and time given by  $L = c\tau/n$  where  $L$  is the cavity length,  $c$  is the speed of light in vacuum,  $\tau$  is the round-trip time in the cavity and  $n$  is the refractive index of the fiber (approximately 1.5 for silica fiber). This estimation for the length of the cavity is in very good agreement with the rough measurement of 10 meters previously mentioned at the beginning of this section.

However, different coexisting traces are observed showing a different number of pulses per round-trip, different amplitudes and even different sign for the amplitude of the pulses being either positive (bright pulses) or negative (dark pulses). Temperatures values for the SOA of 15°C and -10°C have also been explored although the same unstable dynamical behavior is observed. However, for higher temperatures the system shows a higher threshold and a shorter range of currents leading to pulsing dynamics while for lower temperatures the threshold is reduced and the dynamics is present even when the current reaches the upper limit of the laser driver.

The origins of such instabilities have been explored and, provided that the mechani-

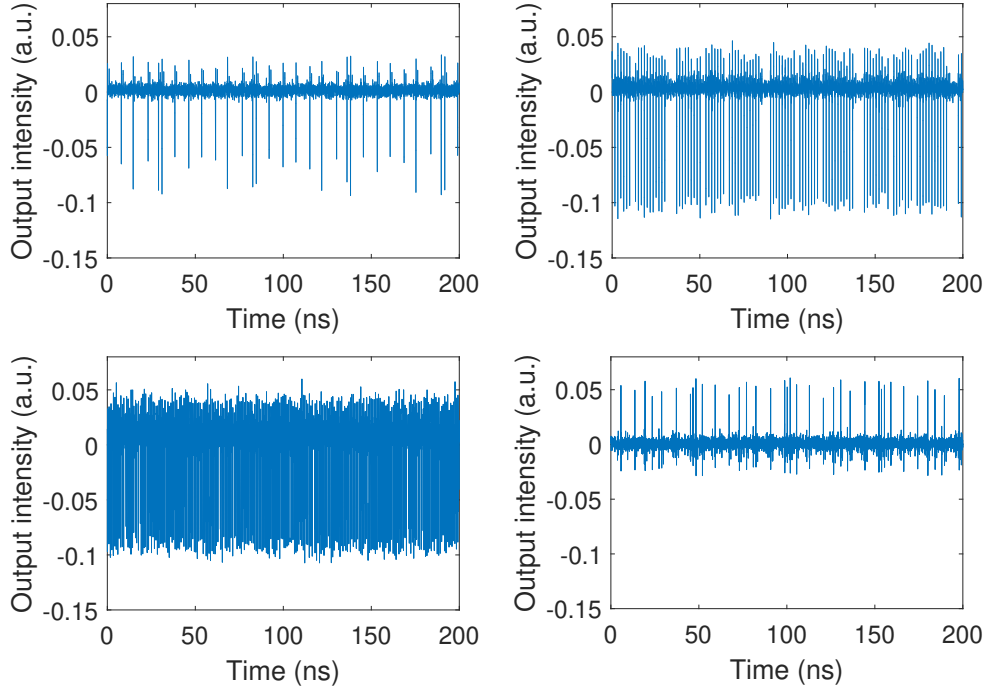


Figure 3.13: Emission of brief and different coexisting pulsed states produced by the fibered SOA-RSAM ring cavity for the same set of parameters values ( $T_{SOA} = 10^\circ\text{C}$ ,  $I_{SOA} = 325 \text{ mA}$  and  $T_{RSAM} = 20^\circ\text{C}$ ). An underlying repetition rate of 53.5 ns corresponding to the cavity length is observed.

cal and thermal fluctuations were already considered and minimized during the design of the setup, the efforts are now directed towards controlling the degree of freedom of the polarization in the system because, as mentioned in Chapter 2, the nonlinear polarization rotation along the fibered cavity is also able to generate pulses [148]. Thus, similar setup configurations to that presented in this section but incorporating the control of the polarization have been investigated for such a purpose.

### 3.4 Generation of pulses by a SOA-based fiber laser under cross-polarization reinjection

As mentioned before, the specifications of the SOA used here for the generation of pulses establish its high dichroism. This has been experimentally checked by using a

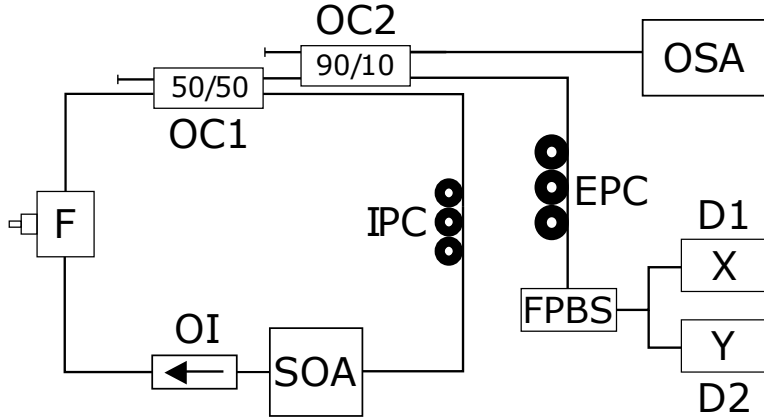


Figure 3.14: Setup for the generation of pulses by crossed reinjection polarization. It presents the same optical devices described in this chapter but getting rid of the RSAM and incorporating in-line fibered polarization controllers to reinject and detect specific polarization states of the light. IPC: intracavity polarization controller, EPC: external polarization controller, FPBS: fibered polarizing beam splitter, OI: optical isolator, OSA: optical spectrum analyzer, OC: optical coupler, D: photodetector, F: band-pass filter.

PM Fibered Polarizing Beam Splitter (FPBS) (model PBC1550PM-APC from Thorlabs). The FPBS receives the signal containing the two corresponding orthogonal polarizations, TE and TM, aligned respectively with the fast and slow axis of the input fiber and splits this signal by means of a calcite prism into two output fibers transmitting each one of the TE and TM polarization components but aligned in both cases with the slow axis of each output fiber. This FPBS has been connected only to the SOA in open cavity configuration and it has demonstrated to provide a substantially higher gain along the axis aligned with the TE polarization –called from now on *x*-polarization– than that aligned with the TM polarization –called from now on *y*-polarization.

In order to explore the effects of reinjecting different polarizations into the SOA to generate pulses, the setup described in Figure 3.11 has been modified as follows. The configuration of the fibered setup still consists in a unidirectional fiber ring but the RSAM has been replaced by an in-line Intracavity Polarization Controller (IPC), as shown in Figure 3.14, in order to select a specific polarization state of the light to be reinjected in the SOA. As described in Section 3.1, this polarization controller consists of three paddles which may be turned in a range of approximately 270° holding the

fiber looped inside. The stress produced in the fiber induces a birefringence which leads to a specific retardation to the signal. By setting the appropriate arrangements of loops in the paddles, they show a behavior which is very close to that of a half-wave or a quarter-wave plate that allows setting a specific polarization for the signal at the output of the controller for an arbitrary input polarization. For the case treated here, the fiber used to create the loops in the polarization controller is the own output leg of the 50%-50% coupler. This fact, together with the removal of the RSAM and the replacement of the fibered circulator by a non-pig-tailed optical isolator, has reduced the cavity length –with respect to the previous configuration with the SOA and the RSAM– to approximately 7 meters.

Hence, while the 50% of the light is reinjected into the SOA, the other 50% is sent to the detection branch through a second coupler of coupling ratio 90%-10%. The 10% is collected by the OSA for the inspection of the optical spectra and the 90% is sent to an External Polarization Controller (EPC) connected to a FPBS that splits the input signal in the two orthogonal polarizations. These polarizations are sent to two 12 GHz photodetectors (Newfocus model 1544B) –D1 for the  $x$ -polarization and D2 for the  $y$ -polarization– connected to a 12 GHz oscilloscope with a sampling rate of 40 GSa/s (Agilent Infiniium DSO81204A) for monitoring the temporal trace.

The preliminary characterization of the performance of the IPC needs to be accomplished in an open cavity in order to monitor the polarization of the output signal to be reinjected into the SOA. Hence, the ring cavity is opened at the point of connection between pigtail fiber of the SOA and the IPC. This unused port of the SOA remains unconnected while the other remains attached to the optical isolator, the bandpass filter, the 50%-50% coupler, the IPC and also the FPBS has been connected to this whole opened branch to properly monitor the variations on the  $x$  and  $y$ -polarizations. In order to visualize the signal levels for the whole range of currents reached by the SOA, a triangular modulation has been imposed to the DC current of the optical source according to the equation

$$I_{LD} = I_{LD_{SET}} + I_{MAX} \frac{U_{MOD}}{V}, \quad (3.2)$$

where  $I_{LD}$  is the time-dependent injection current,  $I_{LD_{SET}}$  is the DC component of the current,  $I_{MAX}$  is the maximum value of the power supply,  $U_{MOD}$  is the voltage of the modulation signal and  $V$  is the maximum allowed input voltage (20 V for the source used here). In order to cover the whole range of current values available from the source, it is set a DC current of  $I_{LD_{SET}} = 245$  mA which is modulated by a symmetrical ramp function with a DC level of 0 V, an amplitude of 10 V<sub>pp</sub> and a low frequency of

100 Hz from the external function generator.

Under these conditions and with the optical fiber properly looped into the spools according to the previous Equation 3.1, the three paddles present in the controller are configured to behave as two quarter-wave plates –external paddles– and a half-wave plate –central paddle–. Thus, the control of the output polarization from the IPC to be reinjected in the SOA can be managed as shown in Figure 3.15. For an unknown input polarization in the IPC, it can be empirically found a certain combinations of angles for the three paddles (let us call it *reference setting*) converting that unknown input polarization into a linear polarization state aligned with the slow axis of the output fiber of the FPBS and also with the main output polarization of the solitary SOA (*x*-polarization). Figure 3.15a shows how the *x*-polarization of ASE from the SOA follows the periodic ramp imposed by the modulation and is maximized when setting the paddles to the mentioned *reference setting*. The small red signal corresponds to the residual gain produced by the SOA in the *y*-polarization.

Under these conditions, if the half-wave plate of the controller is turned by 22.5° from the *reference setting*, the phase difference induced between both polarization components of the signal causes the state of polarization of the light to progressively change from the previous linear state to elliptical and finally to a circular state of polarization. In this case, both the *x* and *y*-polarization reach the same amplitude level as observed in Figure 3.15b.

If the half-wave plate is now further turned beyond 22.5° up to 45° from the *reference setting*, the circular polarization state is gradually transformed into a linear *y*-polarization which, in other words, can be seen as a rotation of 90° of the linear *x*-polarization. Indeed, this is what is shown in Figure 3.15c where, in contrast with what is observed in Figure 3.15a, only the *y*-polarization is present and maximized.

Obviously, the previous behavior can also be reproduced by varying not the half-wave plate but the output quarter-wave plate (the third paddle of the controller in the sense of propagation of the light). Hence, the situation observed in Figure 3.15b have been obtained by rotating the quarter-wave plate by 45° from the *reference setting*. As expected, completing the turn of this paddle up to 90° allows recovering the situation of Figure 3.15a. This procedure can be accomplished in the same way for the EPC although in this case, as the EPC is external to the ring cavity, the setting can be performed even when the system is lasing.

Although the management of the polarization for the cases just exposed is satisfactory in general terms, it is important to remark the existence of some inherent drawbacks present when performing the control of the polarization with in-line fibered polarization controllers. The first point to consider is that the input polarization in the controllers is always unknown due to all the bends and stress induced in the fibers

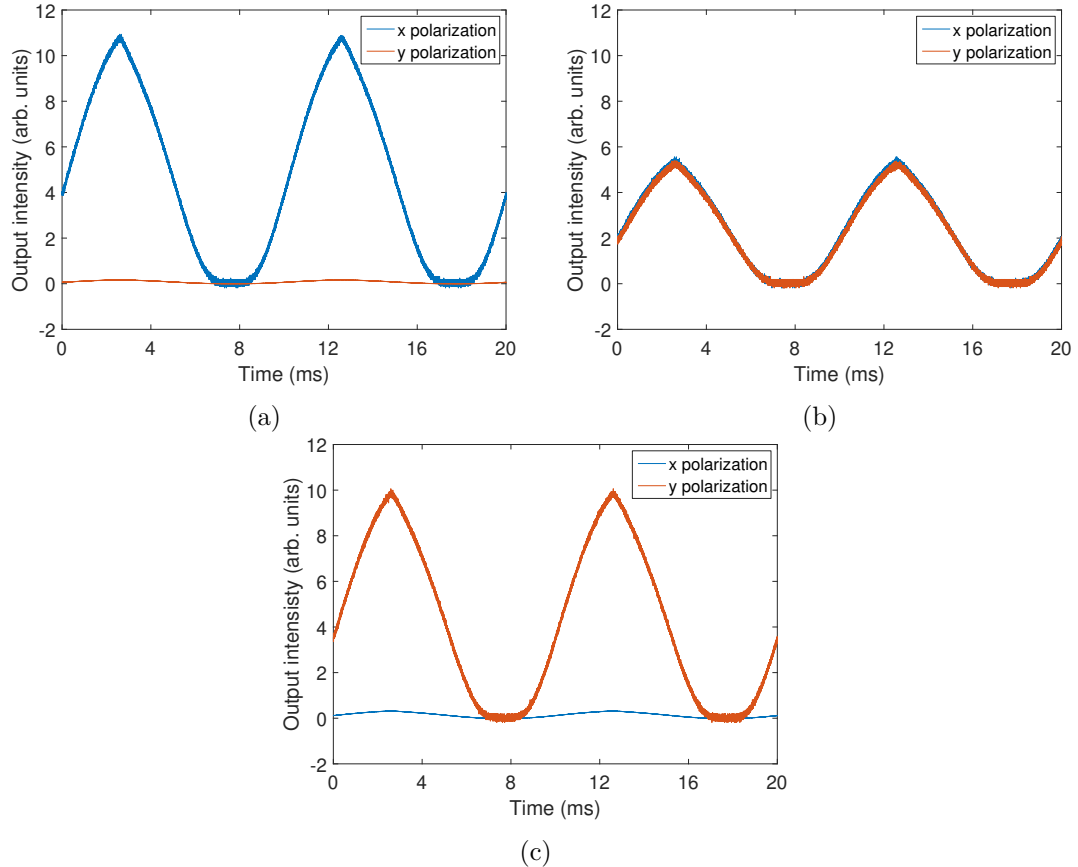


Figure 3.15: Management of the polarization performed by the IPC to the signal sent by the SOA when the DC current is modulated by a triangular signal. a) an empirical combination of angles for the three paddles (respectively  $\lambda/4$ ,  $\lambda/2$  and  $\lambda/4$  wave plates) allows to maximize the signal sent along the  $x$  axis of a FPBS (the small signal along the  $y$  axis corresponds to the residual emission of the SOA in this polarization). b) when the third plate in the sense of propagation of the light ( $\lambda/4$ ) is turned by  $22.5^\circ$  on the basis of the paddles configuration in a), the linear polarization state propagating along the  $x$  axis transforms into circular polarization and both components reach the same amplitude. c) if the plate  $\lambda/2$  is turned by  $45^\circ$  on the basis of the paddles configuration in a), the linear polarization state propagating along the  $x$  axis is turned into the  $y$  axis.

along the optical path. This translates in the unawareness on the angle required for the paddles to achieve a reference polarization state and ensure a good operation of the device and a correct control of the polarization. This aspect, summed to the fact that the birefringence of the fiber is highly sensitive to changes in the room temperature, not only makes very difficult to establish a fixed polarization state of reference with the paddles of the controller but also obliges to permanent readjustments during the experiment. Furthermore, as indicated by the manufacturer, the retardation achieved by looping the fiber in the spools is close to –but not exactly– a half or a quarter-wave plate provided that the numbers of loops cannot be fractional and must be a whole number. This fact together with the lack of a protractor for determining precisely the angle tilted by the paddles leads to the introduction of an uncertainty of few degrees in the exact determination of the angle tilted and reduces considerably the repeatability of the device. As a consequence, the in-line polarization controllers are not deterministic and allow only to have a crude estimation of the polarization state that is reinjected into the SOA. All these aspects force the method to be empirical and iterative until the required behavior is obtained. However, although it may take some time to achieve a good configuration of the plates for the generation of pulses, once that a pulsing state is reached, it remains temporally stable for hours in contrast with what observed in the setup containing the RSAM of Figure 3.11. The stability provided by these train of pulses facilitates their use for LiDAR measurements as it will be shown later in Section 3.5 of this chapter.

For the control on the variation of the polarization effects on both the IPC and the EPC when the cavity is closed, the mentioned uncontrolled evolution of the polarization along the system due to random bends in the fiber is minimized by rolling the fiber in fiber holders which are screwed to the optical table and, therefore, limiting the freedom of movement of the fiber pigtail that is no longer able to bend or twist. Furthermore, for the case of the EPC, it is assumed that the length of the legs of the 90%-10% fiber coupler is not long enough to produce a big variation of the polarization. For the sake of simplicity, the IPC and EPC are set to produce an output  $x$ -polarization from each of them so this is the polarization state to be reinjected in the SOA and detected in D1. As explained above, under this situation, by rotating 45% the half-wave plate of the IPC, the output polarization of the IPC is turned into  $y$ -polarization, reinjected into the SOA and detected by D2.

The confirmation of the correct configuration of the IPC and EPC paddles is assessed by the inspection of the LI curves of the system obtained by the same modulation of the DC current previously described in Equation 3.4 with a frequency from the external function generator set in this case to 10 MHz. The effects of such a modulation of the SOA current are observed on the oscilloscope allowing for the representation of different

LI curves of the laser which depend on the different polarization states reinjected into the SOA. Such a method serves to assess the correctness of the previous configuration of the paddles for the simplest cases of reinjection: the reinjection of the linear  $x$ -polarization into the same linear  $x$ -polarization of the SOA –without any variation or rotation of the polarization– or the reinjection of the  $x$ -polarization into the  $y$ -polarization– by orthogonally rotating the polarization of the SOA. According to this, it is possible to inspect the threshold of the laser for each case of reinjection to obtain fundamental information about the dynamical performance of the laser as shown in Figure 3.16. The blue and orange lines –respectively rise and fall of the current of the SOA–correspond to the detection of the  $x$ -polarization while the detection of the  $y$ -polarization is represented by the purple and green lines –respectively rise and fall of the current of the SOA. It is observed that, if the same output polarization is sent back to the SOA (reinjection  $x$  into  $x$ ) the lasing is favored and the threshold of the laser is minimized. On the contrary, if polarization is turned by  $90^\circ$  (reinjection  $x$  into  $y$ ) the lasing is hindered and the threshold is maximized. No signal is ever measured in the LI curves for the  $y$ -polarization as the EPC is configured to set the light in the  $x$ -polarization. As expected for the IPC, when the paddles are configured for  $x$  into  $x$  reinjection the threshold reaches a minimum value of approximately 125 mA. If the polarization is turned for  $x$  into  $y$  reinjection, the threshold clearly increases up to approximately 325 mA and the lasing is one order of magnitude weaker.

However, as observed, there is no dynamics detected for any of these two concrete situations of reinjection in the previous Figure 3.16. Although this seems logical for  $x$  into  $x$  reinjection, it results unexpected for the case of  $x$  into  $y$  reinjection provided that the competition between polarizations should induce the generation of pulses as discussed in Chapter 2. Nevertheless, this may be caused by the poor amplification offered by the SOA in the  $y$ -polarization. Hence, the next step forward consists on exploring the cross gain reinjection of  $x$  into  $y$  not in a linear polarization state but slightly increasing its ellipticity to allow a small portion of the light to be amplified in the  $x$ -polarization. This slight increase of the ellipticity can be easily accomplished by tilting the half-wave plate by a small angle with respect to the state of linear  $y$ -polarization. At this point, one of the main drawbacks of the use of fibered polarization controllers clearly emerges. The lack of protractors in these devices (see Figure 3.15) makes highly imprecise tilting the paddles at any specific angle, being practically impossible to achieve the repeatability required to systematically study the effects of the polarization in the dynamics of the laser. Nevertheless, in order to overcome this inconvenient and improve the control of the polarization, homemade protractors were designed and assembled together with the polarization controllers to provide an estimation of the angles formed by the paddles with respect to the vertical line

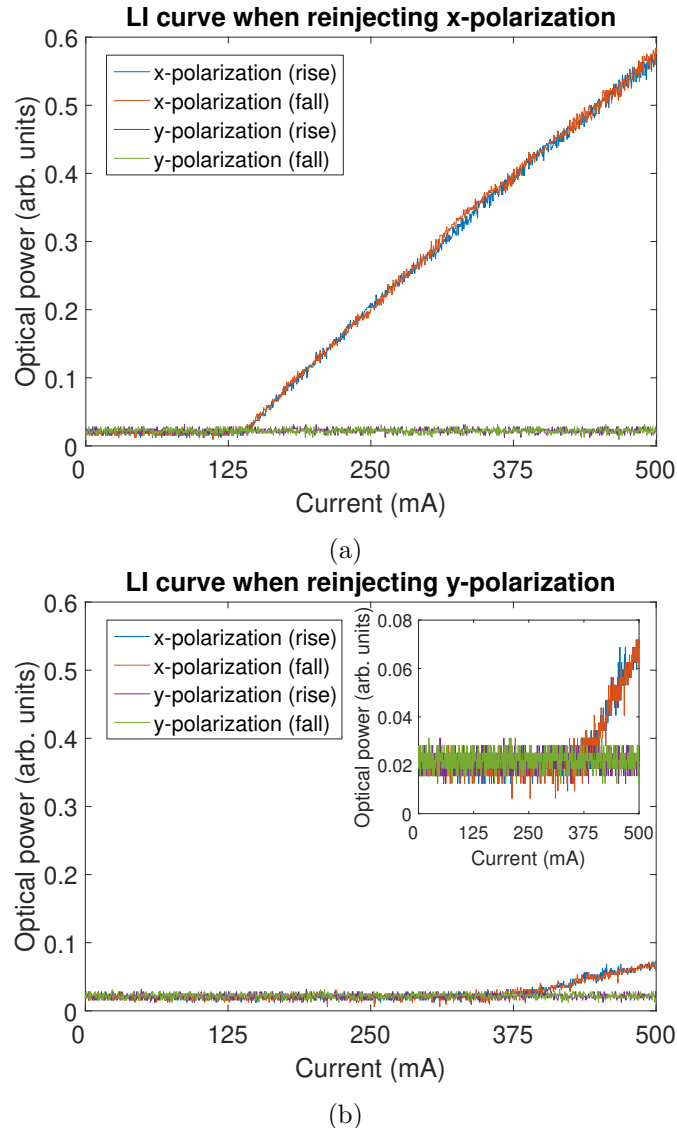


Figure 3.16: LI curves corresponding to different cases of reinjection of light in the SOA. a) the light reinjected corresponds to the  $x$ -polarization (that of higher ASE in the SOA). The threshold is minimized down to 125 mA. b) the light reinjected corresponds to the  $y$ -polarization (that of lower ASE in the SOA). The threshold is maximized up to 375 mA.

represented by  $0^\circ$ . Even when the paddles are not perfect half and quarter-wave plates, this quantification of the tilted angles is useful and allows for a better understanding and control on the polarization state of the reinjected light.

According to this, the reinjections of the  $x$  into  $y$ -polarization are performed increasing the ellipticity of the light by setting the half-wave plate of the controller in a range of angles between  $3^\circ$  and  $11^\circ$  in which the dynamics is clearly revealed in the system. For the case of  $11^\circ$ , the dynamics emerges in the setup as evidenced in the LI curve shown in Figure 3.17, where the blue and orange curves represent respectively the rise and fall of the LI curve for the  $x$ -polarization and the purple and green curves are the rise and fall of the LI curve for the  $y$ -polarization. As observed, the rise and fall overlap for each polarization with exception of the region around 325 mA for the  $x$ -polarization in which the rising curve is narrower and shows a step indicating a change of regime in the temporal trace. Surprisingly, while a threshold near 325 mA would be expected given that the reinjection signal consists on a slightly perturbed state of the  $y$ -polarization, the system starts to lase at a threshold value which is close to the 125 mA corresponding to the reinjection on the  $x$ -polarization (as it was shown in Figure 3.16). This may be explained due to the 21 dB gain difference between the TE and TM polarization components in the SOA mentioned in Section 3.2. That fact causes that even the small amount of light entering through the  $x$ -polarization is strongly amplified and makes the system to lase preferentially on this polarization. On the other hand, although the  $y$ -polarization is weakly amplified, it is still able to interact with the  $x$ -polarization in the way described in Chapter 2 to generate the emission of pulses experimentally observed described next. The traces detected by D1 (blue) and D2 (red) for different current values of the LI curve of Figure 3.17 are shown in Figure 3.18, where two round-trips of pulses are represented on each of the figures. Obviously, below threshold at 100 mA, only noise is detected but as the current is increased above threshold up to 130 mA the system begins to lase and pulses start to emerge although without a well defined structure for the train of pulses (see Figure 3.18a). Once the current reaches a value between 200 mA and 250 mA (Figure 3.18b and Figure 3.18c), besides an increase of the DC level, the traces show clearly a train with a single pulse per round-trip with a FWHM of 100 ps and a repetition time of approximately 37.5 ns corresponding to the approximate length of 7 meters of the cavity. At a current value of 345 mA, close to the jump observed in the LI curve, the trace switches to a configuration with multiple pulses per round-trip (see Figure 3.18d) which turns into a complicated and unclear dynamics at 500 mA. As indicated by the LI curve, no remarkable differences are observed when decreasing the current.

The spectrum of the total signal for each trace in Figure 3.18 is represented in Figure 3.19, being possible to identify each temporal trace with its corresponding

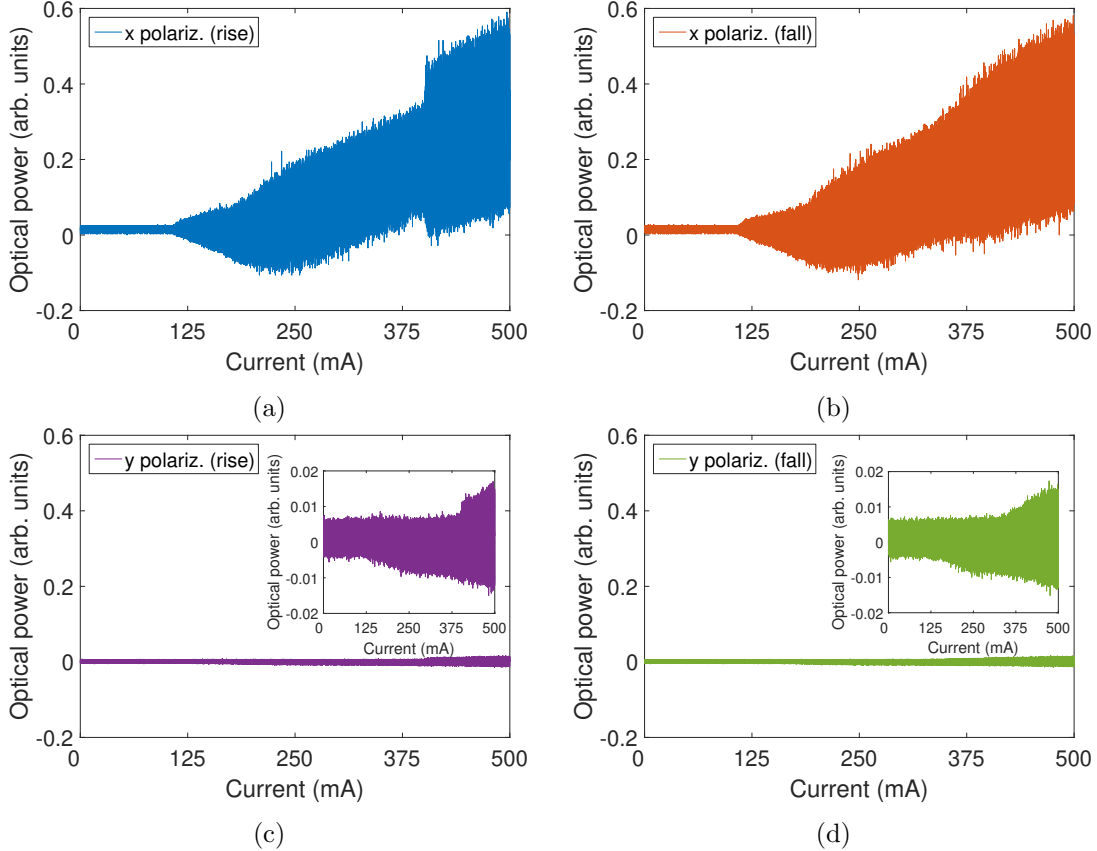


Figure 3.17: LI curve by reinjection of an elliptical state of light obtained by setting the half-wave plate at  $11^\circ$  with respect to the case of  $y$ -polarization. a) Detection of the  $x$ -polarization component of the laser emission when the current is increased from 0 mA up to 500 mA. b) Detection of the  $x$ -polarization component of the laser emission when the current is decreased from 500 mA down to 0 mA. c) Detection of the  $y$ -polarization component of the laser emission when the current is increased from 0 mA up to 500 mA. d) Detection of the  $y$ -polarization component of the laser emission when the current is decreased from 500 mA down to 0 mA.

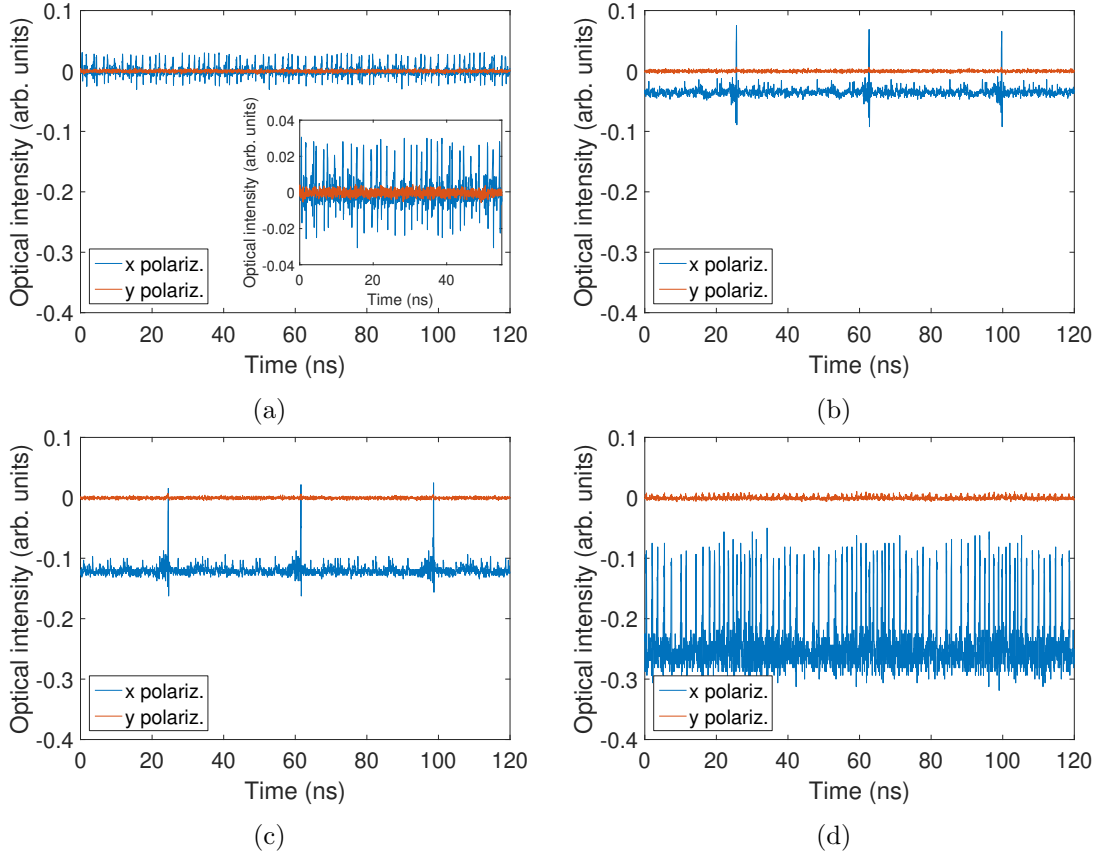


Figure 3.18: Temporal traces by reinjection of an elliptical state of light obtained by setting the half-wave plate at  $11^\circ$  with respect to the case of  $y$ -polarization and varying the current to a) 130 mA (detail of one round-trip in the inset), b) 200 mA, c) 250 mA and d) 345 mA.

spectrum. It is observed that the appearance of the pulses is associated with a broadening of the spectrum indicating the contribution of many modes as it is usual in mode-locked systems. It is worth noting the emergence of a small shoulder at the red side of the spectrum as it seems to have a big impact on the regularity of the trace and the number of pulses per round-trip.

The laser continues emitting pulses for the reinjections performed in the whole range of tested angles between  $11^\circ$  and  $3^\circ$ . However, as the angle (or equivalently the

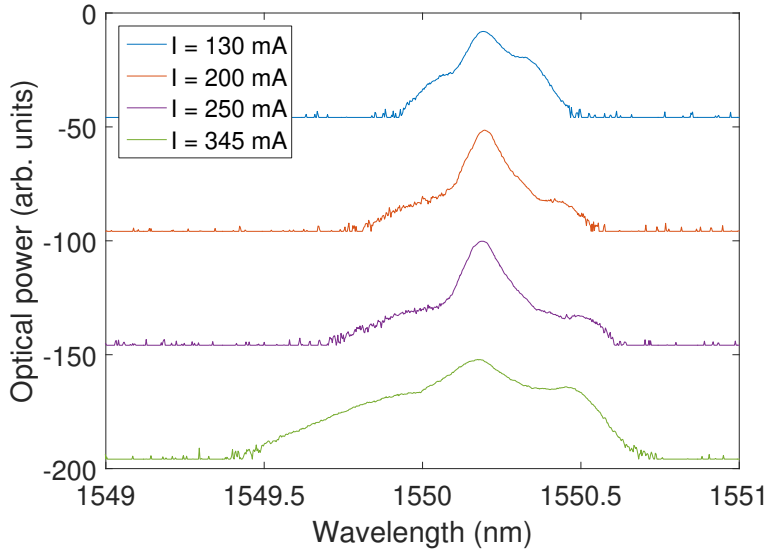


Figure 3.19: Optical spectra obtained by reinjection of an elliptical state of light achieved by setting the half-wave plate by  $11^\circ$  with respect to the case of  $y$ -polarization and varying the current to 130 mA (blue), 200 mA (orange), 250 mA (purple) and 345 mA (green).

ellipticity) is decreased, the behavior of the system becomes, in general, less predictable and shows noticeable differences even for very small variations of the ellipticity. This is clearly observed for low angles values of the half-wave plate close to  $3^\circ$ . In this case, tiny variations of the angle of the half-wave plate –even below the instrumental error of the controller– have an enormous impact on the LI curves as Figure 3.20 evidences. While Figure 3.20a and Figure 3.20c already show differences in comparison with Figure 3.16 –such as the cut from 375 mA on where no dynamics is observed– the LI curve of Figure 3.20b and Figure 3.20d corresponding to the reinjection at tiny variation of the angle below the instrumental error of the controller shows a much more complex LI curve with different regimes. In both cases, some emission is also observed in the  $y$ -polarization.

The temporal traces also reveal a pulsed emission for the situations just described although they suffer in both cases from a lack of the regularity shown in the traces for the reinjection at  $11^\circ$ . In order to illustrate this, Figure 3.21 shows the temporal traces matching different current values of the LI curve depicted in Figure 3.20a and Figure 3.20c. In this case, no remarkable dynamics appears even when the current is

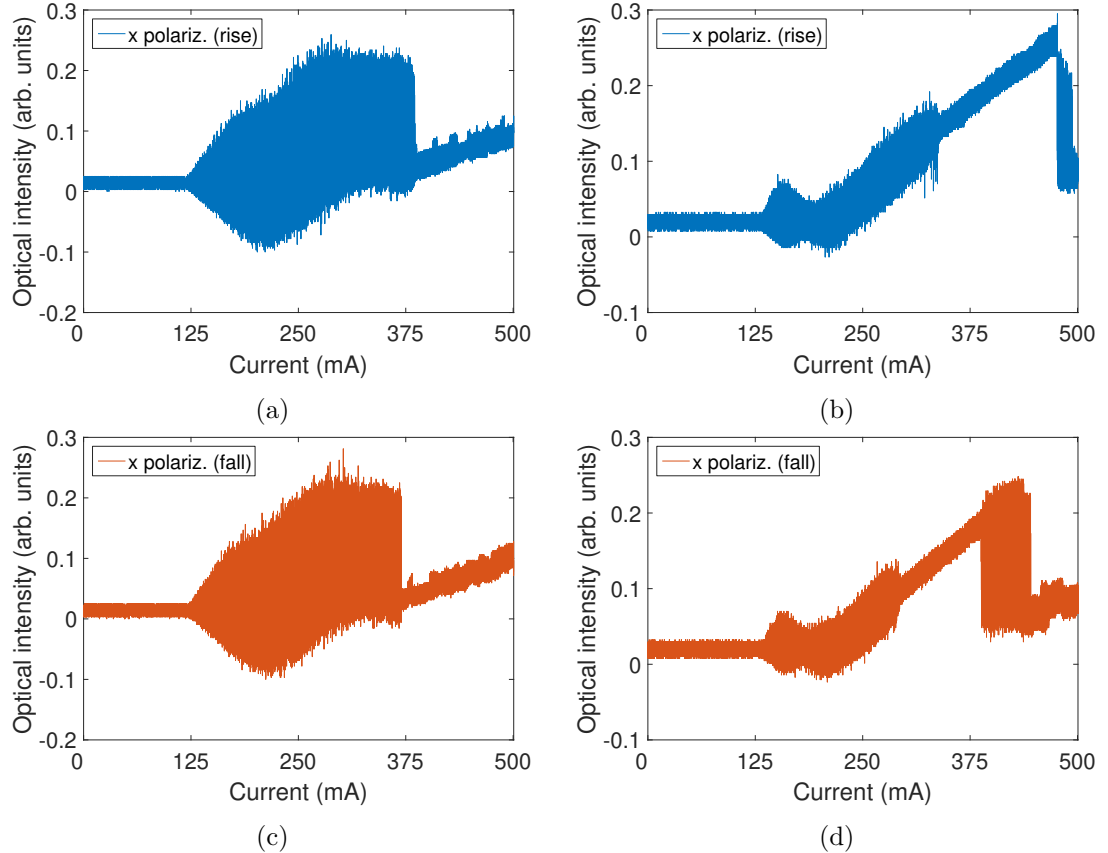


Figure 3.20: Severe differences in two LI curves accomplished by reinjecting two close elliptical states of light obtained by setting the half-wave plate at  $3^\circ$  with respect to the case of  $y$ -polarization reinjection (detection of the x polarization component of the laser emission represented for the a) rise and c) fall of the current) and a tiny angle variation below the instrumental error of the controller with respect case of  $3^\circ$  (detection of the x polarization component of the laser emission represented for the b) rise and d) fall of the current).

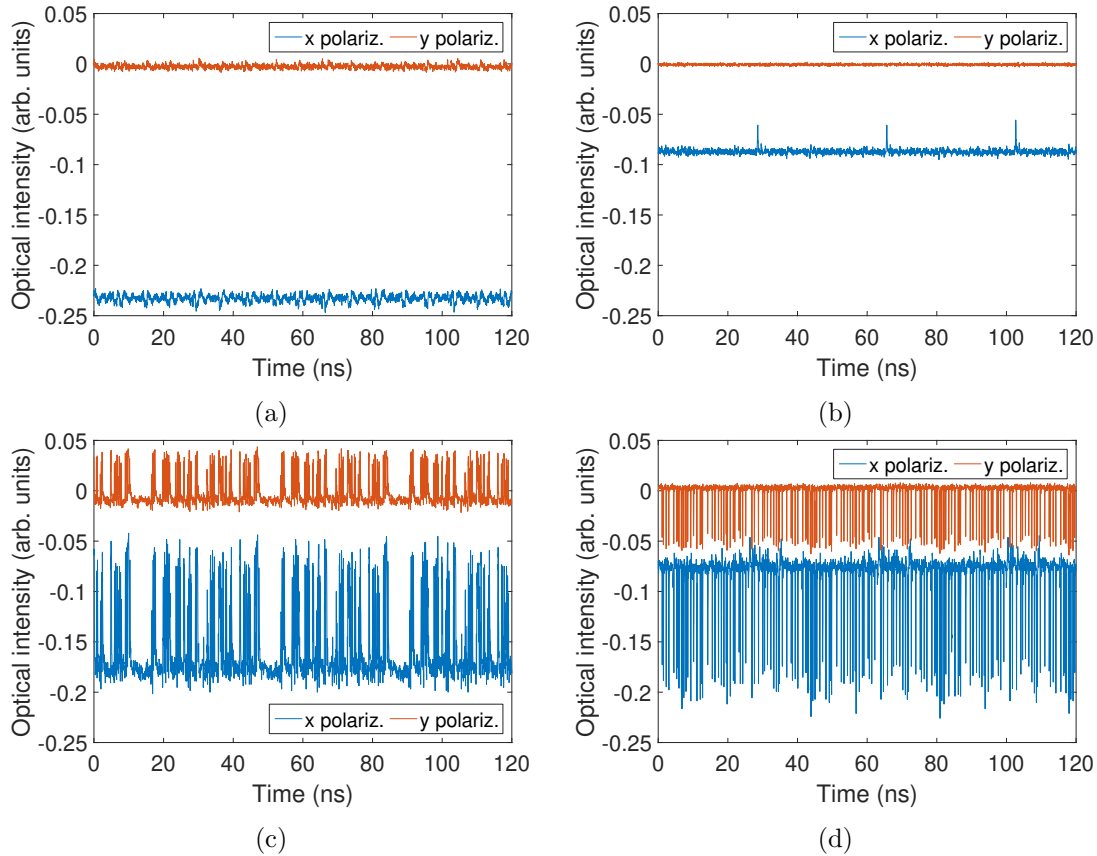


Figure 3.21: Temporal traces corresponding to the LI curve shown in Figure 3.20b and Figure 3.20d obtained for current values a) 460 mA, b) 500 mA, c) 430 mA and d) 400 mA.

raised up to 460 mA and only at 500 mA a regular trace of pulses of low amplitude at the corresponding round-trip time of 37.5 ns appears. However, the lowering of the current up to 430 mA destabilizes the temporal trace and the system begins to emit also in the  $y$ -polarization. Although not shown in the figure, when lowering the current down to 400 mA, the system shows bursts of pulses with a certain regularity given by the round-trip time. However, the complexity of the dynamical behavior of this system is really revealed when raising the current back from this point up to 460 mA. Although it would be expected to retrieve the situation with no dynamics

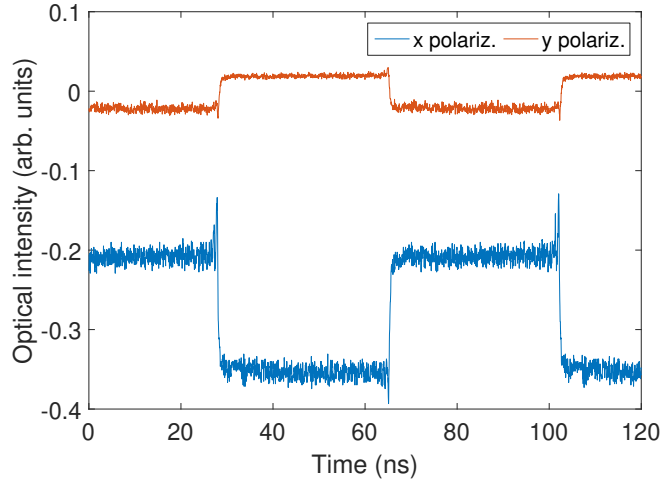


Figure 3.22: Temporal trace showing a square wave generated by a reinjection performed with a random position of the paddles of the controller.

shown before for this same value of current, in this case, the hysteresis of the system does not allow to reach that state again and the system keeps lasing bursts of bright pulses in both polarization components. However, if the current is lowered below 430 mA, these bright pulses transform to dark pulses which remain for currents down to 400 mA although the pulsing dynamics disappears for lower current values. Hence, as long as the pulsing dynamics is kept, it is possible to switch at will between bright and dark pulses by setting the current above or below the mentioned 430 mA.

At this point it has to be mentioned that the complexity of the dynamics offered by the system overcomes the capability on the control of the polarization offered by the in-line fibered controllers given their previously mentioned inherent limitations linked to their low repeatability, the imprecision of the values of the waveplates, the asymmetrical behavior and inaccuracy of the angles turned by the paddles and the dependence of the birefringence of the fiber with the temperature. Nevertheless, the dynamics shown by the pulses generated by the SOA fibered laser is extremely rich as evidenced when reinjecting random polarization states of light which result in the emission of square waves (see Figure 3.22), current-controlled regimes with different number of pulses per roundtrip (see Figure 3.23), multistability of states for the same parameters values (see Figure 3.24) and interaction of pulses (see Figure 3.25). Unfortunately, the limitations established by the in-line fibered polarization controllers prevent the full control of the polarization which is required for the correct study and

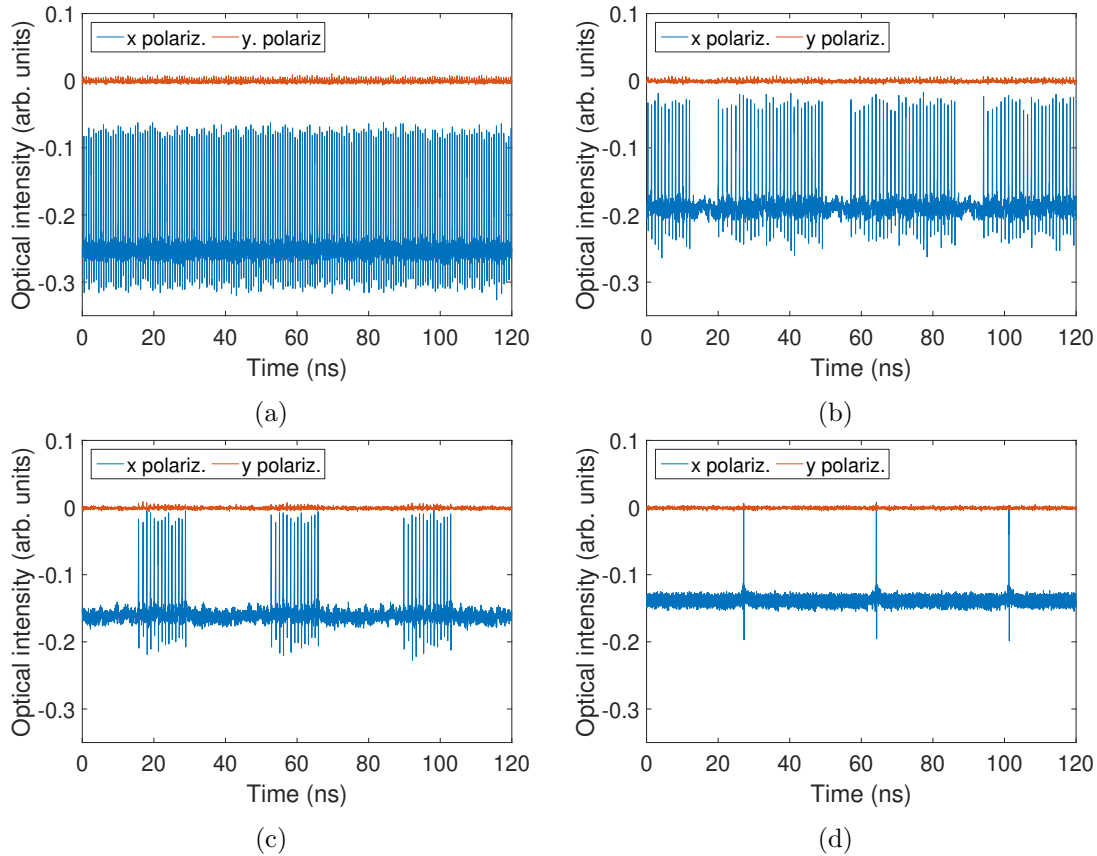


Figure 3.23: Temporal traces obtained by a reinjection performed with a random but fixed position of the paddles of the controller at a) 311 mA, b) 270 mA, c) 250 mA and d) 230 mA.

understanding of the pulsed emission states derived from the reinjection of different polarization states of light.

In order to operate the system beyond the limitations imposed by the control of the polarization in fiber, polarization controllers operating in air as those shown in Figure 3.5b are used. As previously explained, these controllers consist in a fiber input port coupled to an optical collimator which sends light propagating in air towards three rotating waveplates (a central half-wave plate and two external quarter-wave plates). The protractors incorporated to the waveplates and the reduction of the

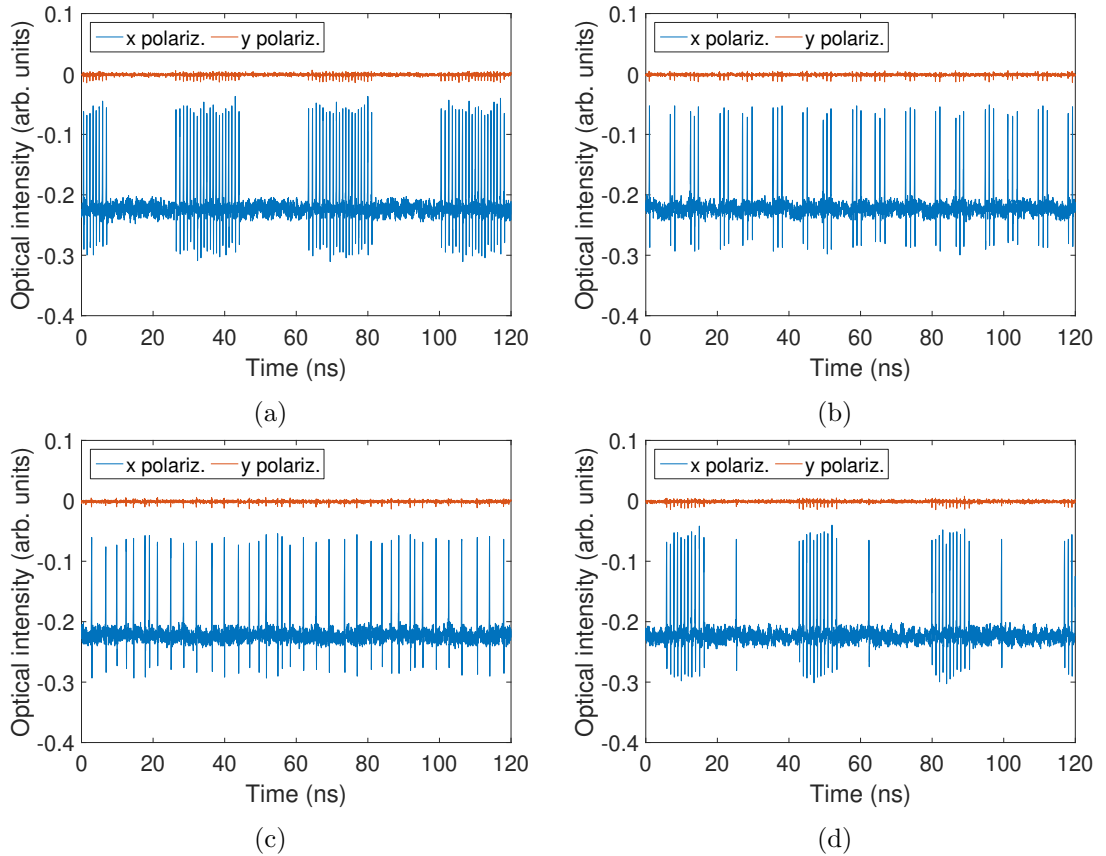


Figure 3.24: Temporal traces showing a multiplicity of coexistent states for a fixed set of parameters values at a current of 287 mA.

sensitivity with the temperature allows for a much more accurate management of the polarization. After selecting the desired polarization for the light, it is sent towards a second collimator present in the output port and the light is coupled back to the optical fiber.

The waveplates of the fiber bench have been tested in an open cavity as previously explained in Section 3.2 to check their performance. Furthermore, the previous bandpass filter has been substituted by a new optical filter (OZOptics DTS0051) showing a resolution of less than 0.1 nm, a tuning range of 50 nm around 1550 nm, a FWHM of 1.1 nm and coupled in this case to PM fibers to minimize evolution of the polarization

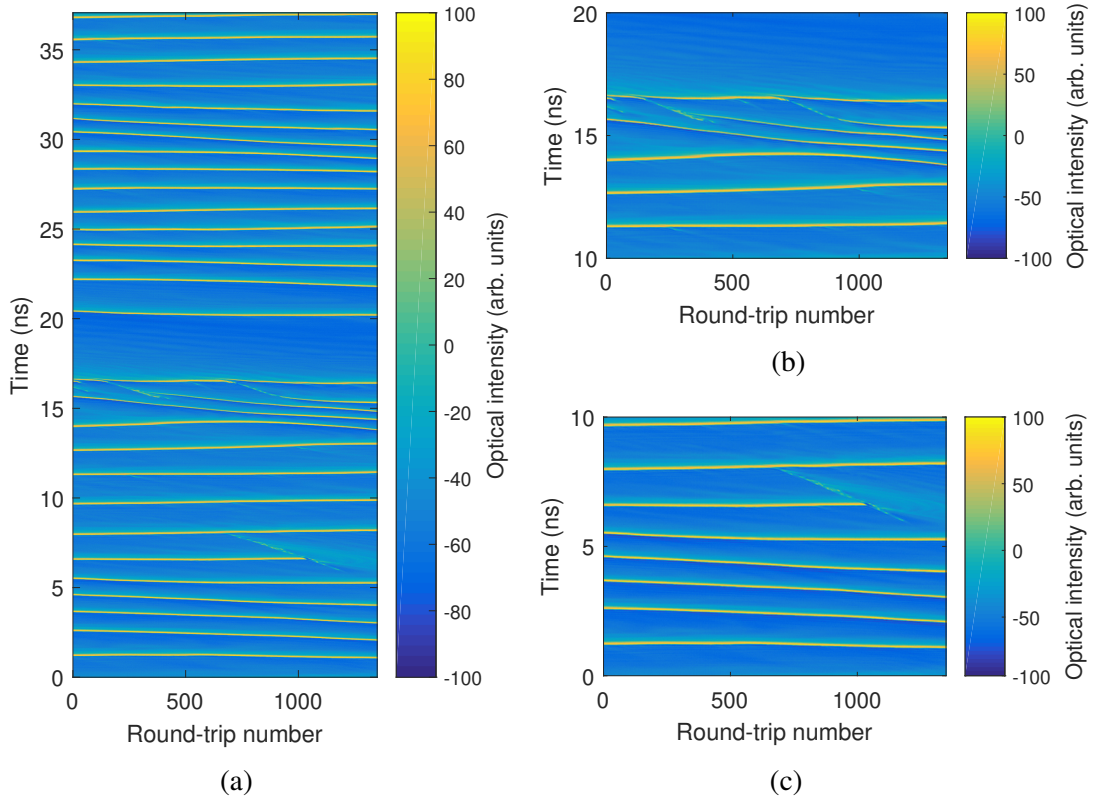


Figure 3.25: Space-time diagram showing the evolution of pulses generated by a random position of the paddles of the in-line fibered polarization controller. a) Piling of 1482 round-trips of 37 ns. b) Detail of a) where the generation of 2 pulses occurs in round-trips 150 and 700. c) Detail of a) showing the cancellation of one pulse in round-trip 1025.

along the cavity. Hence, the fiber laser cavity is completely built on PM fiber with the exception of the section where the fiber bench is present.

The tests performed on the control of the polarization by the waveplates of the fiber bench have demonstrated to be correct although an error of approximately  $5^\circ$  is detected for the angles at which the waveplates are positioned with respect to the effects observed in the polarization. For example, given that the SOA emits almost all the ASE on the  $x$ -polarization, it would be expected that the incoming signal of the SOA would be unaffected and maximal when the three waveplates present

simultaneously an angle of  $0^\circ$ . However, the maximal output signal from the fiber bench is obtained for a combination of angle values corresponding to  $357^\circ$  for the first quarter-wave plate,  $0^\circ$  for the central half-wave plate and  $2^\circ$  for the last quarter-wave plate. Keeping in mind the existence of this small error, the transformations of the polarization state from  $x$  to  $y$ -polarization is correct when the half-wave plate is turned from  $0^\circ$  to  $45^\circ$  and the periodic alternation between these two polarization states with each turn of  $45^\circ$  is clearly observed throughout the complete turn of  $360^\circ$ . As expected, a circular polarization state for the light is observed when the half-wave plate is set at an angle of  $22.5^\circ$  (half the value of  $45^\circ$ ) or any multiple of  $90^\circ$  that could be added to the previous value of  $22.5^\circ$ , this is to say, the circular polarization state is also achieved when setting the half-wave plate at  $112.5^\circ$ ,  $202.5^\circ$  and  $292.5^\circ$ . Instead of turning the half-wave plate, the circular polarization state can also be reached by setting the quarter-wave plate at  $45^\circ$  (also at  $135^\circ$ ,  $225^\circ$  and  $315^\circ$ ). In this case, by completing the turned angle of the quarter-wave plate up to  $90^\circ$  the linear  $x$ -polarization signal is recovered (also for  $180^\circ$ ,  $270^\circ$  and  $360^\circ$ ). Thus, even with the presence of the small error previously mentioned for the setting angles of the waveplates, the behavior of this kind of polarization controllers has demonstrated to be much more repeatable, robust, deterministic and reliable than that of the in-line polarization controllers although they are also prone to present higher losses due to the fact that light propagates in air and there might exist possible mismatches in the alignment of the collimators. Hence, given the advantages and disadvantages presented by each type of polarization controller, the final choice is determined by the demands of the specific applications.

The goal on using this fiber bench is to study in a repeatable manner the casuistics observed for the in-line polarization controller in those cases in which the signal sent to the SOA consists on a small perturbation of the  $x$  into  $y$ -polarization reinjection. In other words, the purpose is to clarify the big differences observed in the dynamics of the laser when the ellipticity of the reinjected signal is slightly varied by a difference of  $1^\circ$  of the angle of the half-wave plate. In this case, given that the whole cavity is now made using PM fiber and that the tests performed on the fiber bench have demonstrated the correct operation of the wave plates, it is possible to reduce the complexity on the management of the polarization controller by removing the two quarter-wave plates and using only the half-wave plate to change between the two orthogonal polarization states and to vary the ellipticity of the light.

Unfortunately, the characterization has been not possible as it has been realized that, although the filter is coupled to PM fiber, the internal design of the filter does not maintain the polarization. On the contrary, turning the micrometer of the filter for the variation of the operating wavelength changed the polarization state of the light to an undetermined state. In fact, the polarization effects are so relevant that

the system is able to emit pulses by turning the micrometer of the filter even when the cavity is closed without any polarization controller on it, what makes impractical the study of the problem in terms of the control of the polarization.

The difficulties encountered on the management of the polarization compelled us to look for new and more controllable geometries for the optical cavity. The final design of the fiber laser and the results obtained will be described in the following chapter.

### **3.5 Proof of principles: fibered SOA laser pulses for LiDAR measurements**

Although the specific details on the process of generation of the pulses originated by the different configurations of the fibered SOA ring laser shown in this chapter are hard to determine due to all the technical limitations concerning to the precise control of the polarization in fiber, one thing that is clearly observed without a doubt from the experimental results is that once that a stable and regular pulsing state is achieved, the duration of such a pulse train reaches in many cases the order of magnitude of the hour what allows to think on the capacity of these pulses to perform LiDAR measurements.

As a practical application, the utility of these pulses for the performance on the remote sensing of distances it is assessed. The measurement of distances can be performed with simple minor modifications at the setup previously shown in Figure 3.14. Once that the pulses are obtained according to the operation of the ring laser described in the previous section, the polarization controller at the detection branch is no longer needed and it can be substituted by a 50%-50% coupler that splits the outgoing signal. One of the pigtail of the coupler sending a half of the signal is directly connected to the photodetector D1 which detects the pulse train trace –used as temporal reference– while the other pigtail of the coupler transmitting the second half of the signal is attached to a replaceable fiber patch cord which is connected to the photodetector D2. The variation on the setup is depicted in Figure 3.26. Although the length of the electrical cables connecting D1 and D2 to the oscilloscope is not exactly the same and cause a default delay between the signals, this delay has been adjusted in the oscilloscope to set the same temporal reference for both signals. Hence, the increase of length introduced by the patch cord on this second branch with respect to the length of the pigtail fiber of the first branch –used as reference– provoke the retardation of the pulses which is observed in the oscilloscope.

By measuring the time lapsed between the reference and the delayed trace it is possible to infer the length of the patch cord which is, in essence, the principle of TOF LiDAR measurements. The measurements are performed for different lengths

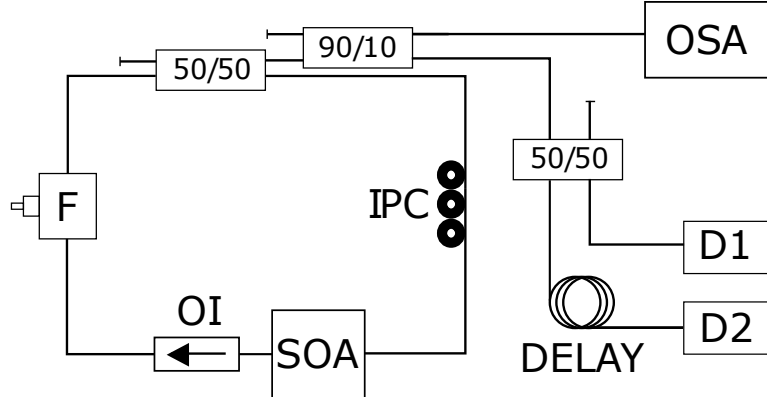


Figure 3.26: Modification of the detection branch of the experimental setup of Figure 3.14 for the demonstration of the proof-of-principles of LiDAR measurements (see text for a complete description). Same acronyms than those in Figure 3.14

of the replaceable patch cord and the results are shown in Figure 3.27. In this case, different pulse delays are produced for a variety of patch cords lengths with nominal lengths of 0 m, 1 m, 2 m, and 5 m. The length of the patch cord can be determined from the simple equation  $L = c\tau/n$ , where  $c$  is the speed of light in vacuum,  $n$  is the refractive index of the optical fiber and  $\tau$  is the time delay of the pulses with respect to the reference trace measured in the scope. Here, the values of  $\tau$  measured correspond to 5.2 ns, 10.1 ns, and 24.7 ns leading to length calculated values of the patch cord of 1.04 m, 2.02 m, and 4.94 m respectively. Intermediate nominal fiber length for the branch causing the delay can also be obtained by attaching a patch cord of 0.5 m, or even shorter, as long as the length is compatible with the existing technical limitations when fabricating very short fibers. In order to know the delay introduced by any other fiber length, a linear regression has been performed using these experimental points which is represented by the orange line in Figure 3.28. The blue line shows the expected theoretical line assuming a standard refractive index for silica fiber of 1.5 which, in fact, is quite close to the calculated value of 1.48 obtained by means of the slope value provided by the linear regression previously performed. In this case, the set of experimental measurements (green dots in Figure 3.28) have been accomplished at a bias current for the laser of 170 mA and show an average standard deviation of approximately 70 ps. These same measurements have been reproduced at bias currents of 200 mA and 250 mA with no significant differences in the values

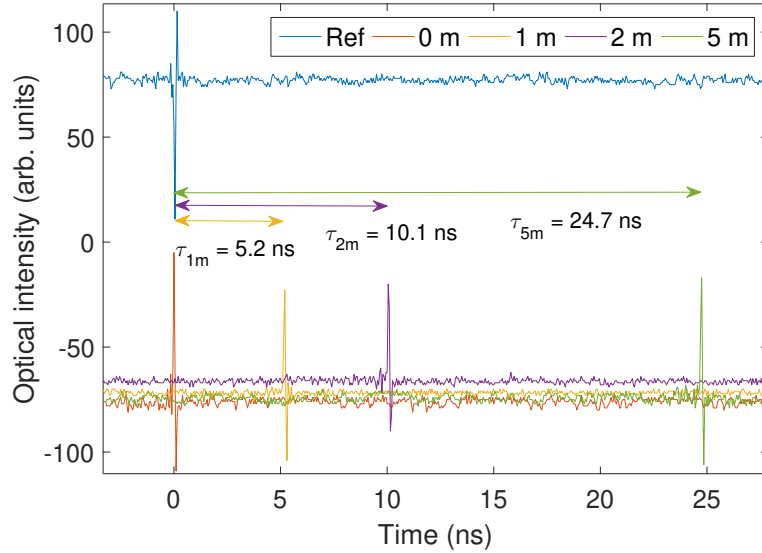


Figure 3.27: Delay times produced on the temporal trace by patch cords of different length. The blue line stands for the reference trace while the orange, yellow, purple and green lines show respectively the traces for patch cord lengths of 0 m, 1 m, 2 m, and 5 m.

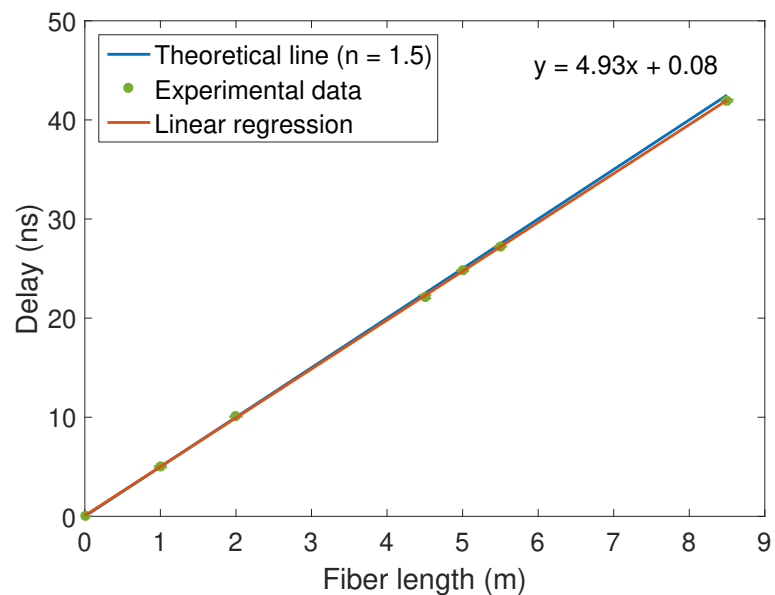


Figure 3.28: Temporal delay experienced by the optical pulses as a function of the length of the replaceable patch cord described in 3.26. The green dots stand for the experimental points while the orange line shows the linear regression of the data and the blue line represents the theoretical delay line calculated for a standard refractive index for silica fiber of 1.5.

obtained from the linear regression. It is important to note that all the previous set experimental measurements are related to the concept of aliasing given that a patch cord length of 8.5 meters offers a delay of approximately 42.5 ns but, as the round-trip time of the ring cavity is approximately 37.5 ns, that means that the first pulse of the delayed branch will appear just 5 ns after the second pulse of the reference branch and it might be confused with the pulse delayed by the 1 meter patch cord. Of course, enlarging the cavity solves the problem but some method to avoid this measurement dependency on the cavity length would be desirable.

## **3.6 Conclusions to the Chapter**

In this chapter, a semiconductor-based unidirectional ring laser has been designed with the purpose to adapt the setup consisting on a VCSEL and an RSAM coupled in a Fabry-Pérot external cavity described in Chapter 2 to optical fiber in order to take advantage of the benefits offered by the optical fibers and overcome the limitations found in the previous system in terms of cavity length which hinder the study of the LS observed in the VCSEL-RSAM setup.

For the fibered version realized here, instead of the VCSEL, a fibered SOA emitting at 1550 nm pumped by electrical current has been used together with a fibered version of the RSAM and a tunable fibered optical filter to select a particular operating wavelength given the broadness of the gain curve of the SOA. Each the optical device has been individually characterized before realizing the interconnection of all the components, including the SOA and the RSAM whose temperatures are controlled by their corresponding TECs.

In the first place, these components have been connected through an optical circulator conforming a unidirectional ring cavity configuration with a total length of approximately 10 meters. After a proper setting of the parameters, the system has been electrically pumped presenting the threshold at 80 mA while the pulsing regimes appear in a range of currents between 100 mA and 391 mA. All the pulse states show an underlying repetition time of 53.5 ns in correspondence with the cavity length. However, the traces remain temporally unstable alternating between a multiplicity of coexisting states for a fixed current and parameters values what is attributed to mechanical perturbations and thermal fluctuations which, as known, are able to induce changes in the birefringence of the optical fibers and affect to the state of polarization of light. Consequently, this configuration for the setup, although able to produce pulses, cannot be easily manipulated due to the difficulties on the control of the factors mentioned.

Hence, the exploration and control over the polarization in the system have been incorporated by means of in-line polarization controllers. The capability of the fibered SOA ring cavity to generate pulses have been demonstrated by reinjecting the main polarization of the SOA – $x$ -polarization– rotated by  $90^\circ$  presenting a small degree of ellipticity instead of being perfectly linear. In these situations, very regular trains of short pulses with large amplitude and a FWHM of approximately 100 ps are obtained with a repetition period given by the cavity round-trip time. It has been also shown that these pulses can be potentially used in remote sensing by performing a simple TOF study. However, again technical limitations emerged from the fact that the in-line polarization controllers offer the possibility of changing the polarization state of light but not in a well-controlled manner and with a lack of the necessary robustness, repeatability, and precision. In fact, it has been shown that a difference as small as  $1^\circ$  in the configuration of the polarization controller induces an extremely different dynamical behavior.

Finally, a second kind of polarization controller in which light propagates in air and allows the deterministic management of the polarization state has been used. It has been connected to a different filter working under the same scheme but coupled to PM optical fibers. However, the variations on the optical filter produced by turning the micrometer for the selection of different wavelength also affected to the polarization making possible to obtain pulses and being, hence, extremely difficult to distinguish if the generation of pulses is due to the performance of the controller or the filter.

## Chapter 4

### Subpicosecond pulses in a self-starting mode-locked semiconductor-based figure-of-eight fiber laser

The following chapter describes the experimental achievement of self-starting and highly stable ultrashort pulses generated by an all-PM SOA based fiber laser in a F8L configuration getting rid of the management of the polarization or the presence of an RSAM for inducing the pulses. The chapter consists on the literal transcription of the article “Subpicosecond pulses in a self-starting mode-locked semiconductor-based figure-of-eight fiber laser” with the exception of a figure including a photograph of the setup which as been added in this chapter of the thesis for a better illustration of the experiment. The article is authored by **Daniel Chaparro**, Luca Furfaro and Salvador Balle and published in Photonics Research, Vol. 5, Issue 1, pp. 37-40, in February 2017 (DOI: 10.1364/PRJ.5.000037). ©2017 Chinese Laser Press. ©2017 Optical Society of America. Users may use, reuse, and build upon the article, or use the article for text or data mining, so long as such uses are for non-commercial purposes and appropriate attribution is maintained. All other rights are reserved.

**Abstract:** We have experimentally studied the mode-locking dynamics of a polarization-maintaining figure-of-eight laser which has a semiconductor optical amplifier as gain medium. Self-starting mode-locking at the fundamental repetition rate of 18 MHz is obtained at the lasing threshold, and further increasing the bias current leads to the progressive emission of additional optical pulses in each round trip and eventually to mode-locked emission at increasingly high harmonics of the fundamental repetition rate, up to 2.45 GHz. The intensity autocorrelation of the amplified mode-locked pulses has a full width at half-maximum duration of 382 fs, which corresponds to a pulse duration of 247 fs.

## 4.1 Introduction

The generation of optical pulses from a laser is an active research field due to its large application potential in a variety of domains, such as telecommunications, metrology, remote sensing, and material processing. In addition, extreme nonlinear optical effects can be explored because the pulses can be externally amplified and the high spatial coherence of the beam allows for tight focusing of the light to small transverse sections; hence extremely high peak intensities and fluences can be achieved [139].

Pulses in the picosecond range or shorter can be obtained by mode-locking (ML) of the laser [265]. The initial development of pulsed laser sources relied on solid-state lasers [139], but fiber lasers have emerged as a reliable alternative to bulky solid state lasers for optical pulse generation [140]. Besides compactness, they provide high beam quality with high efficiency, and the fibered cavity offers mechanical robustness; however, dispersion management is more problematic in fiber lasers due to fiber dispersion, and the optical powers that can be achieved in fiber lasers are usually lower than those obtained in solid-state lasers. Most fiber lasers rely on a fiber section doped with rare-earth ions, which provide gain upon optical pumping; yet, fiber lasers that use a semiconductor optical amplifier (SOA) as the gain element have also been developed, since they offer the simplicity of electrical pumping, high nonlinearity, rapid tuning, and a broad gain bandwidth [141–145].

Active ML of SOA-based fiber lasers in unidirectional ring cavities has allowed researchers to obtain optical pulses with a duration of 15 ps [146], which can be further amplified and compressed down to 50 fs [147]. Exploiting nonlinear polarization rotation of the field in the SOA, passive ML has been achieved in different situations. Yang *et al.* [148] have obtained 800 fs pulses at the fundamental ML frequency of 14 MHz in a unidirectional SOA-based fiber laser. In addition, dark and bright pulses can be obtained in a similar configuration [149]. In this case, the pulses arise from a square-wave intensity modulation that can be quite slow and that can be useful for generating optical clocks with high duty cycle, and the repetition rate of the pulses can be increased by operating the device in the harmonic ML regime. Recently, frequencies up to 12 GHz have been obtained by passive ML of an SOA-based, figure-of-eight laser (F8L) operating at 1.06  $\mu\text{m}$ , with pulses of 29 ps duration; in this case, the repetition frequency can be selected by changing the bias current in the SOA [160].

In this work, we report on self-starting ML of an F8L based on an SOA working in the CL band that does not rely on nonlinear polarization rotation for achieving ML. The cavity is defined by standard off-the-shelf polarization maintaining (PM) components, and its simplicity makes it very attractive for applications because it does not require of any polarization controller or adjustment. Optical pulses with a

duration of 247 fs have been obtained with a repetition rate that depends on the bias current into the SOA. Self-starting fundamental ML at a repetition rate of 18 MHz is obtained at the lasing threshold, and it evolves into harmonic ML up to 2.45 GHz upon increasing the bias current in the SOA.

## 4.2 Experimental Setup

The experimental setup is schematically shown in Fig. 4.1. The F8L cavity is defined by two PM fiber loops coupled through a 50:50 PM fiber coupler. One of the loops (length  $L_1 \approx 6$  m) is purely passive, and it includes a PM optical circulator that imposes unidirectional operation of the loop. The other loop (length  $L_2 \approx 5$  m) includes a single-transverse-mode PM fiber-coupled SOA. The amplifier is strongly dichroic, with a difference of 18 dB in the polarized power levels emitted by amplified spontaneous emission, and it provides an optical gain bandwidth of 80 nm around a wavelength of 1550 nm for the dominant polarization. The SOA (Thorlabs BOA1004P) is thermally stabilized to better than 0.1°C, and it is driven by a stable current source. The laser output is split in two branches. One of them directs 10% of the output toward an optical spectrum analyzer (OSA, HP 86142A). The remaining 90% of the output is sent to a fiber-coupled amplified photodetector (New Focus 1544B) whose output is divided by a Radio-Frequency (RF) 3 dB coupler connected directly to a real-time digital oscilloscope (Agilent Infinium DSO 81204A) and to an RF spectrum analyzer (Anritsu MS2602A) after being amplified by an RF amplifier (Nucléitudes ALC2250). Autocorrelation measurements have been performed when possible by further splitting this branch in two; in one of these branches we insert another optical circulator followed by a PM erbium-doped fiber amplifier (Amonics, AEDFA-PM-CL-17-B-FA providing up to 17 dB gain over the C or L bands) that is used to amplify the laser output, which is finally sent to a background-free optical autocorrelator (Femtochrome Research Inc., FR-103HS).

## 4.3 Experimental results

Figure 4.2 displays the light-current characteristics of the F8L when the substrate temperature of the SOA is set at 20°C, as recorded with a power meter. Increasing the bias current  $I$  into the SOA, the lasing threshold occurs at  $I = I_{th} \simeq 90$  mA, and the emitted average power starts growing, reaching 0.6 mW—which corresponds to an intracavity optical power around 12 mW—for a bias current  $I = 340$  mA. The LI curve presents a slight hysteresis close to threshold, and the F8L does not switch off until the

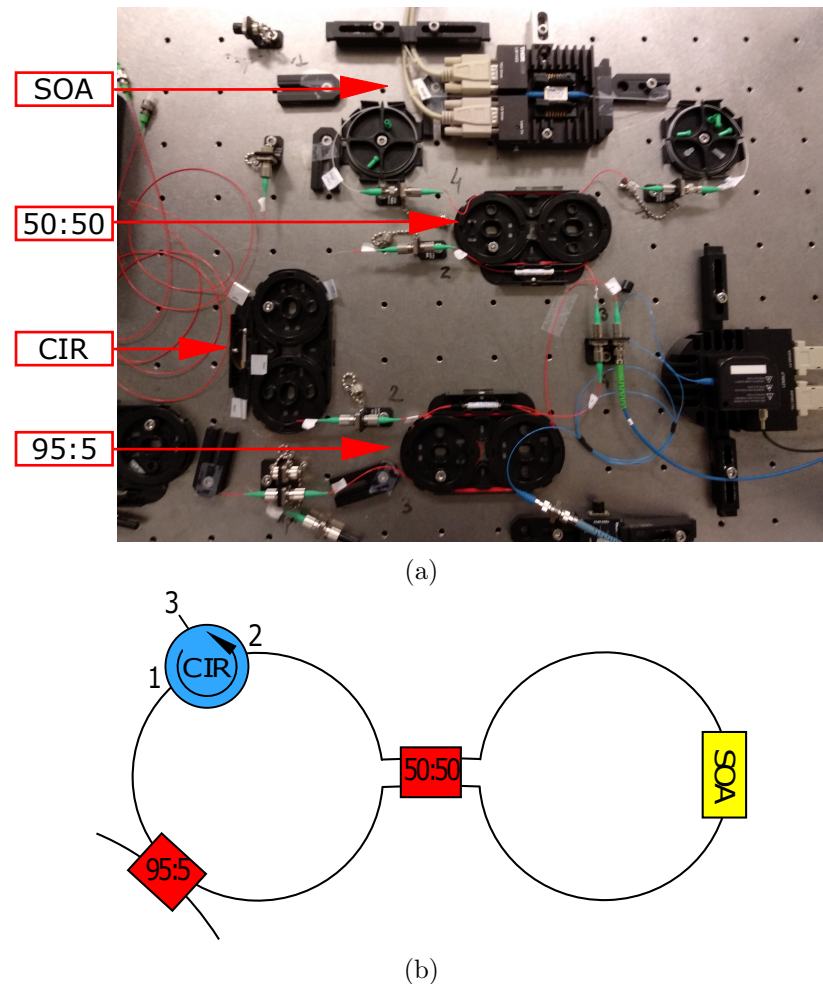


Figure 4.1: a) Photograph of the F8L experimental setup used for the generation of pulses. b) Schematics of the F8L setup. CIR, optical circulator. 50:50 and 95:5: fiber couplers that divert 50% and 5%, respectively. All elements are PM.

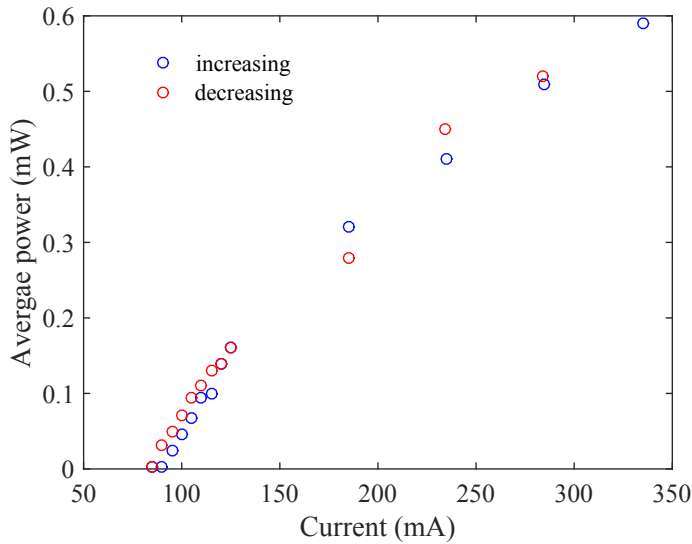


Figure 4.2: Output power of the F8L when the substrate temperature is  $T = 20^\circ\text{C}$  as the bias current of the SOA is increased (blue) and decreased (red).

bias current applied to the SOA is reduced below 85 mA; indeed, for currents below 120 mA, the power emitted is higher on the decreasing branch than on the increasing one.

The optical spectra for several values of the bias current are shown in Fig. 4.3. At threshold ( $I = 95$  mA) the F8L has an optical spectrum centered at a wavelength  $\lambda \simeq 1575$  nm. In this regime, the optical spectrum is rather broad ( $\approx 25$  nm full width at half-maximum, FWHM), and it exhibits some ripples that are more pronounced on the red wing of the spectrum, which we attribute to the residual reflectivities of the SOA facets and connectors in the setup—a similar ripple is observed in the optical spectrum of the amplified spontaneous emission of the SOA when the bias current is above 500 mA. However, the mode spacing of the F8L cavity is  $\approx 18$  MHz, far too small to be resolved by the OSA. The optical spectrum remains essentially unaltered as the current is increased up to  $I = 110$  mA. For this current value, a peak appears on the red wing of the spectrum at wavelength  $\lambda \approx 1584$  nm, the modulation of the spectrum becomes clearer, and the FWHM of the spectrum reduces to  $\approx 3$  nm. Further increasing the current leads to a redshift of the dominant frequency up to  $\lambda \approx 1591$  nm for  $I = 285$  mA, but the FWHM of the spectrum does not change noticeably. In all

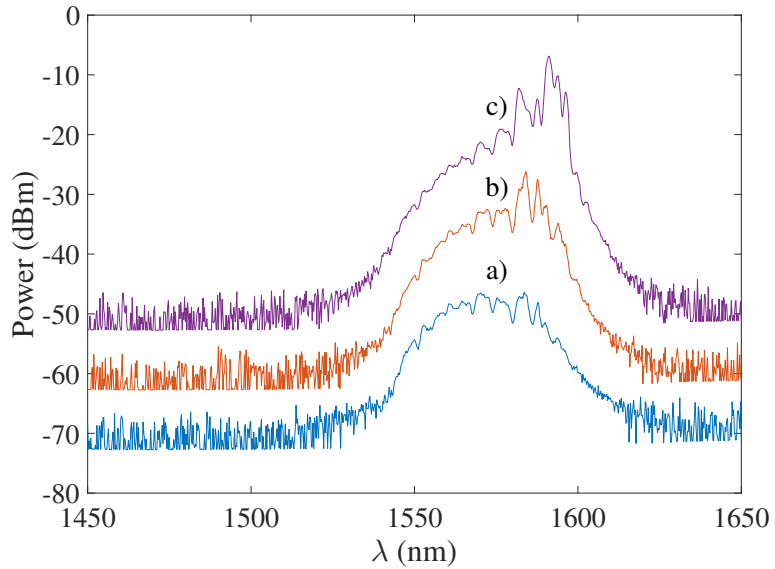


Figure 4.3: Optical spectra of the F8L output when the substrate temperature is  $T = 20^\circ\text{C}$  for bias currents a)  $I = 95 \text{ mA}$ , b)  $I = 110 \text{ mA}$  and c)  $I = 285 \text{ mA}$ .

cases, the optical and RF spectra of the system were stable over tens of minutes.

In the time domain, the former optical spectra correspond in most cases to the emission of regular trains of optical pulses, as shown in Figs. 4.4 and 4.5. Close to the lasing threshold, Fig. 4.4, the laser output exhibits a regular train of short pulses with a period of  $\approx 56 \text{ ns}$  that corresponds to the roundtrip time in the F8L cavity; on the oscilloscope screen, the pulses appear to have an FWHM of  $\approx 70 \text{ ps}$ , which is the minimum pulse width that can be achieved with the detection bandwidth available in our system. This emission state corresponds to the fundamental passively mode-locked state of the system, and it occurs spontaneously. Its RF spectrum is displayed, with different degrees of frequency resolution, in Figs. 4.4(b)–4.4(d). The fundamental frequency of the RF spectrum occurs at 18.0623 MHz and exhibits 50 dB signal to noise ratio, typical of semiconductor lasers [266, 267]. A flat comb of replicas of this peak is observed within 5 GHz. Indeed, the comb covers the full bandwidth of the RF spectrum analyzer, although its amplitude decreases above 5 GHz due to the bandwidth limit of the RF amplifier.

Further increasing the current leads to the appearance of new pulses within the round trip. Although the pulse heights change when the pulse number increases, their temporal profile on the oscilloscope screen remains unchanged. Close to the threshold,

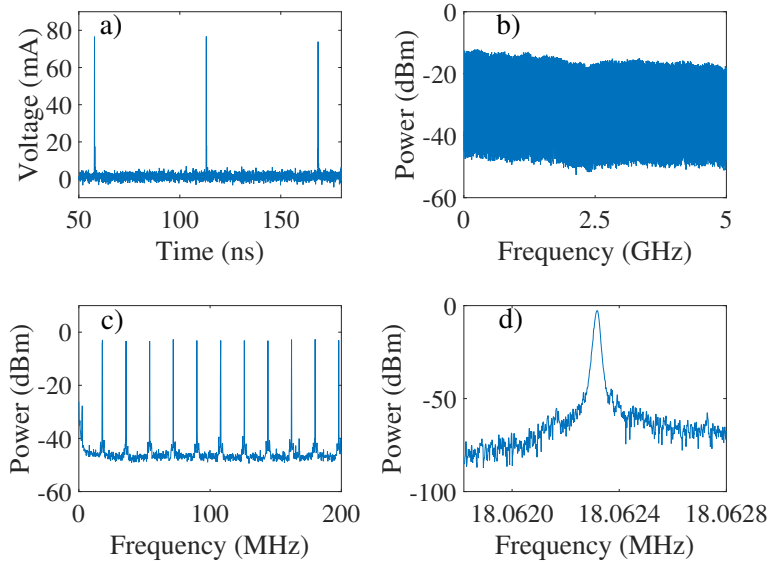


Figure 4.4: a) Time trace of the fundamental mode-locked emission of the F8L when the substrate temperature is  $T = 20^\circ\text{C}$  and the bias current  $I = 85.2 \text{ mA}$ . b) RF spectrum of the pulse train obtained for the fundamental ML regime in the 0-5 GHz range. c) Detail of the RF spectrum in the 0-200 MHz range. d) Zoom around the fundamental peak of the RF spectrum at frequency  $\sim 18 \text{ MHz}$ .

the coexistence of an increasingly large number of states with different numbers of pulses per round trip arranged in a multiplicity of forms is observed, but for still higher bias currents, different harmonic passively mode-locked states set in and remain stable for large current intervals [see Fig. 4.5(a)]. We have obtained stable repetition rates up to 2.45 GHz, which correspond to the 136th harmonic of the fundamental repetition rate. The RF spectrum of each of these states is shown in Figs. 4.5(b)—4.5(e). Again, a clear comb can be seen, with decreasing amplitude above 5 GHz due to the amplifier bandwidth limit, indicating that the pulse width is rather shorter than 100 ps.

In our case, the rather low optical power emitted by semiconductor lasers does not allow performing a direct autocorrelation measurement, and amplification of the pulse train is required, as is often the case when dealing with semiconductor lasers [266–268]. However, the optical spectra of the emission from the F8L lies precisely at the transition from the C-band to the L-band; hence amplification through our fiber amplifier will distort the pulse shapes rather strongly, and autocorrelation measurements will

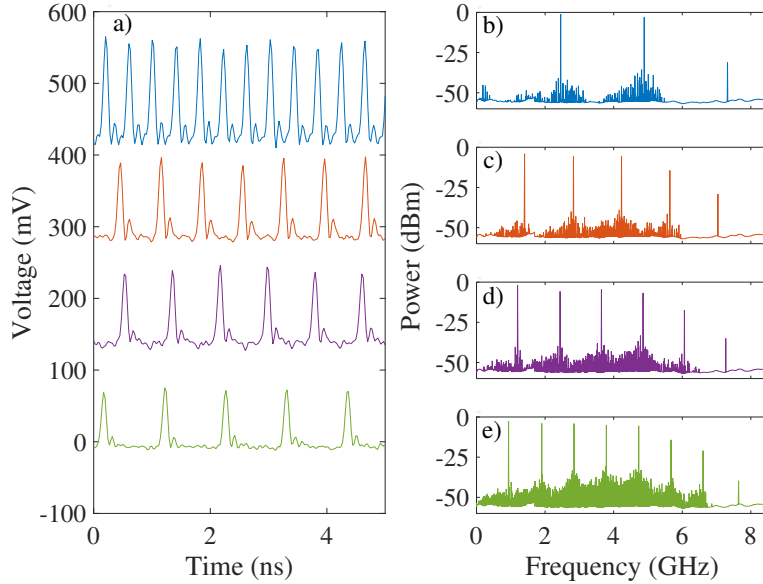


Figure 4.5: a) Time traces of the F8L emission when the substrate temperature is  $T = 20^\circ\text{C}$  for different values of the bias current close to the lasing threshold. From top to bottom,  $I = 201.5, 113.5, 102.8$  and  $93$  mA. The traces have been offset by 100 mV for clarity. b-e) RF spectra from 0-8.5 GHz of the pulse trains in panel a).

not be meaningful. In order to measure the pulse width, we have set the substrate temperature of the SOA to  $40^\circ\text{C}$ ; hence the operation wavelength of the laser is redshifted to 1580 nm or higher, that is, well within the L-band. Figure 4.6 displays the main characteristics of the pulse train when the bias current in the SOA is set to 204 mA: the optical spectrum [blue trace in Fig. 4.6(a)] presents a rather triangular form with maximum power at 1596 nm and a spectral FWHM of  $\sim 7$  nm. The pulse train has a period of  $\sim 700$  ps that corresponds to a dominant frequency in the RF spectrum of  $\sim 1.43$  GHz, with clear harmonics; note however that in this case the pulse train presents some degree of amplitude modulation that manifests as an increased noise floor around the peaks in the RF. This modulation of the pulse amplitude is induced by the proximity (in terms of bias current) of the mode-locked state with frequency  $\sim 1.4$  GHz that is portrayed in Figs.4.6(a)-4.6(c). Further increasing the current reduces the modulation amplitude, but the SOA has not been set at very high current in order to avoid damage in the device as the substrate temperature is rather high.

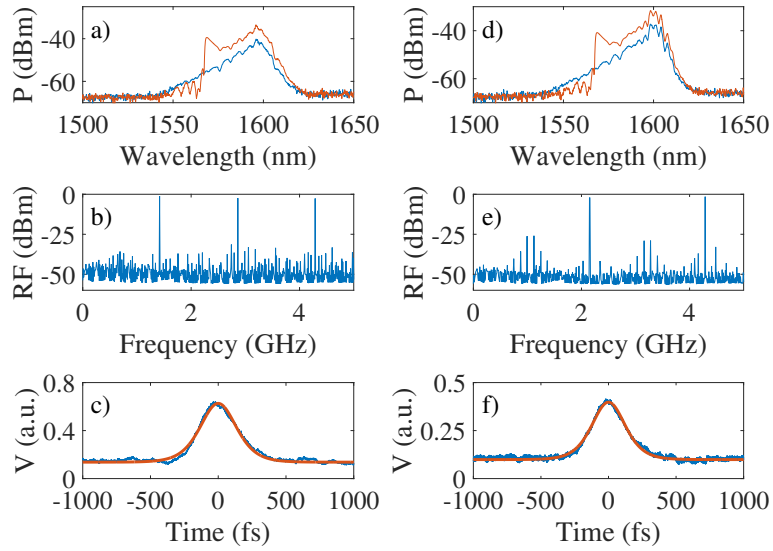


Figure 4.6: a) Optical spectra of the pulses before (blue) and after (brown) amplification by the L-band fiber amplifier. b) RF spectrum and c) intensity autocorrelation trace (blue) and  $\text{sech}^2$  fit (brown) of the amplified pulses for a SOA bias current  $I = 204$  mA. d)-f) Same magnitudes for a SOA bias current  $I = 300.2$  mA. In all these measurements, the SOA temperature is  $T = 40^\circ\text{C}$ .

The optical spectrum of the pulses after passage through the L-band fiber amplifier is also shown (brown curve in a), and it can be seen that—in spite of the appearance of a shoulder arising from amplified spontaneous emission in the L-band amplifier—more than 95% of the input pulse energy is linearly amplified. In these conditions, the autocorrelation trace of the amplified pulses displays a clear peak with a FWHM of 382 fs. After fitting to hyperbolic secant pulses (see brown line), the FWHM pulse width then corresponds to 247 fs, and the resulting time–bandwidth product is 0.31, quite close to the expected theoretical limit. At still higher currents [see Figs. 4.6(d)–4.6(f)], the pulse width remains the same, although the repetition rate of the pulse train has increased up to 2.1 GHz and there is some degree of amplitude modulation. The variations in pulse amplitude are on the order of 10% on the oscilloscope screen, but they cannot be assessed from the autocorrelation traces because the pulse period ( $\simeq 480$  ps) is almost twice the maximum delay available in our autocorrelator.

In order to clarify the physical origin of these ML dynamics, a PM optical isolator

was inserted between the 50:50 coupler and the SOA. It was observed that ML appeared only when the isolator was set such that light traveled from the coupler toward the SOA. In this configuration, the light entering the SOA through the rear facet is strongly amplified and partially fed back onto the opposing facet of the SOA after reaching the fiber-loop mirror. If the direction of the optical isolator is reversed, the amplified light cannot be fed back onto the SOA, which experiences only feedback due to the weak spontaneous emission in the counterpropagating direction. In our opinion, the physical mechanism underlying pulse formation in this system is the interaction between the counterpropagating pulses that is at work in colliding-pulse mode-locked lasers (see e.g., [103]), which is based on the ultrafast dynamics of the gain in active semiconductor systems as described in [269]. This same mechanism is, in our opinion, the one that leads to active ML by counterpropagating injection of external pulses, as, for example, in [146, 147, 270, 271].

#### **4.4 Conclusions**

We have experimentally studied the ML dynamics of a F8L which has a strongly dichroic SOA as gain medium in a simple cavity composed of off-the-shelf PM components. The simplicity of the device, whose only active element is the SOA and which does not require any polarization controller, makes it very attractive for several applications. Increasing the bias current in the SOA leads to self-starting ML at the fundamental repetition rate of 18 MHz just after crossing the lasing threshold, and further increasing the bias current into the SOA leads to the progressive emission of additional optical pulses in each round trip and eventually to mode-locked emission at increasingly high harmonics of the fundamental repetition rate, up to 2.45 GHz. The intensity autocorrelation of the amplified mode-locked pulses has an FWHM duration of 382 fs, which corresponds to a pulse duration of 247 fs. The physical mechanism leading to ML seems to be the interaction of the counterpropagating waves in the SOA, and work is in progress to better substantiate this hypothesis.

## Chapter 5

# Optical addressing of pulses in a SOA-based Figure-of-Eight fiber laser

The following chapter describes the experimental achievement of the independent recording and erasure of the LS and highly stable ultrashort pulses generated by an all-PM SOA based fiber laser in a F8L configuration. The chapter consists in the literal transcription of the article “Optical Addressing of Pulses in a Semiconductor-Based Figure-of-Eight Fiber Laser”. Reprinted (abstract/excerpt/figure) with permission from **Daniel Chaparro** and Salvador Balle, Physical Review Letters, Volume 120, Page Number 064101, 2018. Copyright 2018 by the American Physical Society (<http://dx.doi.org/10.1103/PhysRevLett.120.064101>).

**Abstract:** We experimentally demonstrate that optical pulses emitted by a semiconductor-based polarization-maintaining figure-of-eight fiber laser are temporal localized structures that can be individually switched on and off by means of optical reinjection of single pulses at different delay times. We also explore the formation of an equispaced cluster of localized structures that can be interpreted as a portion of an underlying periodic pattern—the harmonic state—and we provide a basic theoretical scenario for explaining the observations.

### 5.1 Introduction

Localized Structures (LSs) are states characterized by a correlation range much shorter than the characteristic size of the system, appearing in many nonlinear dissipative systems [272]. The concept of LSs originated in the field of pattern formation for describing the inhomogeneous spatial distribution of some order parameter, and it represents one of the paradigms of self-organization. Spatial LSs arise in systems like granular media [273], gas discharges [274], semiconductor devices [275], reaction-diffusion systems [276], fluids [277], convective systems [278], optical cavities [193, 279], etc. LSs may arise when different states coexist—the most common case being that of

the coexistence of a homogeneous and a modulated state whose period is much shorter than the size of the system, hereby ensuring a large enough aspect ratio—although more complex scenarios can be found; see Refs. [179, 280] for a review. In the most common scenario, LSs are interpreted as the elementary constituents of the modulated state. Their coexistence with a homogeneous state makes LSs individually addressable objects which can be created or destroyed independently without disturbing the rest of the system; hence, they can be used as bits for information processing and storage. While the precise theoretical definition of LSs is still under debate [281], an operational definition based on their addressability is usually adopted [138, 169, 253].

Recently, the concept of LSs has been extended to the time domain [282–285], particularly for optical resonators [171]. Temporal LS (TLSs) appear as short optical pulses, although we should remark that not all pulse-emitting devices produce TLS since these pulses may be highly correlated in time—this the case for most mode-locked lasers [281]. TLS are observed, e.g., in injected fiber resonators [282], passively mode-locked lasers [138, 169, 253, 256], and single mode vertical-cavity surface-emitting lasers (VCSELs) [209]. In optical systems, TLSs allow us to achieve extremely high peak irradiances that enable the exploration of extreme non-linear optical effects in matter. Several interesting regimes (e.g., soliton bound states [286], molecules [287], repulsive or attracting forces on an extremely long scale [288], soliton rain [226] and soliton explosion [289]) have been experimentally observed.

TLSs may yield short optical pulses with arbitrary pulse arrangements useful in such fields as telecommunications, metrology, remote sensing, and material processing. For these applications, controlling the number and arrangement of the pulses is of the utmost importance. Léo *et al.* [282] demonstrated that optical injection in a passive fiber resonator can be used for defining the pulse pattern. In active systems, Refs. [253, 256] showed that TLSs emitted by a VCSEL with an intracavity saturable absorber can be written, erased and manipulated in position through control of the bias current applied to the laser, although this method is more limited in accuracy, flexibility, and speed optical injection.

In this Letter, we focus on the optical addressing of the pulses emitted by the so-called figure-of-eight lasers (F8Ls). From the application point of view, optical injection allows us to optically perturb the system at any specific times without the speed limits imposed by the electronics of the device, thereby overcoming certain limitations of [253, 256]. F8Ls involve two fiber loops, with one being unidirectional. The coupler connecting the two loops acts as a nonlinear optical switch, whose transmittivity depends on the nonlinear phaseshift acquired by the optical fields upon passing through an amplifying medium [290]. In our case, the gain medium is a fiber-coupled semiconductor optical amplifier (SOA) [144, 160, 291], and all of the fibers and components

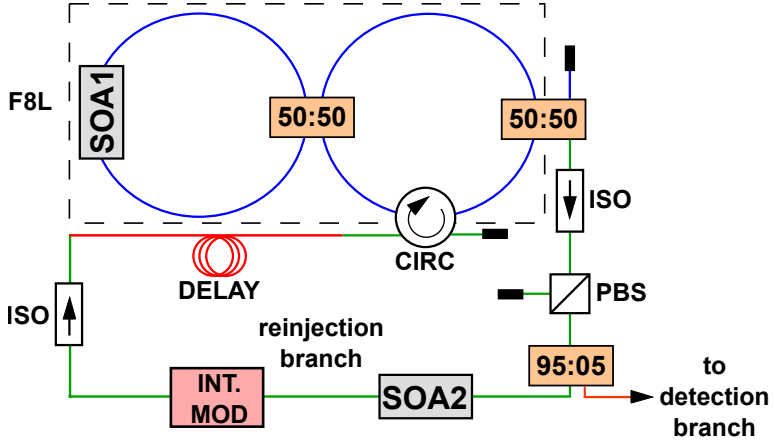


Figure 5.1: Schematics of the F8L setup. SOA: semiconductor optical amplifier. circ: circulator. ISO: optical isolator. PBS: polarization beam splitter. Int. mod: intensity modulator. See text for a detailed description.

in the F8L system are polarization maintaining (PM) to avoid nonlinear polarization evolution in the cavity due to thermal and mechanical fluctuations. This kind of F8L produced trains of optical pulses 247 fs wide at repetition frequencies ranging from 18 MHz (inverse of the round-trip time) up to a harmonic state with a repetition rate of 2.5 GHz [292]. Compared to the systems in [138, 256], the F8L is lightweight, compact, and fiber integrated—ensuring low loss, good mode quality, and mechanical stability. Here, we experimentally demonstrate that, through optical reinjection of single pulses into the original pulse train at different delay times, we are able to individually switch on additional pulses in the system without perturbing the rest of the system. We observe that there are preferred delays where the written pulses remain for a very long time after reinjection removal, and we profit from these to demonstrate that the pulses can be switched off by optical injection. Moreover, the original pulses can be extinguished by proper choice of a delay time, so the pulses from the F8L can be interpreted as TLSs within one round-trip time. Finally, we explore the formation of clusters of equally spaced LSs interpreted as portions of the periodic underlying pattern (the harmonic state), and we discuss a basic theoretical model for explaining the observations.

## 5.2 Experimental Setup

The setup of the F8L (see Fig. 5.1) is similar to that used in Ref. [292], suitably modified to allow optical injection into the cavity. The F8L is defined by two PM fiber loops coupled through a 50:50 PM fiber coupler. One loop (length  $\approx 6$  m) is purely passive, operating unidirectionally due to a PM four-port optical circulator that works in the  $1 \rightarrow 2 \rightarrow 3 \rightarrow 4 \rightarrow 1$  scheme; hence, port 4 can be used to inject optical signals into the system. The other loop (length  $\approx 5$  m) includes a single-transverse mode PM fiber-coupled SOA (SOA1, Thorlabs BOA1004P) that provides the gain. Hence, our F8L has a total transit time of  $\sim 55$  ns and works as the so-called nonlinear amplifying loop mirror. The laser output from the 50:50 coupler in the unidirectional loop passes through a PM optical isolator and is split in two with a 95:5 PM fiber coupler. The beam containing 5% of the output power is used for detection (see Ref. [292] for a description of the detection branch), while the other beam is used for optical reinjection into the F8L cavity. The reinjection beam is amplified by a second SOA (SOA2), nominally identical to SOA1. A single pulse of the laser output is selected by a PM Intensity Modulator (Photline MX-LN-10) controlled with an Electrical Pulse Generator (EPG) (Standford Research Systems Inc. DG535) triggered by the sync signal of the oscilloscope. Adjusting the delay of the EPG with respect to the sync signal from the scope allows us to pick a single optical pulse; simultaneously, the current of SOA2 is externally gated to control the power of the reinjected pulse. The length of the reinjection branch determines the time delay of the reinjected pulse with respect to the pulse train (modulo the round-trip time). It can be changed by inserting PM fiber patch cords of different lengths; in our case, the minimum delay (no patch cord inserted) is 5 ns, and each meter of patch cord adds  $\sim 5$  ns to the delay. It is also possible to write pulses “below” the default of 5 ns by using a long enough fiber cord which imposes a total delay that exceeds the round-trip.

## 5.3 Experimental results

When the reinjection loop is not active, the F8L behaves similarly to that presented in Ref. [292], although the laser threshold is now higher due to the use of a 50:50 coupler ( $I = I_{th} \simeq 135$  mA for a substrate temperature of 20° C). Close to threshold, the F8L emits light with a rather broad spectrum centered at the wavelength  $\lambda \simeq 1575$  nm. In this regime, the light-current characteristics of the F8L exhibits a slight hysteresis, and it does not switch off until the bias current is reduced below 100 mA. In the time domain, the laser output exhibits a regular train of short pulses with a period of  $\approx 55$  ns

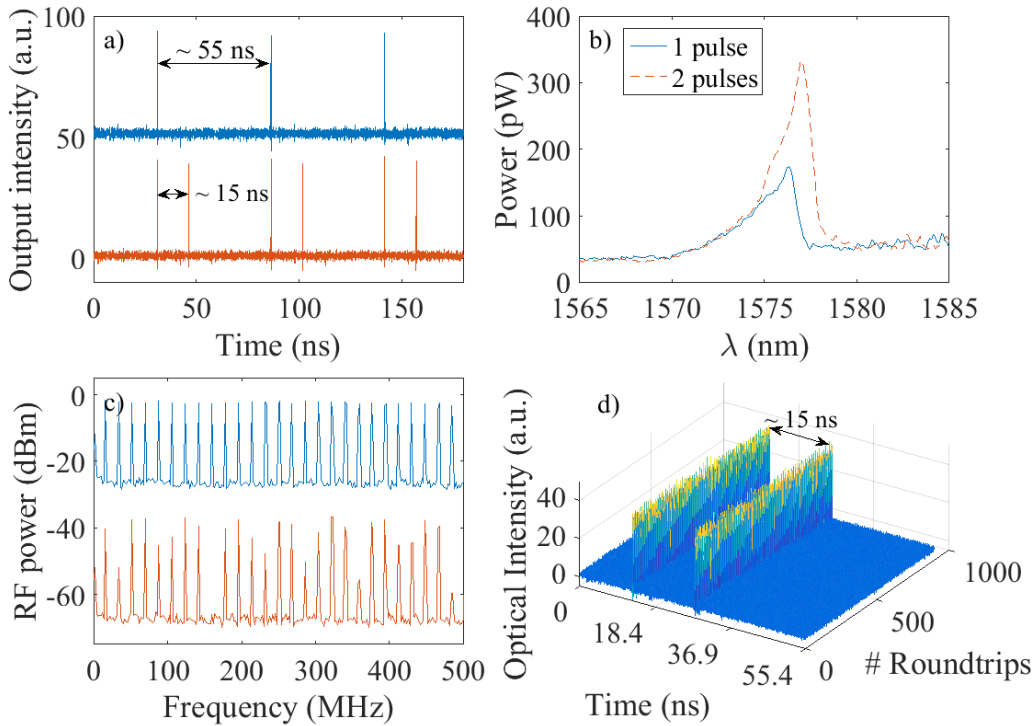


Figure 5.2: (a) (Top) Time trace (blue) showing a single pulse per round-trip with a fundamental period of 55 ns at  $I = 150$  mA (trace displaced upwards by 50 units for clarity). (Bottom) Pulse train (orange) with two pulses per round-trip (the second pulse is 15 ns from the first). (b) Optical spectrum of the traces in (a) where the solid line (blue) stays for the case of one pulse per round-trip and the dashed line (orange) for two pulses per round-trip. (c) (Top) rf spectrum of the fundamental state. (Bottom) State with two pulses per round-trip (the bottom spectrum is displaced downwards by 40 units for clarity). d) Space-time diagram showing the stability of the two-pulse state over  $\sim 1000$  round-trips.

(see the blue traces in Fig. 5.2) corresponding to the round-trip time in the fiber loops defining the F8L. The intensity autocorrelation measurement reveals that the shape of these pulses is still hyperbolic secant squared, being now much longer (1.35 ps FWHM) than those in Ref. [292] due to the substantially higher losses. The rf spectrum displays a sharp peak at the fundamental frequency of 18 MHz, and a flat comb of replicas

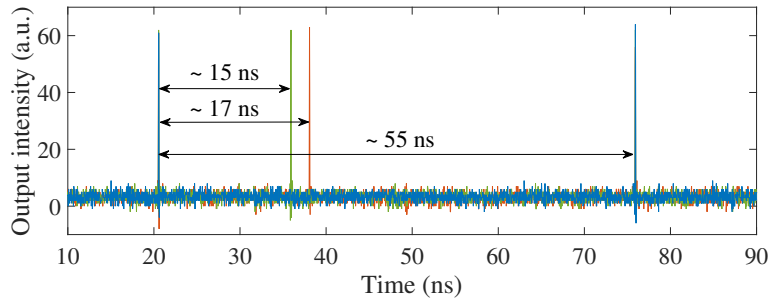


Figure 5.3: A blue time trace of the fundamental state ( $I = 150$  mA) indicating a pulsing period of 55 ns. The orange time trace was recorded after the injection of a second pulse with a delay of 17 ns (bias current in SOA2,  $I_r = 80$  mA). The green time trace was recorded after injection of a second pulse with a delay of 17 ns (bias current of SOA2,  $I_r = 0$  mA). The second pulse now appears with a delay of  $\sim 15$  ns.

of this peak within the 5 GHz bandwidth of our rf amplifier. Increasing the bias current leads to a harmonic state with a regular pulse spacing, as in Ref. [292]. In the present case, however, the transition to the harmonic state does not occur gradually through the appearance of new pulses in the pulse train; instead, it occurs suddenly due to the increased cavity losses. Yet, multiple states presenting different number of pulses within a round-trip time organized with different time arrangements can still be observed by decreasing the bias current from the harmonic state (see Fig. 5.2). These states are stable (remaining for minutes or even longer), several of them coexist for the same value of the bias current, and the observed pulse shape is the same in all of them.

The coexistence of different states of the pulse train with a constant pulse shape but different pulse number and arrangements, together with the eventual development of a harmonic state, suggests that these pulses could be TLSs [253]. To verify this hypothesis, we set the F8L in its fundamental regime and proceed to activate the reinjection loop with a patch cord of 2.4 m, imposing a delay of 17 ns. Upon gating SOA2, a new pulse appears in the pulse train, which now displays two pulses per round-trip with a pulse separation of 17 ns. This new pulse train remains stable with that pulse separation as long as the bias current of SOA2 is not completely turned off. If the bias current of SOA2 is set to 0 mA, after a few seconds the pulse moves and places itself at  $\sim 15$  ns with respect to the reference pulse (see Fig. 5.3) where it remains fixed and stable for hours. A similar situation occurs when the reinjection is performed

using a 6 meter long fiber cord in the reinjection loop corresponding to a delay of 35 ns. Again, the pulse remains in this location while SOA2 is driven by some current, but it moves—in this case to 30 ns—after SOA2’s current is turned off, remaining there for hours. These preferred pulse positions arise from the residual reflectivity of the connectors at the end of the 1.5 m long SOA pigtailed: these imperfections in the setup pin the LSs to specific positions in the round-trip, similar to what happens in broad-area VCSELs, where imperfections in the mirrors defining the cavity pinned the LSs to specific positions in the transverse plane [191].

To test the optical addressability of these pulses, a situation with the pulses remaining for very long time on their positions is required. We exploit these preferred positions by using a 2 m long fiber cord in the reinjection arm (delay  $\sim 15$  ns). By activating the reinjection arm in the fundamental state, a new pulse of the same shape is created at the corresponding delay time, remaining there indefinitely after the bias current of SOA2 is turned off (see Fig. 5.4b)). This new state with two pulses per round-trip at 15 ns is the same shown in greater detail in Fig. 5.2. In this state, by changing the delay of the EPG with respect to the sync signal in order to pick the second pulse of the pulse train, the activation of the reinjection arm leads to a state with three pulses per round-trip (Fig. 5.4c)). It is possible to switch off an existing pulse by reinjecting another optical pulse on top of (or at least very close to) it, induced by gain depletion in the semiconductor (see the Supplemental Material)(Section 5.4 of the current chapter of this thesis). If the delay between the EPG and the sync signal is now set for picking the fundamental pulse, this pulse is reinjected onto the second pulse and switched off, leading to a pulse train with two pulses per round-trip with a delay of 30 ns, as shown in Fig. 5.4d). Instead, if the delay between the EPG and the sync signal is set for picking the second pulse, this pulse is reinjected into the third pulse of the signal and switched off, hereby recovering the pulse train with two pulses per round-trip with a delay of 15 ns, as shown in Fig. 5.4e). The same process can also be performed by changing the length of the fiber patch cord instead of modifying the delay in the EPG, indicating that the interaction of the optical reinjection with the pulse train is not phase sensitive but instead mediated by the active material.

For reinjection at  $\sim 10$  ns (see Fig. 5.5), the new pulse remains in its position for shorter times (tens of seconds) after the bias current in the SOA2 is set to zero. This pulse usually jumps to the preferred position at 15 ns or—most often—moves to the proximity of the preceding pulse (at  $\sim 2$  ns), where it remains to form a bound state of two pulses (see Fig. 5.5c). Activating again the reinjection loop without modifying its settings allows us to write a new pulse in the train 10 ns from the first one. Interestingly, a short time after the SOA2 current drops to zero, the new pulse jumps to the vicinity of the bound state, placing itself at  $\sim 2$  ns from the second

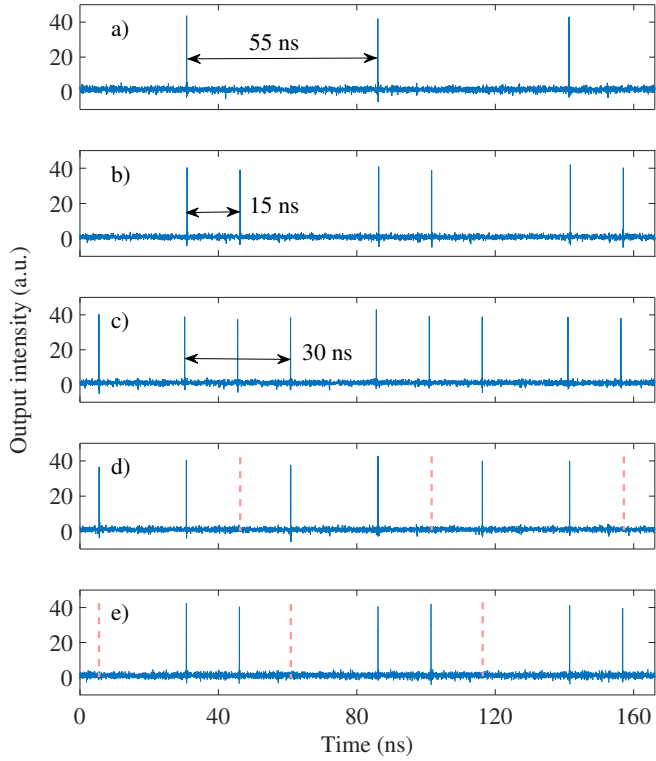


Figure 5.4: Time traces showing the optical addressing of pulses with a reinjection delay of  $\sim 15$  ns. (a) Fundamental state with pulses at  $\sim 55$  ns. (b) State with two pulses per period obtained by reinjection of a pulse. (c) State with three pulses per period obtained by reinjection of the second pulse in (b). (d) State with two pulses per period with a spacing of 30 ns obtained from (c) by reinjection of the first pulse in (c). (e) State (b) recovered from (c) by reinjection of the second pulse.

pulse in the bound state and leading to a three-pulse bound state (Fig. 5.5e). The procedure can be repeated until forming a bound state of six pulses with 2 ns pulse spacing, which we interpret as a portion of the modulated state that coexists with the homogeneous off solution [179, 280]. At this stage, the sixth pulse lays precisely 10 ns from the first pulse in the bound state (Fig. 5.5j), and activating the reinjection arm again without modifying its settings leads to switching off this sixth pulse (Fig. 5.5k). Hence, although bounded, the sixth pulse still preserves its properties as a TLS since

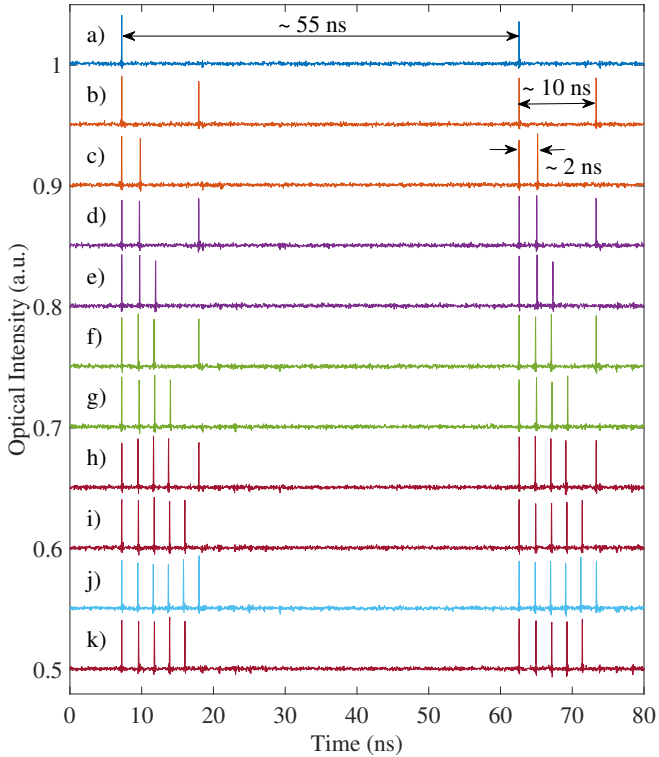


Figure 5.5: Creation of a cluster of pulses with spacing  $\sim 2$  ns. (a) Fundamental state. (b) Reinjection of the first pulse in (a) at 10 ns. (c) Displacement of the second pulse in (b) at 2 ns from the first pulse when the reinjection current is turned off. From (d)-(j), iterative procedure of the previous steps to create a six pulse cluster. (k) Erasure of the sixth pulse of the package by reinjecting on top of it. See text for explanation.

it can be switched on or off at will without affecting the rest of the bound state. The pulses in the middle of the cluster also retain their character as TLSs (see Fig. 5.6). The upper trace displays a state with a cluster of three pulses with a delay of  $\sim 15$  ns respect to the fundamental pulse, and an almost regular spacing of  $\sim 2$  ns between pulses in the cluster. In this state, reinjection of the fundamental pulse with a fiber patch cord 2.5 m long (delay,  $\sim 17.5$  ns) allows us to switch off the central pulse of the cluster (see bottom trace). As a consequence of the reduction in intracavity power, the timing of the third pulse slightly changes, passing from 20 to 19 ns.

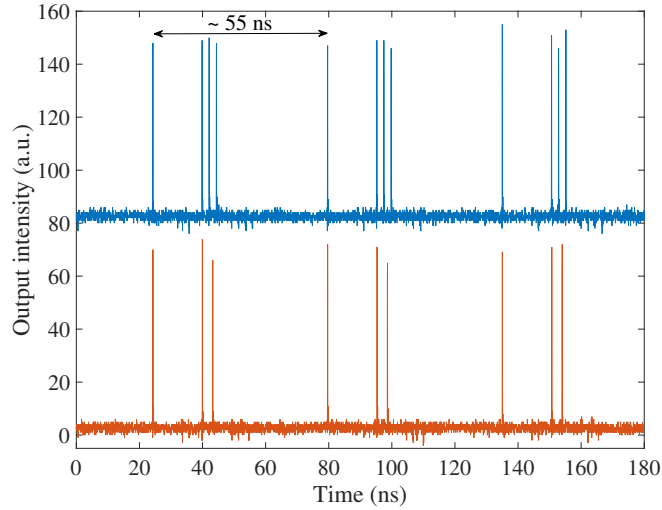


Figure 5.6: Erasure of the central pulse of a three-pulse cluster.

A basic theoretical understanding of the pulsing dynamics of a F8L can be achieved with the model presented in the Supplemental Material (Section 5.4 of the current chapter of this thesis). In the fundamental pulsing regime, the single pulse in the unidirectional loop is split in two at the 50:50 coupler. These two counterpropagating pulses arrive at different times into the SOA1, which is periodically subject to the non-simultaneous saturation imposed by these two pulses. The dynamics of the system can then be described by an iterative map, whose solution allows us to reconstruct the spatiotemporal distribution of the local gain (see the Supplemental Material)(Section 5.4 of the current chapter of this thesis).

Summarizing, we have studied the optical reinjection of pulses into a polarization-maintaining figure-of-eight laser which has a SOA as its gain medium. The coexistence of multiple lasing states from the F8L under the same parameters and the independent writing and erasing of optical pulses indicate that they can be interpreted as TLSs. These TLSs can be placed at any position within the round-trip and remain there when the bias current of the SOA2 is not zero. Turning the bias current off reveals preferred positions for the LS towards which they displace. Furthermore, interactions between LSs lead to the formation of bound states of several pulses, retaining their individuality. These features can be useful for generating periodic trains with arbitrary pulse patterns.

## 5.4 Supplemental material

A minimal theoretical model for the F8L must consider bidirectional propagation of the fields along the SOA together with the dynamics of the gain, supplemented with the boundary conditions appropriate to the F8L geometry. We adopt a simplified Traveling-Wave Model, [293, 294]

$$\left( \pm \partial_z + \frac{1}{v} \partial_t \right) A_{\pm} = \frac{1 - i\alpha}{2} g A_{\pm}, \quad (5.1)$$

$$\frac{1}{\gamma_e} \partial_t g = g_0 - g - g(|A_+|^2 + |A_-|^2), \quad (5.2)$$

where  $A_{\pm}(z, t)$  are the slowly-varying field amplitudes in the SOA at position  $z$  and time  $t$ ,  $g(z, t)$  is the instantaneous local gain due to the carrier density,  $g_0$  is the unsaturated gain due to the external pump, and  $\gamma_e$  is the gain relaxation rate due to spontaneous emission. In addition,  $v$  is the group velocity of light in the waveguide of the SOA,  $\alpha$  is the linewidth enhancement factor, internal losses are neglected in front of the large SOA gain, and gain dispersion is not considered because the typical gain bandwidth ( $\gtrsim 25$  nm) is much bigger than the typical spectral width of the laser emission even in the regime of short pulses ( $\lesssim 5$  nm).

The boundary conditions for the fields read

$$A_+(0, t) = i\sigma\rho' e^{i(\phi_1+\Phi_m)} \left[ \rho A_-(0, t - \tau_m - 2\tau_1) e^{i\phi_1} + i\sigma A_+(L, t - \tau_m - \tau_1 - \tau_2) e^{i\phi_2} \right], \quad (5.3)$$

$$A_-(L, t) = \rho\rho' e^{i(\phi_2+\Phi_m)} \left[ \rho A_-(0, t - \tau_m - \tau_1 - \tau_2) e^{i\phi_1} + i\sigma A_+(L, t - \tau_m - 2\tau_2) e^{i\phi_2} \right] = -i\frac{\rho}{\sigma} e^{i(\phi_1-\phi_2)} A_+(0, t - \tau_2 + \tau_1), \quad (5.4)$$

where  $\phi_{1,2}$  and  $\tau_{1,2}$  are the optical phase and the time delay accumulated when traveling from each facet of the SOA to the corresponding entry port of the coupler, and in our case,  $\rho = \sigma = \frac{1}{\sqrt{2}}$ . For the sake of notation, we define  $\tau_1 = \tau - \Delta/2$ ,  $\tau_2 = \tau + \Delta/2$ ,  $\phi_1 = \Phi - \phi/2$ ,  $\phi_2 = \Phi + \phi/2$ ,  $T = \tau_1 + \tau_2 + \tau_m$  and  $\Psi = \Phi_m + \phi_1 + \phi_2$ , and for definiteness we take  $\Delta \geq 0$ .

It is worth remarking that the 50:50 structure ( $\rho = \sigma = 1/\sqrt{2}$ ) as described by (5.3)-(5.4) does not define, strictly speaking, an optical resonator: if the SOA section

is replaced by a passive section ( $g \equiv 0$ ) of the same length, monochromatic solutions of the form  $A_{\pm}(z, t) = A_{\pm}e^{iq(vt \mp z)}$  cannot be found, since (5.3)-(5.4) impose  $A_{\pm} \equiv 0$ . This happens because the passive bidirectional loop is a fiber loop mirror where all the light entering through one of the input ports is reflected back through the same port; as a consequence, all the light entering the 50:50 coupler through port 4 is reflected through this very same port 4, and the unidirectionality of the other loop prevents establishing a close path for light in the device. From this point of view, the 50:50 F8L is a modeless optical device which operation relies entirely on the nonlinear effects that might impose the SOA, which should arise through the asymmetric placing of the SOA as described by  $\Delta$ .

The field equations can be formally integrated, yielding

$$A_{\pm}(z, t) = A_{\pm} \left( 0, t \mp \frac{z}{v} \right) e^{\pm \Gamma G_{\pm}(z, t)}, \quad (5.5)$$

$$G_{\pm}(z, t) = \int_0^z g \left( z', t \mp \frac{z - z'}{v} \right) dz', \quad (5.6)$$

where  $\Gamma \equiv \frac{1-i\alpha}{2}$ . Imposing the boundary conditions, one finds that

$$A_+(z, t) = A \left( t - \frac{z}{v} \right) e^{\Gamma G(z, t)}, \quad (5.7)$$

$$A_-(z, t) = -ie^{i\phi} A \left( t - \frac{L-z}{v} - \Delta \right) e^{\Gamma H(z, t)}, \quad (5.8)$$

where

$$A_+(0, t) \equiv A(t), \quad (5.9)$$

$$G(z, t) = \int_0^z g \left( z', t - \frac{z - z'}{v} \right) dz', \quad (5.10)$$

$$H(z, t) = \int_z^L g \left( z', t + \frac{z - z'}{v} \right) dz', \quad (5.11)$$

and the model can be recast as

$$\frac{1}{\gamma_e} \partial_t g = g_0 - g - g \left| A \left( t - \frac{z}{v} \right) \right|^2 e^{G(z, t)} - g \left| A \left( t - \frac{L-z}{v} - \Delta \right) \right|^2 e^{H(z, t)} \quad (5.12)$$

$$A(t) = \rho' e^{i\Psi} A \left( t - T - \frac{L}{v} \right) \times \frac{e^{\Gamma H(0, t-T+\Delta)} - e^{\Gamma G(L, t-T)}}{2}. \quad (5.13)$$

It is immediate to see that a stationary gain distribution  $g(z, t) \equiv h(z)$  implies  $A(t) \equiv 0$ .

In order to clarify the mechanism for pulsed emission in the F8L, we can try to build an approximate solution to the problem based on the experimental evidences. The system (at least in some regimes) emits a train of very short optical pulses that we approximate as a series of Dirac deltas,

$$|A(t)|^2 \simeq \sum_k P_k \delta(t - kT_p), \quad (5.14)$$

where  $T_p = T + L/v$  is the period of the pulse train. Then, eq. (5.13) imposes that

$$P_{k+1} = \left(\frac{\rho'}{2}\right)^2 P_k |e^{\Gamma H_k} - e^{\Gamma G_k}|^2, \quad (5.15)$$

where

$$G_k = \int_0^L g(z', kT_p + z'/v) dz', \quad (5.16)$$

$$H_k = \int_0^L g(z', kT_p + (L - z')/v + \Delta) dz'. \quad (5.17)$$

Using (5.14) in eq. (5.12) and integrating in time yields

$$\begin{aligned} g(z, t) &= g_0 - \gamma_e \sum_k P_k \Theta\left(t - kT_p - \frac{z}{v}\right) e^{-\gamma_e(t-kT_p-\frac{z}{v})} d_z e^{\int_0^z g(s, kT_p + \frac{s}{v}) ds} \\ &\quad + \gamma_e \sum_k P_k \Theta\left(t - kT_p - \Delta - \frac{L-z}{v}\right) \\ &\quad \times e^{-\gamma_e(t-kT_p-\Delta-\frac{L-z}{v})} d_z e^{\int_z^L g(s, kT_p + \Delta + \frac{L-s}{v}) ds}, \end{aligned} \quad (5.18)$$

where  $\Theta(x)$  is Heaviside's step function. This equation expresses that the single pulse that circulates in the unidirectional loop is split in two at the 50:50 coupler, and that these two counter-propagating pulses arrive at different times onto the active medium, which is subject to the non-simultaneous saturation imposed by these two pulses. Eq. (5.18) would determine the local gain in the device in every roundtrip if the power of each pulse,  $P_k$ , were known.

Using (5.18) in (5.16) and (5.17), one has

$$\begin{aligned} G_n &= g_0 L - \gamma_e \sum_k P_k \Theta(n-k) e^{-\gamma_e(n-k)T_p} (e^{G_k} - 1) \\ &+ \gamma_e \sum_k P_k \int_0^L \Theta \left[ (n-k)T_p - \Delta - \frac{L-2z'}{v} \right] \\ &\times e^{-\gamma_e \left[ (n-k)T_p - \Delta - \frac{L-2z'}{v} \right]} dz' e^{\int_{z'}^L g(s, kT_p + \Delta + \frac{L-s}{v}) ds} dz' , \end{aligned} \quad (5.19)$$

$$\begin{aligned} H_n &= g_0 L - \gamma_e \sum_k P_k \Theta(n-k) e^{-\gamma_e(n-k)T_p} (e^{H_k} - 1) \\ &- \gamma_e \sum_k P_k \int_0^L \Theta \left[ (n-k)T_p + \Delta + \frac{L-2z'}{v} \right] \\ &\times e^{-\gamma_e \left[ (n-k)T_p + \Delta + \frac{L-2z'}{v} \right]} dz' e^{\int_0^{z'} g(s, kT_p + \frac{s}{v}) ds} dz' , \end{aligned} \quad (5.20)$$

Recalling that, in a typical experimental situation,  $T_p \gtrsim 10$  ns,  $\gamma_e \gtrsim 10^9$  s<sup>-1</sup>,  $L \lesssim 1$  mm,  $v \sim 10^8$  m/s, one can neglect the  $z$  dependence of the exponential functions in the integrals in (5.19) and (5.20). Considering  $\Delta > L/v$ , which corresponds to a fiber length difference of 2 mm or more, one then finds a map that relates the pulse power in roundtrip  $n+1$ ,  $P_{n+1}$ , with the pulse power  $P_n$  and the gains  $G_n$  and  $H_n$  in the preceding roundtrip,

$$G_n \approx g_0 L - \gamma_e P_n \frac{e^{G_n} - 1}{2} + \mathcal{O}(e^{-\gamma_e T_p}) , \quad (5.21)$$

$$H_n \approx g_0 L - \gamma_e P_n \frac{e^{H_n} - 1}{2} - \gamma_e P_n e^{-\gamma_e \Delta} (e^{G_n} - 1) + \mathcal{O}(e^{-\gamma_e T_p}) , \quad (5.22)$$

$$\begin{aligned} P_{n+1} &= \left( \frac{\rho'}{2} \right)^2 P_n |e^{\Gamma H_n} - e^{\Gamma G_n}|^2 \\ &= \left( \frac{\rho'}{2} \right)^2 P_n \left[ e^{H_n} + e^{G_n} - 2e^{(H_n+G_n)/2} \cos \left( \alpha \frac{H_n - G_n}{2} \right) \right] . \end{aligned} \quad (5.23)$$

The fixed points of the map correspond to periodic trains of optical pulses of amplitude  $P_n = P \forall n$ , and they can be used to reconstruct the local gain (5.18) in the fundamental pulsing state.

The map also reveals that the off solution ( $P_n = 0, G_n = g_0 L = H_n \forall n$ ) is a fixed point of the system, and that (pulsing) emission occurs because of the asymmetry imposed by  $\Delta$ . However, if  $\Delta$  is too long as compared to the gain recovery time,

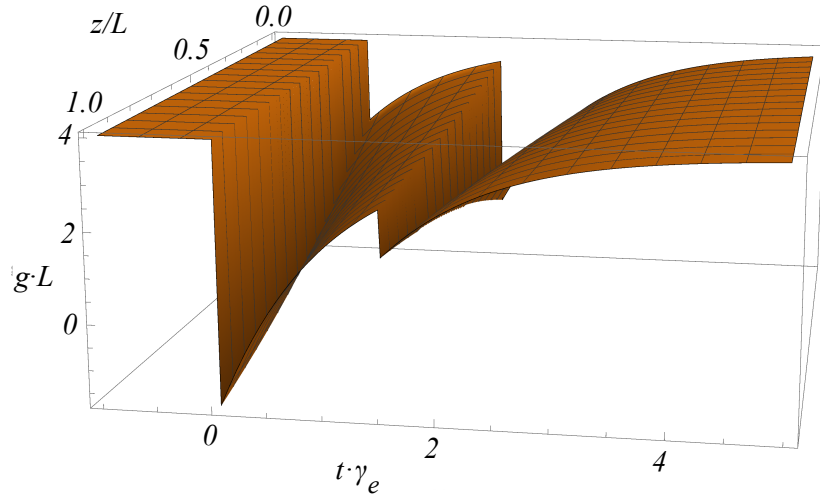


Figure 5.7: Theoretical space-time distribution of the local gain in the fundamental state for  $\alpha = 5$ ,  $L = 1$  mm,  $v = 10^8$  m/s,  $\gamma_e = 5 \cdot 10^9$  s $^{-1}$ ,  $T_p = 10$  ns,  $\Delta = 200$  ps,  $g_0 \cdot L = 5$  and  $\rho'^2 = 0.5$ .

$\gamma_E \Delta \gg 1$ , then  $G_n = H_n \Rightarrow P_n = 0$ . Indeed, when a 1 m long patch cord was inserted into the bidirectional loop, the fundamental pulsing disappeared, and only irregular harmonic dynamics could be obtained.

The dynamics of the local gain in the fundamental pulsing state is represented in Fig. 5.7 for typical parameter values for a time interval of the order of  $\gamma_e^{-1}$  after the arrival of a pulse. At a given time, the single pulse in the unidirectional loop is split in two by the 50:50 coupler. The first pulse of this pulse pair enters the SOA at  $t = 0$ ,  $z = 0$  and propagates towards  $z = L$ . As it propagates, the local gain is depleted, and the spatial hole burnt by the pulse is deeper at  $z = L$  than at  $z = 0$ . After passage of this first pulse, the local gain starts to recover due to current injection, but then, at  $t = \Delta$ , the second pulse arrives at  $z = L$ , and it propagates towards  $z = 0$  in a medium which local gain is not either homogeneous or static, thus it experiences an amplification and phase modulation that depend on the delay  $\Delta$ . Thus, in general destructive interference does not occur when the two pulses recombine at the exit of the 50:50 coupler, and sustained pulsing can exist. However, if  $\gamma_e \Delta \gg 1$ , when the second pulse arrives the medium has fully recovered from the passage of the first pulse, hence the amplification and phase modulation of the second pulse are the same as those of the first pulse; as a consequence, destructive interference among the two pulses occurs at the exit of the 50:50 coupler and the pulsing disappears. The dynamical scenario

just outlined, where the interaction between pulses is mediated by the material gain, as in [173], allows to explain the most relevant aspects of the behavior of the F8L. An additional pulse can be inserted into a given pulse train without distortion provided that the gain has recovered from the passage of the previous pulse. Hence the minimum time separation between pulses is related to the recovery time of the gain and—to a lesser extent—to the intracavity power, i.e., pulse energy. If the delay is long enough, the new pulse would induce the same dynamics described above, leading to the emission of a pulse train with two pulses per roundtrip. On the contrary, if the pulse is injected with a too short delay such that it arrives to SOA1 just before the reference pulse, it would induce a gain depletion that leads to erasing the reference pulse.

# **Chapter 6**

## **Summary and conclusions**

The present chapter aims to summarize the results and highlight the conclusions obtained throughout the work developed in this thesis which has focused on the generation of pulses in semiconductor lasers with potential applications in LiDAR systems.

In **Chapter 1**, a brief review of the state of the art of LiDAR systems has been developed with an emphasis placed on ranging methods using both CW and pulsed signals using semiconductor lasers. It has been concluded that both VCSELs and fiber laser appear as very suitable candidates to be incorporated into remote measurement techniques as they could improve the performance of LiDAR measurements due to their outstanding benefits at very low cost such as the possibility to operate at eye-safe wavelengths, the improvement of the resolution by the supply of ultra-short pulse duration, the great facility to be externally modulated and the possibility of their integration in chips than can be assembly in drone-based LiDAR stations of reduced dimensions. According to this, the center of attention throughout the work carried out in this thesis has set to the research on the generation and dynamics of the pulses emitted by two types of the most common semiconductor lasers: a VCSEL in external cavity configuration emitting at 980 nm and a fiber laser based on a SOA emitting at 1550 nm. In particular, for the last case mentioned, the demonstration of the nature of the pulses as LS points to the possibility of generate arbitrary patterns of pulses which could be used under the similar basis scheme that RM-CW LiDAR, this is to say, ranging by means of the correlation of a same pseudo random binary sequence after a delay time between the emitted and received signals, but overcoming the electrical modulation of a CW signal as the switching on or off of the pulses is already all-optically performed by the laser. However, the power emitted by the lasers studied in this thesis is not comparable to that of standard RM-CW –set in the order of the watt– and external amplification might be required. Furthermore, the devices developed here show a moderated dependency with the room temperature and consequently, a good thermal isolation system should be developed in order to implement these lasers on real LiDAR systems. On the other hand, although the F8L laser also presents the same ambient temperature dependency, it exhibits an outstanding robustness against

mechanical perturbations which, together with the possibility of integrating it on a chip, makes it appealing for many aerial LiDAR applications like those involving drones or space crafts.

In **Chapter 2**, the antecedents on previous studies which have already established the ability to generate pulses by means of cross-reinjection of polarization in a VCSEL or by passive mode-locking when including an RSAM in the cavity have been shown as well as the demonstration of the nature of these pulses as LS for sufficiently long cavities. In such a system, multiple states with a varying number of these LS are able to coexist making possible to switch them on or off, however, the methods used for such a purpose are quite rough and imprecise as they involve mechanical perturbations of the experimental setup. Hence, the contribution of the work realized in this chapter of the thesis on such a system has consisted in finding precise and effective parameters for the generation and control of the optical pulses. It has been experimentally found that the bias current of the VCSEL is a very suitable parameter for such a purpose if it is modulated by a sinusoidal signal and two requirements are fulfilled: a frequency equal to the cavity round-trip and an amplitude comprised between the off-state and the regime with the maximum number of pulses. The application of such a modulation to the VCSEL has allowed for the electrical addressing of pulses as it has been possible to generate and erase a multi-pulse pattern of 5 pulses one by one by increasing and decreasing the modulation depth at each step. These results have been theoretically supported and explained through the simulations obtained from a delayed differential equation model with delay concluding that the pulses are generated due to a temporal overrun of the modulation gain over the value in which a single independent pulse may exist forcing the pulses to be located in the regions of maximum gain and establishes the spacing between pulses. However, one of the main limitations of the setup exposed in this chapter is linked to the fact that the number of pulses within the round-trip in the previous configuration was limited by the cavity length achievable in a standard-size room laboratory prompted the adaptation of the setup to optical fiber in order to reach arbitrarily long cavities.

Hence, **Chapter 3** is devoted to the creation of an experimental setup based on an optical fiber ring using a SOA (mainly emitting in a linear  $x$ -polarization) as the gain medium which is able to overcome the limitations of the previous setup in terms of cavity lengths. Given the big broadness shown by the SOA, a band-pass filter has also been incorporated to the setup for the selection and tuning of the operation wavelength of the system. In analogy with the previous setup, the first method explored for the generation of pulses has been the passive mode-locking using a fiber-coupled RSAM. This configuration has demonstrated the capability of emitting pulses although in a quite unstable manner given the changes on the polarization state of the

---

light propagating in the optical fiber. Hence, it has been found that the management of the degree of freedom of the polarization is an indispensable requirement for the controlled generation of optical pulses and the generation of pulses by crossed polarization reinjection has been explored using different fibered and air-based polarization controllers and showing both, in general, more weaknesses than strengths. With respect to the use of fibered polarization controllers, on the contrary to what is expected according to the antecedents described in Chapter 2, no pulsed emission have been observed for the orthogonal reinjection of the linear  $x$ -polarization. However, if the polarization controller is managed to slightly increase the ellipticity of the reinjected light, the system emits pulses of 100 ps of FWHM which are separated regularly by the round-trip time of the cavity. The traces obtained in this manner remain stable for many minutes and they have allowed performing TOF measurements demonstrating, hence, the potential use of the pulses generated by this laser in LiDAR systems. However, in general for any other polarization states, this fibered polarization controllers are not deterministic and suffer from a remarkable lack of precision and repeatability what prevents to know without a doubt the polarization state of the reinjected light. Knowing this and only with exploratory purposes in order to sketch the potential of this setup, reinjections of unknown and arbitrary polarizations have been performed and plenty of different dynamical regimes have been observed like square waves, bright and dark pulses and also traces with pulses that evidence signs of being LS. Although the limitations shown by the fibered polarization controllers have been tried to be overcome by deterministic air-based polarization controllers, it has been found that the management of the polarization in the experimental system cannot be fully dominated given that the tuning of the band-pass filter present in the setup also affects the polarization. Hence, it can be concluded that the management of the polarization, although it is required for the generation of pulses under this experimental configuration, is a completely inefficient operational method to achieve the desired controlled pulsed emission given the existence of intrinsic limitations of the controllers and external factors affecting the polarization state that cause a big impact on the stability of the temporal traces, translating in any case in a lack of knowledge on the state of the reinjected polarization.

Therefore, due to the uncertainties linked to control on the reinjection of the polarization, the configuration of the ring cavity is dropped out and the fiber laser setup is redesign in **Chapter 4** as a PM F8L with a 50:50 coupler interconnecting two cavity loops: one being unidirectional containing an optical circulator and the other bidirectional containing the SOA. Although the first tests have been performed including polarization controllers and the band-pass filter in the loops of the F8L to compare its dynamical behavior with that of the previous setup, it has been rapidly found that the

generation of pulsing states occurs even with better performance without the presence of these two elements. This is an extraordinary simplification offering tremendous benefits given that the F8L contains only the SOA, a circulator and a coupler and the behavior of the system is far more robust, stable and predictable. The optical power is increased in one order of magnitude with respect to the ring configuration and different pulsed regimes appear systematically for bias currents above the threshold showing a much higher temporal stability without being affected neither by thermal nor mechanical effects, being remarkable that the optical table could be considerably hit without affecting the output traces.

Hence, the fact that the whole system is PM and the absence of polarization controllers confirms that the polarization degree of freedom does not play any role in the generation of pulses under this experimental scheme. It has also been found out that for bias currents of the SOA close to the threshold, the system is able to emit pulses in the fundamental regime with one pulse per round-trip with a repetition frequency of 18 MHz. For higher currents, the system emits in a multiplicity of harmonic states with many equispaced pulses in a round-trip (up to 2.45 GHz). Furthermore, the number of pulses can be controlled (increased or decreased) by raising or lowering the bias current of the SOA. Besides all these benefits in terms of stability of the traces and simplicity of the generation of the pulsing states, this system has also demonstrated the capability to generate ultrashort pulses in the range of the femtosecond as the autocorrelation techniques applied confirmed with a value for the FWHM of the pulses of 247 fs.

Finally, in **Chapter 5**, and given that this SOA has given hints of the emission of LS in previous configurations, a reinjection branch was built. It was gated by an optical intensity modulator and contained a replaceable patch cord whose length determines the temporal delay at which the reinjected pulse is written (with a default delay of 5 ns occurring when no patch cord is added). The opening of the gate created with the optical modulator has demonstrated the capability to reinject a pulse at any desired delay as long as the bias current of the optical intensity modulator is not set to 0 mA. When this is the case, it has been found that most of the pulses drift until they place themselves at certain preferred positions from which the pulses do not displace anymore. It was found out that 15 ns and 30 ns were two of these preferred positions within a roundtrip of 55 ns and, hence, reinjecting a pair of pulses at these two temporal locations gave rise to a trace with three pulses per round-trip which could be independently written and erased at will as many times as desired. Moreover, this F8L has also shown the capability to emit clusters states of pulses being also possible the erasure of a single of the pulses of the cluster without perturbing the others. This experimental evidences together with the observation of the coexistence of multiple

---

lasing states under the same parameters demonstrate the nature of LS of the pulses generated by the PM F8L.

Even more interestingly, it has been noticed that given that the optical circulator in the unidirectional cavity prevents the formation of a closed cavity causing the F8L to be a modeless laser and the mechanism leading to the pulsed emission cannot be either PML nor crossed polarization reinjection. Hence, this F8L cannot operate if the local gain distribution is stationary and, therefore assuming a pulsing solution, we have reformulated the Travelling-Wave equations of the system in terms of a discrete map that allows us to assess the impact of the different parameters on the pulsing dynamics of the F8L, and we have used the fixed point of the map for evidencing the dynamics of the local gain in the SOA. The pulsing dynamics of the F8L can be traced back to the asymmetry of the active loop: the difference in arrival times of the pulses to the SOA facets makes each pulse to propagate in an active medium with different pumping.

## Outlook

All the results just exposed have been obtained from the research performed throughout this thesis, however, it has also raised several subjects of future research comprising both experimental as theoretical which are listed below:

- **Creation of a fully operational arbitrary pulse pattern generator:** the features shown by the F8L designed and studied in this thesis settle the basis for the creation of an all-optical arbitrary pulse pattern generator only limited by the displacement experienced by the pulses when the reinjection branch is switched off. As described, given that the pulses show the tendency to stack together showing a minimal repetition frequency of 500 MHz, the concept of introducing a sinusoidal perturbative optical modulation in the F8L at that frequency should force the location of the pulses and avoid their displacements when varying the current of the gate. Although not shown in this thesis, some preliminary results strongly support this idea and thus further research on this topic is highly required.
- **Further development of the theoretical frame for the F8L:** the description of the theoretical behavior of the F8L designed in this thesis has demonstrated to be extremely challenging given the lack of an evident mechanism causing the generation of pulses given that neither saturable absorbent effects nor polarization evolution nor even cavity modes were present in the F8L. Although the preliminary model developed in this thesis offers a satisfactory description

of the behavior of the F8L for the evolution of the gain and lasing parameters, further efforts in the highly demanding task of solving of the integro-differential equations with delays present in the model are required for the simulation of the temporal traces.

- **Study of the range of asymmetry allowed by the F8L:** according to the nominal length of the optical fibers, the experimental setup has been built with the SOA located symmetrically with respect the coupler in the bidirectional. However, the difference between the nominal and real value introduces a small asymmetry that induces the pulsed emission justified by the model and numerical simulations. Hence, it is required to explore the impact of such a parameter on the emission of the F8L. Some preliminary tests have been accomplished by introducing a fibered variable delay line confirming the absence of pulses for a perfectly symmetrical F8L although further research is needed.
- **Implementation in a LiDAR system:** although the proof-of-principles of TOF measurements in fiber were satisfactorily accomplished, more in-depth measurements of LiDAR ensuring the effectiveness of the measurements not only in optical fiber but also in air, shall be performed. Thus, the creation of a fully operational setup that accurately collimates the output beam, directs it to a target and detects the back reflection can be considered to be developed for future work.
- **Comparison with a full PM ring fiber laser with RSAM:** given the good results offered by the SOA under a PM F8L configuration, a highly interesting way to come full circle would be to recover the fiber ring cavity configuration with RSAM but adapting it by using a PM fiber-coupled RSAM and filter to study the behavior of such a system in comparison with the previous VCSEL–RSAM setup that originated the work accomplished in this thesis.

## Bibliography

- [1] A. Kilpelä, “Pulsed time-of-flight laser range finder techniques for fast, high precision measurement applications,” PhD thesis, University of Oulu, 2004. [Online]. Available: <http://urn.fi/urn:isbn:9514272625>.
- [2] T. H. Maiman, “Stimulated optical radiation in ruby,” *Nature*, vol. 187, no. 4736, p. 493, 1960. DOI: [10.1038/187493a0](https://doi.org/10.1038/187493a0).
- [3] L. D. Smullin and G. Fiocco, “Optical echoes from the Moon,” *Nature*, vol. 194, no. 4835, p. 1267, 1962. DOI: [10.1038/1941267a0](https://doi.org/10.1038/1941267a0).
- [4] G. Fiocco and L. D. Smullin, “Detection of scattering layers in the upper atmosphere (60–140 km) by optical radar,” *Nature*, vol. 199, no. 4900, p. 1275, 1963. DOI: [10.1038/1991275a0](https://doi.org/10.1038/1991275a0).
- [5] G. G. Goyer and R. Watson, “The laser and its application to meteorology,” *Bulletin of the American Meteorological Society*, vol. 44, no. 9, p. 564, 1963, ISSN: 00030007, 15200477. [Online]. Available: <http://www.jstor.org/stable/26247220>.
- [6] E. O. Hulbert, “Observations of a searchlight beam to an altitude of 28 kilometers,” *Journal of the Optical Society of America*, vol. 27, no. 11, p. 377, 1937. DOI: [10.1364/josa.27.000377](https://doi.org/10.1364/josa.27.000377).
- [7] E. A. Johnson, R. C. Meyer, R. E. Hopkins, and W. H. Mock, “The measurement of light scattered by the upper atmosphere from a search-light beam,” *Journal of the Optical Society of America*, vol. 29, no. 12, p. 512, 1939. DOI: [10.1364/josa.29.000512](https://doi.org/10.1364/josa.29.000512).
- [8] L. Elterman, “The measurement of stratospheric density distribution with the searchlight technique,” *Journal of Geophysical Research*, vol. 56, no. 4, p. 509, 1951. DOI: [10.1029/jz056i004p00509](https://doi.org/10.1029/jz056i004p00509).
- [9] ——, “Seasonal trends of temperature, density, and pressure to 67.6 km obtained with the searchlight probing technique,” *Journal of Geophysical Research*, vol. 59, no. 3, p. 351, 1954. DOI: [10.1029/jz059i003p00351](https://doi.org/10.1029/jz059i003p00351).
- [10] R. T. H. Collis, “Lidar,” in *Advances in Geophysics*, vol. 13, Elsevier, 1969, p. 113. DOI: [10.1016/s0065-2687\(08\)60509-9](https://doi.org/10.1016/s0065-2687(08)60509-9).

## Bibliography

---

- [11] R. M. Measures, *Laser remote sensing: Fundamentals and applications*. New York: Wiley-Interscience, 1984, Provided by the SAO/NASA Astrophysics Data System. [Online]. Available: <https://ui.adsabs.harvard.edu/abs/1984wi..book....M>.
- [12] B. Lohani and S. Ghosh, “Airborne LiDAR technology: A review of data collection and processing systems,” *Proceedings of the National Academy of Sciences, India Section A: Physical Sciences*, vol. 87, no. 4, p. 567, 2017. DOI: 10.1007/s40010-017-0435-9.
- [13] J. G. Williams, S. G. Turyshev, and D. H. Boggs, “Progress in lunar laser ranging tests of relativistic gravity,” *Physical Review Letters*, vol. 93, no. 26, p. 261101, 2004. DOI: 10.1103/physrevlett.93.261101.
- [14] I. Ciufolini, E. C. Pavlis, J. Ries, R. Koenig, G. Sindoni, A. Paolozzi, and H. Newmayer, “Gravitomagnetism and its measurement with laser ranging to the LAGEOS satellites and GRACE earth gravity models,” in *General Relativity and John Archibald Wheeler*, I. Ciufolini and R. A. Matzner, Eds. Dordrecht: Springer Netherlands, 2010, p. 371. DOI: 10.1007/978-90-481-3735-0\_17.
- [15] T. W. Murphy, “Lunar laser ranging: The millimeter challenge,” *Reports on Progress in Physics*, vol. 76, no. 7, p. 076901, 2013. DOI: 10.1088/0034-4885/76/7/076901.
- [16] J. Bösenberg and V. Matthias, “EARLINET: A european aerosol research lidar network to establish an aerosol climatology,” Max-Planck-Institut für Meteorologie, Tech. Rep., 2003. [Online]. Available: <http://hdl.handle.net/2117/12900>.
- [17] I. Veselovskii, A. Kolgotin, V. Griaznov, D. Müller, K. Franke, and D. N. Whiteman, “Inversion of multiwavelength Raman lidar data for retrieval of bimodal aerosol size distribution,” *Applied Optics*, vol. 43, no. 5, p. 1180, 2004. DOI: 10.1364/ao.43.001180.
- [18] A. Behrendt, T. Nakamura, and T. Tsuda, “Combined temperature lidar for measurements in the troposphere, stratosphere, and mesosphere,” *Applied Optics*, vol. 43, no. 14, p. 2930, 2004. DOI: 10.1364/ao.43.002930.
- [19] F. Mao, W. Gong, S. Song, and Z. Zhu, “Determination of the boundary layer top from lidar backscatter profiles using a Haar wavelet method over Wuhan, China,” *Optics & Laser Technology*, vol. 49, p. 343, 2013. DOI: 10.1016/j.optlastec.2012.08.017.

- 
- [20] M. Hayman, S. Spuler, and B. Morley, “Polarization lidar observations of backscatter phase matrices from oriented ice crystals and rain,” *Optics Express*, vol. 22, no. 14, p. 16976, 2014. DOI: [10.1364/oe.22.016976](https://doi.org/10.1364/oe.22.016976).
  - [21] M. Kempenaars, J. C. Flanagan, L. Giudicotti, M. J. Walsh, M. Beurskens, I. Balboa, and J.-E. Contributors, “Enhancement of the JET edge LIDAR Thomson scattering diagnostic with ultrafast detectors,” *Review of Scientific Instruments*, vol. 79, no. 10, p. 10E728, 2008. DOI: [10.1063/1.2969078](https://doi.org/10.1063/1.2969078).
  - [22] P. Newman, G. Sibley, M. Smith, M. Cummins, A. Harrison, C. Mei, I. Posner, R. Shade, D. Schroeter, L. Murphy, W. Churchill, D. Cole, and I. Reid, “Navigating, recognizing and describing urban spaces with vision and lasers,” *The International Journal of Robotics Research*, vol. 28, no. 11-12, p. 1406, 2009. DOI: [10.1177/0278364909341483](https://doi.org/10.1177/0278364909341483).
  - [23] C. Rasmussen, K. Sohn, Q. Wang, and P. Oh, “Perception and control strategies for driving utility vehicles with a humanoid robot,” in *2014 IEEE/RSJ International Conference on Intelligent Robots and Systems*, 2014, p. 973. DOI: [10.1109/iros.2014.6942677](https://doi.org/10.1109/iros.2014.6942677).
  - [24] H. Jeong, J. Oh, M. Kim, K. Joo, I. S. Kweon, and J. H. Oh, “Control strategies for a humanoid robot to drive and then egress a utility vehicle for remote approach,” in *2015 IEEE-RAS 15th International Conference on Humanoid Robots (Humanoids)*, 2015, p. 811. DOI: [10.1109/HUMANOIDS.2015.7363447](https://doi.org/10.1109/HUMANOIDS.2015.7363447).
  - [25] S. Verghese, “Self-driving cars and lidar,” in *Conference on Lasers and Electro-Optics*, 2017, p. AM3A.1. DOI: [10.1364/CLEO\\_AT.2017.AM3A.1](https://doi.org/10.1364/CLEO_AT.2017.AM3A.1).
  - [26] R. W. Wolcott and R. M. Eustice, “Robust LIDAR localization using multiresolution Gaussian mixture maps for autonomous driving,” *The International Journal of Robotics Research*, vol. 36, no. 3, p. 292, 2017. DOI: [10.1177/0278364917696568](https://doi.org/10.1177/0278364917696568).
  - [27] K. T. Vierling, L. A. Vierling, W. A. Gould, S. Martinuzzi, and R. M. Clawges, “Lidar: Shedding new light on habitat characterization and modeling,” *Frontiers in Ecology and the Environment*, vol. 6, no. 2, p. 90, 2008. DOI: [10.1890/070001](https://doi.org/10.1890/070001).
  - [28] K. T. Vierling, C. Bässler, R. Brandl, L. A. Vierling, I. Weiß, and J. Müller, “Spinning a laser web: predicting spider distributions using LiDAR,” *Ecological Applications*, vol. 21, no. 2, p. 577, 2011. DOI: [10.1890/09-2155.1](https://doi.org/10.1890/09-2155.1).

## Bibliography

---

- [29] M. Colgan, C. Baldeck, J. Féret, and G. Asner, “Mapping savanna tree species at ecosystem scales using support vector machine classification and BRDF correction on airborne hyperspectral and LiDAR data,” *Remote Sensing*, vol. 4, no. 11, p. 3462, 2012. DOI: [10.3390/rs4113462](https://doi.org/10.3390/rs4113462).
- [30] W. D. Simonson, H. D. Allen, and D. A. Coomes, “Use of an airborne lidar system to model plant species composition and diversity of mediterranean oak forests,” *Conservation Biology*, vol. 26, no. 5, p. 840, 2012. DOI: [10.1111/j.1523-1739.2012.01869.x](https://doi.org/10.1111/j.1523-1739.2012.01869.x).
- [31] N. C. Coops, F. Morsdorf, M. E. Schaepman, and N. E. Zimmermann, “Characterization of an alpine tree line using airborne LiDAR data and physiological modeling,” *Global Change Biology*, vol. 19, no. 12, p. 3808, 2013. DOI: [10.1111/gcb.12319](https://doi.org/10.1111/gcb.12319).
- [32] M. E. H. Burton, J. R. Poulsen, M. E. Lee, V. P. Medjibe, C. G. Stewart, A. Venkataraman, and L. J. T. White, “Reducing carbon emissions from forest conversion for oil palm agriculture in Gabon,” *Conservation Letters*, vol. 10, no. 3, p. 297, 2016. DOI: [10.1111/conl.12265](https://doi.org/10.1111/conl.12265).
- [33] G. P. Asner, P. G. Brodrick, C. Philipson., N. R. Vaughn, R. E. Martin, D. E. Knapp, J. Heckler, L. J. Evans, T. Jucker, B. Goossens, D. J. Stark, G. Reynolds, R. Ong, N. Renneboog, F. Kugan, and D. A. Coomes, “Mapped aboveground carbon stocks to advance forest conservation and recovery in Malaysian Borneo,” *Biological Conservation*, vol. 217, p. 289, 2018. DOI: [10.1016/j.biocon.2017.10.020](https://doi.org/10.1016/j.biocon.2017.10.020).
- [34] V. González-Jaramillo, A. Fries, J. Zeilinger, J. Homeier, J. Paladines-Benitez, and J. Bendix, “Estimation of above ground biomass in a tropical mountain forest in southern ecuador using airborne LiDAR data,” *Remote Sensing*, vol. 10, no. 5, p. 660, 2018. DOI: [10.3390/rs10050660](https://doi.org/10.3390/rs10050660).
- [35] B. D. Collins and N. Sitar, “Stability of steep slopes in cemented sands,” *Journal of Geotechnical and Geoenvironmental Engineering*, vol. 137, no. 1, p. 43, 2011. DOI: [10.1061/\(asce\)gt.1943-5606.0000396](https://doi.org/10.1061/(asce)gt.1943-5606.0000396).
- [36] C. M. Litton, C. P. Giardina, J. K. Albano, M. S. Long, and G. P. Asner, “The magnitude and variability of soil-surface CO<sub>2</sub> efflux increase with mean annual temperature in Hawaiian tropical montane wet forests,” *Soil Biology and Biochemistry*, vol. 43, no. 11, p. 2315, 2011. DOI: [10.1016/j.soilbio.2011.08.004](https://doi.org/10.1016/j.soilbio.2011.08.004).

- 
- [37] J. N. Otoo, N. H. Maerz, X. Li, and Y. Duan, “Verification of a 3-D LiDAR viewer for discontinuity orientations,” *Rock Mechanics and Rock Engineering*, vol. 46, no. 3, p. 543, 2013. DOI: [10.1007/s00603-012-0366-3](https://doi.org/10.1007/s00603-012-0366-3).
  - [38] A. Mushkin, A. Sagy, E. Trabelci, R. Amit, and N. Porat, “Measuring the time and scale-dependency of subaerial rock weathering rates over geologic time scales with ground-based lidar,” *Geology*, vol. 42, no. 12, p. 1063, 2014. DOI: [10.1130/g35866.1](https://doi.org/10.1130/g35866.1).
  - [39] E. Nadal-Romero, J. Revuelto, P. Errea, and J. I. López-Moreno, “The application of terrestrial laser scanner and SfM photogrammetry in measuring erosion and deposition processes in two opposite slopes in a humid badlands area (central Spanish Pyrenees),” *SOIL*, vol. 1, no. 2, p. 561, 2015. DOI: [10.5194/soil-1-561-2015](https://doi.org/10.5194/soil-1-561-2015).
  - [40] J. A. Richardson, C. B. Connor, P. H. Wetmore, L. J. Connor, and E. A. Gallant, “Role of sills in the development of volcanic fields: Insights from lidar mapping surveys of the San Rafael Swell, Utah,” *Geology*, vol. 43, no. 11, p. 1023, 2015. DOI: [10.1130/g37094.1](https://doi.org/10.1130/g37094.1).
  - [41] M. Chevalier, J. Pan, H. Li, Z. Sun, D. Liu, J. Pei, W. Xu, and C. Wu, “First tectonic-geomorphology study along the Longmu–Gozha Co fault system, Western Tibet,” *Gondwana Research*, vol. 41, p. 411, 2017. DOI: [10.1016/j.gr.2015.03.008](https://doi.org/10.1016/j.gr.2015.03.008).
  - [42] A. Jochem, B. Höfle, and M. Rutzinger, “Extraction of vertical walls from mobile laser scanning data for solar potential assessment,” *Remote Sensing*, vol. 3, no. 4, p. 650, 2011. DOI: [10.3390/rs3030650](https://doi.org/10.3390/rs3030650).
  - [43] H. T. Nguyen, J. M. Pearce, R. Harrap, and G. Barber, “The application of LiDAR to assessment of rooftop solar photovoltaic deployment potential in a municipal district unit,” *Sensors*, vol. 12, no. 4, p. 4534, 2012. DOI: [10.3390/s120404534](https://doi.org/10.3390/s120404534).
  - [44] N. Lukač, D. Žlaus, S. Seme, B. Žalik, and G. Štumberger, “Rating of roofs’ surfaces regarding their solar potential and suitability for PV systems, based on LiDAR data,” *Applied Energy*, vol. 102, p. 803, 2013, Special Issue on Advances in sustainable biofuel production and use - XIX International Symposium on Alcohol Fuels - ISAF. DOI: [10.1016/j.apenergy.2012.08.042](https://doi.org/10.1016/j.apenergy.2012.08.042).
  - [45] T. Le, D. Khaldi, H. Xie, B. Dong, and R. Vega, “LiDAR-based solar mapping for distributed solar plant design and grid integration in San Antonio, Texas,” *Remote Sensing*, vol. 8, no. 3, p. 247, 2016. DOI: [10.3390/rs8030247](https://doi.org/10.3390/rs8030247).

## Bibliography

---

- [46] R. Margolis, P. Gagnon, J. Melius, C. Phillips, and R. Elmore, “Using GIS-based methods and lidar data to estimate rooftop solar technical potential in US cities,” *Environmental Research Letters*, vol. 12, no. 7, p. 074013, 2017. DOI: [10.1088/1748-9326/aa7225](https://doi.org/10.1088/1748-9326/aa7225).
- [47] N. Salimzadeh and A. Hammad, “High-level framework for GIS-based optimization of building photovoltaic potential at urban scale using BIM and LiDAR,” in *International Conference on Sustainable Infrastructure 2017*, 2017, p. 123. DOI: [10.1061/9780784481196.012](https://doi.org/10.1061/9780784481196.012).
- [48] S. El-Asha, L. Zhan, and G. V. Iungo, “Quantification of power losses due to wind turbine wake interactions through SCADA, meteorological and wind LiDAR data,” *Wind Energy*, vol. 20, no. 11, p. 1823, 2017. DOI: [10.1002/we.2123](https://doi.org/10.1002/we.2123).
- [49] F. Carbajo Fuertes and F. Porté-Agel, “Using a virtual lidar approach to assess the accuracy of the volumetric reconstruction of a wind turbine wake,” *Remote Sensing*, vol. 10, no. 5, p. 721, 2018. DOI: [10.3390/rs10050721](https://doi.org/10.3390/rs10050721).
- [50] F. Carbajo Fuertes, C. Markfort, and F. Porté-Agel, “Wind turbine wake characterization with nacelle-mounted wind lidars for analytical wake model validation,” *Remote Sensing*, vol. 10, no. 5, p. 668, 2018. DOI: [10.3390/rs10050668](https://doi.org/10.3390/rs10050668).
- [51] V. Ussyshkin and L. Theriault, “Airborne lidar: Advances in discrete return technology for 3D vegetation mapping,” *Remote Sensing*, vol. 3, no. 3, p. 416, 2011. DOI: [10.3390/rs3030416](https://doi.org/10.3390/rs3030416).
- [52] L. Wallace, A. Lucieer, C. Watson, and D. Turner, “Development of a UAV-LiDAR system with application to forest inventory,” *Remote Sensing*, vol. 4, no. 6, p. 1519, 2012. DOI: [10.3390/rs4061519](https://doi.org/10.3390/rs4061519).
- [53] A. Lausch, S. Erasmi, D. King, P. Magdon, and M. Heurich, “Understanding forest health with remote sensing—part II—A review of approaches and data models,” *Remote Sensing*, vol. 9, no. 2, p. 129, 2017. DOI: [10.3390/rs9020129](https://doi.org/10.3390/rs9020129).
- [54] A. Kelly, N. Chan, H. Herman, D. Huber, R. Meyers, P. Rander, R. Warner, J. Ziglar, and E. Capstick, “Real-time photorealistic virtualized reality interface for remote mobile robot control,” *The International Journal of Robotics Research*, vol. 30, no. 3, p. 384, 2010. DOI: [10.1177/0278364910383724](https://doi.org/10.1177/0278364910383724).
- [55] A. M. Pinto, L. F. Rocha, and A. P. Moreira, “Object recognition using laser range finder and machine learning techniques,” *Robotics and Computer Integrated Manufacturing*, vol. 29, no. 1, p. 12, 2013. DOI: [10.1016/j.rcim.2012.06.002](https://doi.org/10.1016/j.rcim.2012.06.002).

- 
- [56] H. Alismail and B. Browning, "Automatic calibration of spinning actuated lidar internal parameters," *Journal of Field Robotics*, vol. 32, no. 5, p. 723, 2014. DOI: 10.1002/rob.21543.
  - [57] K. M. Johnson and W. B. Ouimet, "Rediscovering the lost archaeological landscape of southern New England using airborne light detection and ranging (LiDAR)," *Journal of Archaeological Science*, vol. 43, p. 9, 2014. DOI: 10.1016/j.jas.2013.12.004.
  - [58] M. D. McCoy and T. N. Ladefoged, "New developments in the use of spatial technology in archaeology," *Journal of Archaeological Research*, vol. 17, no. 3, p. 263, 2009. DOI: 10.1007/s10814-009-9030-1.
  - [59] K. M. Prufer, A. E. Thompson, and D. J. Kennett, "Evaluating airborne LiDAR for detecting settlements and modified landscapes in disturbed tropical environments at Uxbenká, Belize," *Journal of Archaeological Science*, vol. 57, p. 1, 2015. DOI: 10.1016/j.jas.2015.02.013.
  - [60] D. Tapete, V. Banks, L. Jones, M. Kirkham, and D. Garton, "Contextualising archaeological models with geological, airborne and terrestrial LiDAR data: The Ice Age landscape in Farndon Fields, Nottinghamshire, UK," *Journal of Archaeological Science*, vol. 81, p. 31, 2017. DOI: 10.1016/j.jas.2017.03.007.
  - [61] A. P. Shetty, "GPS-LiDAR sensor fusion aided by 3D city models for UAVs," Master's thesis, University of Illinois at Urbana-Champaign, 2017. [Online]. Available: <http://hdl.handle.net/2142/97501>.
  - [62] M. Uijt de Haag, "An integrated LIDAR/IMU/GPS navigation and surveillance," Ohio University, Tech. Rep., Dec. 2004, p. 16. [Online]. Available: <https://www.researchgate.net/publication/235012220>.
  - [63] K. Gajdamowicz, D. Öhman, and M. Horemuz, "Mapping and 3D modelling of urban environment based on lidar, gps/imu and image data," in *Proceeding of 5th International Symposium on Mobile Mapping Technology*, 2007. [Online]. Available: <https://www.isprs.org/proceedings/XXXVI/5-C55/>.
  - [64] A. Soloviev, "Tight coupling of GPS, laser scanner, and inertial measurements for navigation in urban environments," in *2008 IEEE/ION Position, Location and Navigation Symposium*, 2008, p. 511. DOI: 10.1109/PLANS.2008.4570059.
  - [65] T. Bosch and M. Lescure, *Selected papers on laser distance measurements*, ser. SPIE milestone series. SPIE Optical Engineering Press, 1995, ISBN: 9780819420107. [Online]. Available: <http://spie.org/Publications/Book/602487?SSO=1>.

## Bibliography

---

- [66] M. Amann, T. M. Bosch, M. Lescure, R. A. Myllylae, and M. Rioux, “Laser ranging: A critical review of usual techniques for distance measurement,” *Optical Engineering*, vol. 40, no. 1, p. 10, 2001. DOI: [10.1117/1.1330700](https://doi.org/10.1117/1.1330700).
- [67] S. Donati, *Electro-Optical Instrumentation: Sensing and Measuring with Lasers*. Upper Saddle River, NJ, USA: Prentice Hall PTR, 2004, ISBN: 0130616109.
- [68] N. Takeuchi, N. Sugimoto, H. Baba, and K. Sakurai, “Random modulation cw lidar,” *Applied Optics*, vol. 22, no. 9, p. 1382, 1983. DOI: [10.1364/ao.22.001382](https://doi.org/10.1364/ao.22.001382).
- [69] N. J. Krichel, A. McCarthy, and G. S. Buller, “Resolving range ambiguity in a photon counting depth imager operating at kilometer distances,” *Optics Express*, vol. 18, no. 9, p. 9192, 2010. DOI: [10.1364/oe.18.009192](https://doi.org/10.1364/oe.18.009192).
- [70] M. Quatrevallet, X. Ai, A. Pérez-Serrano, P. Adamiec, J. Barbero, A. Fix, G. Ehret, J. G. Rarity, and I. Esquivias, “Random-modulation differential absorption lidar based on semiconductor lasers and single photon counting for atmospheric CO<sub>2</sub> sensing,” in *International Conference on Space Optics — ICSO 2016*, vol. 10562, 2017. DOI: [10.1117/12.2296151](https://doi.org/10.1117/12.2296151).
- [71] X. Ai, R. Nock, J. G. Rarity, and N. Dahnoun, “High-resolution random-modulation cw lidar,” *Applied Optics*, vol. 50, no. 22, p. 4478, 2011. DOI: [10.1364/ao.50.004478](https://doi.org/10.1364/ao.50.004478).
- [72] F. Y. Lin and J. M. Liu, “Chaotic lidar,” *IEEE Journal of Selected Topics in Quantum Electronics*, vol. 10, no. 5, p. 991, 2004. DOI: [10.1109/jstqe.2004.835296](https://doi.org/10.1109/jstqe.2004.835296).
- [73] Y. Wang and A. Wang, “A novel high-resolution chaotic lidar with optical injection to chaotic laser diode,” in *Semiconductor Lasers and Applications III*, 2008. DOI: [10.1117/12.757320](https://doi.org/10.1117/12.757320).
- [74] R. Agishev, B. Gross, F. Moshary, S. Ahmed, and A. Gilerson, “Development of a SNR parameterization scheme for general lidar assessment,” *Applied Physics B*, vol. 80, no. 6, p. 765, 2005. DOI: [10.1007/s00340-005-1783-8](https://doi.org/10.1007/s00340-005-1783-8).
- [75] R. Agishev, B. Gross, F. Moshary, A. Gilerson, and S. Ahmed, “Range-resolved pulsed and CWFM lidars: Potential capabilities comparison,” *Applied Physics B*, vol. 85, no. 1, p. 149, 2006. DOI: [10.1007/s00340-006-2254-6](https://doi.org/10.1007/s00340-006-2254-6).
- [76] M. U. Piracha, D. Nguyen, D. Mandridis, T. Yilmaz, I. Ozdur, S. Ozharar, and P. J. Delfyett, “Range resolved lidar for long distance ranging with sub-millimeter resolution,” *Optics Express*, vol. 18, no. 7, p. 7184, 2010. DOI: [10.1364/oe.18.007184](https://doi.org/10.1364/oe.18.007184).

- 
- [77] O. Uchino, M. Tokunaga, M. Maeda, and Y. Miyazoe, “Differential-absorption-lidar measurement of tropospheric ozone with excimer–raman hybrid laser,” *Optics Letters*, vol. 8, no. 7, p. 347, 1983. DOI: [10.1364/ol.8.000347](https://doi.org/10.1364/ol.8.000347).
- [78] S. E. Bisson, “Parametric study of an excimer-pumped, nitrogen Raman shifter for lidar applications,” *Applied Optics*, vol. 34, no. 18, p. 3406, 1995. DOI: [10.1364/ao.34.003406](https://doi.org/10.1364/ao.34.003406).
- [79] L. Herbst, R. F. Delmdahl, and R. Paetzl, “Average power scaling of UV excimer lasers drives flat panel display and lidar applications,” in *High Energy/Average Power Lasers and Intense Beam Applications VI; Atmospheric and Oceanic Propagation of Electromagnetic Waves VI*, 2012. DOI: [10.1117/12.906687](https://doi.org/10.1117/12.906687).
- [80] T. J. Kane, B. Zhou, and R. L. Byer, “Potential for coherent Doppler wind velocity lidar using neodymium lasers,” *Applied Optics*, vol. 23, no. 15, p. 2477, 1984. DOI: [10.1364/ao.23.002477](https://doi.org/10.1364/ao.23.002477).
- [81] R. W. Farley and P. D. Dao, “Development of an intracavity-summed multiple-wavelength Nd:YAG laser for a rugged, solid-state sodium lidar system,” *Applied Optics*, vol. 34, no. 21, p. 4269, 1995. DOI: [10.1364/ao.34.004269](https://doi.org/10.1364/ao.34.004269).
- [82] P. Rambaldi, M. Douard, and J. P. Wolf, “New UV tunable solid-state lasers for lidar applications,” *Applied Physics B Laser and Optics*, vol. 61, no. 1, p. 117, 1995. DOI: [10.1007/bf01090981](https://doi.org/10.1007/bf01090981).
- [83] K. Scholle, E. Heumann, and G. Huber, “Single mode Tm and Tm,Ho:LuAG lasers for LIDAR applications,” *Laser Physics Letters*, vol. 1, no. 6, p. 285, 2004. DOI: [10.1002/lapl.200410067](https://doi.org/10.1002/lapl.200410067).
- [84] Y. Xia, X. Cheng, F. Li, J. Wang, Y. Yang, X. Lin, and S. Gong, “Long-term wavelength drift compensation of tunable pulsed dye laser for sodium detection lidar,” *Optics Communications*, vol. 354, p. 52, 2015. DOI: [10.1016/j.optcom.2015.05.048](https://doi.org/10.1016/j.optcom.2015.05.048).
- [85] J. Jiao, G. Yang, J. Wang, X. Cheng, L. Du, Z. Wang, and W. Gong, “Initial multi-parameter detection of atmospheric metal layers by Beijing Na–K lidar,” *Journal of Quantitative Spectroscopy and Radiative Transfer*, vol. 188, p. 46, 2016. DOI: [10.1016/j.jqsrt.2016.05.018](https://doi.org/10.1016/j.jqsrt.2016.05.018).
- [86] Y. Chen, Q. Liu, S. Hu, and J. Huang, “SO<sub>2</sub> differential absorption lidar system based on dye laser,” in *AOPC 2017: Optical Sensing and Imaging Technology and Applications*, 2017. DOI: [10.1117/12.2285262](https://doi.org/10.1117/12.2285262).

## Bibliography

---

- [87] E. C. Burrows and K. Y. Liou, "High resolution laser LIDAR utilising two-section distributed feedback semiconductor laser as a coherent source," *Electronics Letters*, vol. 26, no. 9, p. 577, 1990. DOI: [10.1049/el:19900378](https://doi.org/10.1049/el:19900378).
- [88] B. Schwarz, "Mapping the world in 3D," *Nature Photonics*, vol. 4, no. 7, p. 429, 2010. DOI: [10.1038/nphoton.2010.148](https://doi.org/10.1038/nphoton.2010.148).
- [89] P. J. Rodrigo and C. Pedersen, "Field performance of an all-semiconductor laser coherent Doppler lidar," *Optics Letters*, vol. 37, no. 12, p. 2277, 2012. DOI: [10.1364/ol.37.002277](https://doi.org/10.1364/ol.37.002277).
- [90] P. J. Rodrigo, Q. Hu, and C. Pedersen, "Semiconductor laser lidar wind velocity sensor for turbine control," in *Light, Energy and the Environment*, 2014, p. EF3A.3. DOI: [10.1364/E2.2014.EF3A.3](https://doi.org/10.1364/E2.2014.EF3A.3).
- [91] I. Esquivias, A. Consoli, M. Krakowski, M. Faugeron, G. Kochem, M. Traub, J. Barbero, P. Fiadino, X. Ai, J. Rarity, M. Quatrevalet, and G. Ehret, "High-brightness all semiconductor laser at 1.57  $\mu\text{m}$  for space-borne lidar measurements of atmospheric carbon dioxide: Device design and analysis of requirements," in *Laser Sources and Applications II*, vol. 9135, 2014. DOI: [10.1117/12.2052191](https://doi.org/10.1117/12.2052191).
- [92] Q. Hu, C. Pedersen, and P. J. Rodrigo, "Eye-safe diode laser Doppler lidar with a MEMS beam-scanner," *Optics Express*, vol. 24, no. 3, p. 1934, 2016. DOI: [10.1364/oe.24.001934](https://doi.org/10.1364/oe.24.001934).
- [93] M. Hayman and S. Spuler, "Demonstration of a diode-laser-based high spectral resolution lidar (HSRL) for quantitative profiling of clouds and aerosols," *Optics Express*, vol. 25, no. 24, p. A1096, 2017. DOI: [10.1364/oe.25.0a1096](https://doi.org/10.1364/oe.25.0a1096).
- [94] R. Matthey and V. Mitev, "Pseudo-random noise-continuous-wave laser radar for surface and cloud measurements," *Optics and Lasers in Engineering*, vol. 43, no. 3-5, p. 557, 2005. DOI: [10.1016/j.optlaseng.2004.03.014](https://doi.org/10.1016/j.optlaseng.2004.03.014).
- [95] K. Myneni, T. A. Barr, B. R. Reed, S. D. Pethel, and N. J. Corron, "High-precision ranging using a chaotic laser pulse train," *Applied Physics Letters*, vol. 78, no. 11, p. 1496, 2001. DOI: [10.1063/1.1355663](https://doi.org/10.1063/1.1355663).
- [96] W. Wu, Y. Liao, and F. Lin, "Noise suppressions in synchronized chaos lidars," *Optics Express*, vol. 18, no. 25, p. 26155, 2010. DOI: [10.1364/oe.18.026155](https://doi.org/10.1364/oe.18.026155).
- [97] Y. Hong, P. S. Spencer, and K. A. Shore, "Enhancement of chaotic signal bandwidth in vertical-cavity surface-emitting lasers with optical injection," *Journal of the Optical Society of America B*, vol. 29, no. 3, p. 415, 2012. DOI: [10.1364/josab.29.000415](https://doi.org/10.1364/josab.29.000415).

- 
- [98] K. Iiyama, S. Matsui, T. Kobayashi, and T. Maruyama, “High-resolution FMCW reflectometry using a single-mode vertical-cavity surface-emitting laser,” *IEEE Photonics Technology Letters*, vol. 23, no. 11, p. 703, 2011. DOI: 10.1109/lpt.2011.2131124.
- [99] A. E. Siegman, *Lasers*. Mill Valley, Calif: University Science Books, 1986, ISBN: 0935702113.
- [100] N. Postec and P. Picart, *Optique pour l'ingénieur*, Website, 2009. [Online]. Available: [http://www.optique-ingenieur.org/fr/cours/OPI\\_fr\\_M01\\_C01/co/Contenu\\_13.html](http://www.optique-ingenieur.org/fr/cours/OPI_fr_M01_C01/co/Contenu_13.html).
- [101] E. A. Avrutin, E. L. Portnoi, and J. H. Marsh, “Monolithic and multi-GigaHertz mode-locked semiconductor lasers: Constructions, experiments, models and applications,” *IEE Proceedings - Optoelectronics*, vol. 147, no. 4, p. 251, 2000. DOI: 10.1049/ip-opt:20000282.
- [102] V. S. Letokhov and V. N. Morozov, “Generation of ultra-short duration coherent light pulses,” *Soviet Journal of Experimental and Theoretical Physics*, vol. 25, p. 862, 1967, Provided by the SAO/NASA Astrophysics Data System. [Online]. Available: <http://adsabs.harvard.edu/abs/1967JETP...25..862L>.
- [103] S. Bischoff, M. P. Sørensen, J. Mørk, S. D. Brorson, T. Franck, J. M. Nielsen, and A. Møller-Larsen, “Pulse-shaping mechanism in colliding-pulse mode-locked laser diodes,” *Applied Physics Letters*, vol. 67, no. 26, p. 3877, 1995. DOI: 10.1063/1.115303.
- [104] K. Merghem, A. Akroud, A. Martinez, G. Moreau, J.-P. Tourrenc, F. Lelarge, F. V. Dijk, G.-H. Duan, G. Aubin, and A. Ramdane, “Short pulse generation using a passively mode locked single InGaAsP/InP quantum well laser,” *Optics Express*, vol. 16, no. 14, p. 10 675, 2008. DOI: 10.1364/oe.16.010675.
- [105] M. J. R. Heck, E. J. Salumbides, A. Renault, E. A. J. M. Bente, Y. Oei, M. K. Smit, R. van Veldhoven, R. Nötzel, K. S. E. Eikema, and W. Ubachs, “Analysis of hybrid mode-locking of two-section quantum dot lasers operating at 15 μm,” *Optics Express*, vol. 17, no. 20, p. 18 063, 2009. DOI: 10.1364/oe.17.018063.
- [106] T. Brabec, C. Spielmann, P. F. Curley, and F. Krausz, “Kerr lens mode locking,” *Optics Letters*, vol. 17, no. 18, p. 1292, 1992. DOI: 10.1364/ol.17.001292.

## Bibliography

---

- [107] V. J. Matsas, T. P. Newson, D. J. Richardson, and D. N. Payne, “Selfstarting passively mode-locked fibre ring soliton laser exploiting nonlinear polarisation rotation,” *Electronics Letters*, vol. 28, no. 15, p. 1391, 1992. DOI: [10.1049/el:19920885](https://doi.org/10.1049/el:19920885).
- [108] M. J. Heck, M. L. Davenport, H. Park, D. J. Blumenthal, and J. E. Bowers, “Ultra-long cavity hybrid silicon mode-locked laser diode operating at 930 MHz,” in *Optical Fiber Communication Conference*, 2010, p. OM15. DOI: [10.1364/OFC.2010.OMI5](https://doi.org/10.1364/OFC.2010.OMI5).
- [109] S. Cheung, J. Baek, R. P. Scott, N. K. Fontaine, F. M. Soares, X. Zhou, D. M. Baney, and S. J. B. Yoo, “1-GHz monolithically integrated hybrid mode-locked InP laser,” *IEEE Photonics Technology Letters*, vol. 22, no. 24, p. 1793, 2010. DOI: [10.1109/lpt.2010.2086050](https://doi.org/10.1109/lpt.2010.2086050).
- [110] Y. Chen and M. C. Wu, “Monolithic colliding-pulse mode-locked quantum-well lasers,” *IEEE Journal of Quantum Electronics*, vol. 28, no. 10, p. 2176, 1992. DOI: [10.1109/3.159526](https://doi.org/10.1109/3.159526).
- [111] M. Xia, M. G. Thompson, R. V. Penty, and I. H. White, “External-cavity mode-locked quantum-dot laser diodes for low repetition rate, sub-picosecond pulse generation,” *IEEE Journal of Selected Topics in Quantum Electronics*, vol. 17, no. 5, p. 1264, 2011. DOI: [10.1109/jstqe.2011.2159828](https://doi.org/10.1109/jstqe.2011.2159828).
- [112] G. New, “Pulse evolution in mode-locked quasi-continuous lasers,” *IEEE Journal of Quantum Electronics*, vol. 10, no. 2, p. 115, 1974. DOI: [10.1109/jqe.1974.1145781](https://doi.org/10.1109/jqe.1974.1145781).
- [113] C. W. Wilmsen, H. Temkin, and L. A. Coldren, *Vertical-Cavity Surface-Emitting Lasers*. Cambridge, UK: Cambridge University Press, 1999, ISBN: 0521590221.
- [114] K. Iga, “Surface-emitting laser-its birth and generation of new optoelectronics field,” *IEEE Journal of Selected Topics in Quantum Electronics*, vol. 6, no. 6, p. 1201, 2000. DOI: [10.1109/2944.902168](https://doi.org/10.1109/2944.902168).
- [115] H. Li, P. Wolf, P. Moser, G. Larisch, J. A. Lott, and D. Bimberg, “Vertical-cavity surface-emitting lasers for optical interconnects,” *SPIE Newsroom*, 2014. DOI: [10.1117/2.1201411.005689](https://doi.org/10.1117/2.1201411.005689).
- [116] J. S. Harris, H. Bae, and T. Sarmiento, “GaInNAs(Sb) long-wavelength VC-SELs,” in *VCSELS: Fundamentals, Technology and Applications of Vertical-Cavity Surface-Emitting Lasers*, R. Michalzick, Ed. Berlin, Heidelberg: Springer Berlin Heidelberg, 2013, p. 353. DOI: [10.1007/978-3-642-24986-0\\_11](https://doi.org/10.1007/978-3-642-24986-0_11).

- 
- [117] J. J. Kim, K. H. Kim, M. Lee, H. S. Lee, E. Lee, O. Kwon, J. Roh, and B. Yoo, “2.5-Gb/s hybrid single-mode and multimode fiber transmission of 1.5- $\mu$ m wavelength VCSEL,” *IEEE Photonics Technology Letters*, vol. 19, no. 5, p. 297, 2007. DOI: 10.1109/lpt.2007.891243.
- [118] A. Larsson, “Advances in VCSELs for communication and sensing,” *IEEE Journal of Selected Topics in Quantum Electronics*, vol. 17, no. 6, p. 1552, 2011. DOI: 10.1109/jstqe.2011.2119469.
- [119] W. Hofmann, M. Müller, P. Wolf, A. Mutig, T. Gründl, G. Böhm, D. Bimberg, and M. C. Amann, “40 Gbit/s modulation of 1550 nm VCSEL,” *Electronics Letters*, vol. 47, no. 4, p. 270, 2011. DOI: 10.1049/el.2010.3631.
- [120] C. Xie, P. Dong, S. Randel, D. Pilori, P. Winzer, S. Spiga, B. Kögel, C. Neumeyr, and M.-C. Amann, “Single-VCSEL 100-Gb/s short-reach system using discrete multi-tone modulation and direct detection,” in *Optical Fiber Communication Conference*, 2015, p. Tu2H.2. DOI: 10.1364/OFC.2015.Tu2H.2.
- [121] G. Giuliani, M. Norgia, S. Donati, and T. Bosch, “Laser diode self-mixing technique for sensing applications,” *Journal of Optics A: Pure and Applied Optics*, vol. 4, no. 6, p. S283, 2002. DOI: 10.1088/1464-4258/4/6/371.
- [122] R. S. Matharu, J. Perchoux, R. Kliese, Y. L. Lim, and A. D. Rakić, “Maintaining maximum signal-to-noise ratio in uncooled vertical-cavity surface-emitting laser-based self-mixing sensors,” *Optics Letters*, vol. 36, no. 18, p. 3690, 2011. DOI: 10.1364/ol.36.003690.
- [123] S. Ura, S. Shoda, K. Nishio, and Y. Awatsuji, “In-line rotation sensor based on VCSEL behavior under polarization-rotating optical feedback,” *Optics Express*, vol. 19, no. 24, p. 23 683, 2011. DOI: 10.1364/oe.19.023683.
- [124] X. Zhao, E. K. Lau, D. Parekh, H.-K. Sung, W. Hofmann, M. C. Amann, M. C. Wu, and C. J. Chang-Hasnain, “107-GHz resonance frequency of 1.55- $\mu$ m VCSELs under ultra-high optical injection locking,” in *Conference on Lasers and Electro-Optics/Quantum Electronics and Laser Science Conference and Photonic Applications Systems Technologies*, 2008, p. CMW4. [Online]. Available: <http://www.osapublishing.org/abstract.cfm?URI=CLEO-2008-CMW4>.
- [125] R. Diaz, S. Chan, and J. Liu, “Lidar detection using a dual-frequency source,” *Optics Letters*, vol. 31, no. 24, p. 3600, 2006. DOI: 10.1364/ol.31.003600.

## Bibliography

---

- [126] A. Hurtado, A. Quirce, A. Valle, L. Pesquera, and M. J. Adams, “Nonlinear dynamics induced by parallel and orthogonal optical injection in 1550 nm Vertical-Cavity Surface-Emitting Lasers (VCSELs),” *Optics Express*, vol. 18, no. 9, p. 9423, 2010. DOI: [10.1364/oe.18.009423](https://doi.org/10.1364/oe.18.009423).
- [127] A. Quirce, A. Valle, H. Lin, Y. Zhang, and D. W. Pierce, “Polarization switching of transverse modes in VCSELs subject to two-frequency orthogonal optical injection,” in *Semiconductor Lasers and Laser Dynamics V*, vol. 8432, 2012. DOI: [10.1117/12.922524](https://doi.org/10.1117/12.922524).
- [128] H. Lin, D. W. Pierce, A. J. Basnet, A. Quirce, Y. Zhang, and A. Valle, “Two-frequency injection on a multimode vertical-cavity surface-emitting laser,” *Optics Express*, vol. 19, no. 23, p. 22437, 2011. DOI: [10.1364/oe.19.022437](https://doi.org/10.1364/oe.19.022437).
- [129] S. Chan, S. Hwang, and J. Liu, “Period-one oscillation for photonic microwave transmission using an optically injected semiconductor laser,” *Optics Express*, vol. 15, no. 22, p. 14921, 2007. DOI: [10.1364/oe.15.014921](https://doi.org/10.1364/oe.15.014921).
- [130] S.-C. Chan, S.-K. Hwang, and J.-M. Liu, “Radio-over-fiber transmission from an optically injected semiconductor laser in period-one state,” in *Physics and Simulation of Optoelectronic Devices XV*, vol. 6468, 2007. DOI: [10.1117/12.699170](https://doi.org/10.1117/12.699170).
- [131] R. Gordon, A. P. Heberle, and J. R. A. Cleaver, “Transverse mode-locking in microcavity lasers,” *Applied Physics Letters*, vol. 81, no. 24, p. 4523, 2002. DOI: [10.1063/1.1528287](https://doi.org/10.1063/1.1528287).
- [132] B. Zhang, D. W. Snoke, and A. P. Heberle, “Towards the transverse mode-locking of oxide-confined VCSELs,” *Optics Communications*, vol. 285, no. 20, p. 4117, 2012. DOI: [10.1016/j.optcom.2012.06.042](https://doi.org/10.1016/j.optcom.2012.06.042).
- [133] R. Haring, M. Paschotta, A. Aschwanden, E. Gini, F. Morier-Genoud, and U. Keller, “High-power passively mode-locked semiconductor lasers,” *IEEE Journal of Quantum Electronics*, vol. 38, no. 9, p. 1268, 2002. DOI: [10.1109/jqe.2002.802111](https://doi.org/10.1109/jqe.2002.802111).
- [134] K. Jasim, Q. Zhang, A. V. Nurmikko, E. Ippen, A. Mooradian, G. Carey, and W. Ha, “Picosecond pulse generation from passively modelocked vertical cavity diode laser at up to 15 GHz pulse repetition rate,” *Electronics Letters*, vol. 40, no. 1, p. 34, 2004. DOI: [10.1049/el:20040024](https://doi.org/10.1049/el:20040024).

- 
- [135] U. Keller, K. J. Weingarten, F. X. Kartner, D. Kopf, B. Braun, I. D. Jung, R. Fluck, C. Honninger, N. Matuschek, and J. A. der Au, “Semiconductor saturable absorber mirrors (SESAM’s) for femtosecond to nanosecond pulse generation in solid-state lasers,” *IEEE Journal of Selected Topics in Quantum Electronics*, vol. 2, no. 3, p. 435, 1996. DOI: 10.1109/2944.571743.
- [136] J. Javaloyes, J. Mulet, and S. Balle, “Passive mode locking of lasers by crossed-polarization gain modulation,” *Phys. Rev. Lett.*, vol. 97, no. 16, p. 163902, 2006. DOI: 10.1103/physrevlett.97.163902.
- [137] J. Mulet, J. Javaloyes, and S. Balle, “Mode-locking of VECSELs by crossed-polarization gain modulation,” *IEEE Journal of Quantum Electronics*, vol. 43, no. 9, p. 786, 2007. DOI: 10.1109/JQE.2007.902784.
- [138] M. Marconi, J. Javaloyes, S. Balle, and M. Giudici, “How lasing localized structures evolve out of passive mode locking,” *Physical Review Letters*, vol. 112, no. 22, p. 223901, 2014. DOI: 10.1103/physrevlett.112.223901.
- [139] M. E. Fermann, A. Galvanauskas, and G. Sucha, *Ultrafast Lasers: Technology and Applications*, ser. Optical Engineering - Marcel Dekker. CRC Press, 2002, ISBN: 9780203910207. [Online]. Available: <https://books.google.es/books?id=TV1fIv5xwVAC>.
- [140] C. Jauregui, J. Limpert, and A. Tünnermann, “High-power fibre lasers,” *Nature Photonics*, vol. 7, no. 11, p. 861, 2013. DOI: 10.1038/nphoton.2013.273.
- [141] M. J. Guy, J. R. Taylor, D. G. Moodie, and A. E. Kelly, “10 GHz 3 ps actively mode-locked ring laser incorporating a semiconductor laser amplifier and an electroabsorption modulator,” *Electronics Letters*, vol. 32, no. 24, p. 2240, 1996. DOI: 10.1049/el:19961482.
- [142] C. O’Riordan and M. J. Connelly, “Repetition rate and wavelength tunable all-optically mode-locked fiber ring laser based on a reflective semiconductor optical amplifier,” in *2010 7th International Symposium on Communication Systems, Networks Digital Signal Processing (CSNDSP 2010)*, 2010, p. 670. [Online]. Available: <https://ieeexplore.ieee.org/document/5580335>.
- [143] H. Shi, G. A. Alphonse, J. C. Connolly, and P. J. Delfyett, “20 × 5 Gbit/s optical WDM transmitter using single-stripe multiwavelength modelocked semiconductor laser,” *Electronics Letters*, vol. 34, no. 2, p. 179, 1998. DOI: 10.1049/el:19980155.

## Bibliography

---

- [144] K. Vlachos, C. Bintjas, N. Pleros, and H. Avramopoulos, “Ultrafast semiconductor based fiber laser sources,” *IEEE Journal of Selected Topics in Quantum Electronics*, vol. 10, no. 1, p. 147, 2004. DOI: [10.1109/JSTQE.2003.822941](https://doi.org/10.1109/JSTQE.2003.822941).
- [145] L. Xu, B. C. Wang, V. Baby, I. Glesk, and P. R. Prucnal, “Widely tunable fiber ring laser with edfa/soa,” in *LEOS 2001. 14th Annual Meeting of the IEEE Lasers and Electro-Optics Society (Cat. No.01CH37242)*, vol. 2, 2001, p. 421. DOI: [10.1109/LEOS.2001.968852](https://doi.org/10.1109/LEOS.2001.968852).
- [146] G. Lin, I. Chiu, and M. Wu, “1.2-ps mode-locked semiconductor optical amplifier fiber laser pulses generated by 60-ps backward dark-optical comb injection and soliton compression,” *Optics Express*, vol. 13, no. 3, p. 1008, 2005. DOI: [10.1364/opex.13.001008](https://doi.org/10.1364/opex.13.001008).
- [147] G. Lin, Y. Lin, K. Lin, W. Lee, and C. Wu, “50 fs soliton compression of optical clock pulse recovered from NRZ data injected SOAFL,” *Optics Express*, vol. 18, no. 9, p. 9525, 2010. DOI: [10.1364/oe.18.009525](https://doi.org/10.1364/oe.18.009525).
- [148] X. Yang, Z. Li, E. Tangdiongga, D. Lenstra, G. D. Khoe, and H. J. S. Dorren, “Sub-picosecond pulse generation employing an SOA-based nonlinear polarization switch in a ring cavity,” *Optics Express*, vol. 12, no. 11, p. 2448, 2004. DOI: [10.1364/opex.12.002448](https://doi.org/10.1364/opex.12.002448).
- [149] Y. Mao, X. Tong, Z. Wang, L. Zhan, P. Hu, and Q. Guo, “Dark and bright pulses in a SOA-based fiber ring laser,” *Optics Communications*, vol. 360, p. 35, 2016. DOI: [10.1016/j.optcom.2015.10.021](https://doi.org/10.1016/j.optcom.2015.10.021).
- [150] N. J. Doran and D. Wood, “Nonlinear-optical loop mirror,” *Optics Letters*, vol. 13, no. 1, p. 56, 1988. DOI: [10.1364/ol.13.000056](https://doi.org/10.1364/ol.13.000056).
- [151] I. N. Duling, C. J. Chen, P. K. A. Wai, and C. R. Menyuk, “Operation of a nonlinear loop mirror in a laser cavity,” *IEEE Journal of Quantum Electronics*, vol. 30, no. 1, p. 194, 1994. DOI: [10.1109/3.272080](https://doi.org/10.1109/3.272080).
- [152] R. Paschotta, *Encyclopedia of Laser Physics and Technology*. Wiley VCH Verlag GmbH, 2008, ISBN: 3527408283.
- [153] D. J. Richardson, R. I. Laming, D. N. Payne, V. Matsas, and M. W. Phillips, “Selfstarting, passively modelocked erbium fibre ring laser based on the amplifying Sagnac switch,” *Electronics Letters*, vol. 27, no. 6, p. 542, 1991. DOI: [10.1049/el:19910341](https://doi.org/10.1049/el:19910341).
- [154] I. N. Duling, “Subpicosecond all-fibre erbium laser,” *Electronics Letters*, vol. 27, no. 6, p. 544, 1991. DOI: [10.1049/el:19910342](https://doi.org/10.1049/el:19910342).

- 
- [155] S. Wang, Q. Ning, A. Luo, Z. Lin, Z. Luo, and W. Xu, "Dissipative soliton resonance in a passively mode-locked figure-eight fiber laser," *Optics Express*, vol. 21, no. 2, p. 2402, 2013. DOI: [10.1364/oe.21.002402](https://doi.org/10.1364/oe.21.002402).
  - [156] H. Lin, C. Guo, S. Ruan, and J. Yang, "Dissipative soliton resonance in an all-normal-dispersion Yb-doped figure-eight fibre laser with tunable output," *Laser Physics Letters*, vol. 11, no. 8, p. 085102, 2014. DOI: [10.1088/1612-2011/11/8/085102](https://doi.org/10.1088/1612-2011/11/8/085102).
  - [157] H. Santiago-Hernandez, O. Pottiez, M. Duran-Sanchez, R. I. Alvarez-Tamayo, J. P. Lauterio-Cruz, J. C. Hernandez-Garcia, B. Ibarra-Escamilla, and E. A. Kuzin, "Dynamics of noise-like pulsing at sub-ns scale in a passively mode-locked fiber laser," *Optics Express*, vol. 23, no. 15, p. 18840, 2015. DOI: [10.1364/oe.23.018840](https://doi.org/10.1364/oe.23.018840).
  - [158] F. B. Braham, G. Semaan, F. Bahloul, M. Salhi, and F. Sanchez, "Experimental optimization of dissipative soliton resonance square pulses in all anomalous passively mode-locked fiber laser," *Journal of Optics*, vol. 19, no. 10, p. 105501, 2017. DOI: [10.1088/2040-8986/aa7ead](https://doi.org/10.1088/2040-8986/aa7ead).
  - [159] J. W. Nicholson and M. Andrejco, "A polarization maintaining, dispersion managed, femtosecond figure-eight fiber laser," *Optics Express*, vol. 14, no. 18, p. 8160, 2006. DOI: [10.1364/oe.14.008160](https://doi.org/10.1364/oe.14.008160).
  - [160] H. Chen, K. Lin, C. Tsai, H. Wu, C. Wu, C. Chen, Y. Chi, G. Lin, and W. Hsieh, "12 GHz passive harmonic mode-locking in a 1.06 μm semiconductor optical amplifier-based fiber laser with figure-eight cavity configuration," *Optics Letters*, vol. 38, no. 6, p. 845, 2013. DOI: [10.1364/OL.38.000845](https://doi.org/10.1364/OL.38.000845).
  - [161] N. N. Rosanov, *Spatial Hysteresis and Optical Patterns*. Springer Berlin Heidelberg, 2002. DOI: [10.1007/978-3-662-04792-7](https://doi.org/10.1007/978-3-662-04792-7).
  - [162] N. Akhmediev and A. Ankiewicz, Eds., *Dissipative Solitons*. Springer Berlin Heidelberg, 2005. DOI: [10.1007/b11728](https://doi.org/10.1007/b11728).
  - [163] X. Hachair, F. Pedaci, E. Caboche, S. Barland, M. Giudici, J. R. Tredicce, F. Prati, G. Tissoni, R. Kheradmand, L. A. Lugliato, I. Protsenko, and M. Brambilla, "Cavity solitons in a driven vcsel above threshold," *IEEE Journal of Selected Topics in Quantum Electronics*, vol. 12, no. 3, p. 339, 2006. DOI: [10.1109/JSTQE.2006.872711](https://doi.org/10.1109/JSTQE.2006.872711).

## Bibliography

---

- [164] S. Barland, M. Brambilla, L. Columbo, L. Furfaro, M. Giudici, X. Hachair, R. Kheradmand, L. A. Lugiato, T. Maggipinto, G. Tissoni, and J. Tredicce, “Cavity solitons in a VCSEL: Reconfigurable micropixel arrays,” *Europhysics News*, vol. 34, no. 4, p. 136, 2003. DOI: [10.1051/epn:2003403](https://doi.org/10.1051/epn:2003403).
- [165] O. Thual and S. Fauve, “Localized structures generated by subcritical instabilities,” *Journal de Physique*, vol. 49, no. 11, p. 1829, 1988. DOI: [10.1051/jphys:0198800490110182900](https://doi.org/10.1051/jphys:0198800490110182900).
- [166] G. Dewel, P. Borckmans, A. D. Wit, B. Rudovics, J.-J. Peraud, E. Dulos, J. Boissonade, and P. D. Kepper, “Pattern selection and localized structures in reaction-diffusion systems,” *Physica A: Statistical Mechanics and its Applications*, vol. 213, no. 1-2, p. 181, 1995. DOI: [10.1016/0378-4371\(94\)00160-u](https://doi.org/10.1016/0378-4371(94)00160-u).
- [167] Y. A. Astrov and Y. A. Logvin, “Formation of clusters of localized states in a gas discharge system via a self-completion scenario,” *Physical Review Letters*, vol. 79, no. 16, p. 2983, 1997. DOI: [10.1103/physrevlett.79.2983](https://doi.org/10.1103/physrevlett.79.2983).
- [168] Z. Bakonyi, D. Michaelis, U. Peschel, G. Onishchukov, and F. Lederer, “Dissipative solitons and their critical slowing down near a supercritical bifurcation,” *Journal of the Optical Society of America B*, vol. 19, no. 3, p. 487, 2002. DOI: [10.1364/josab.19.000487](https://doi.org/10.1364/josab.19.000487).
- [169] P. Grelu and N. Akhmediev, “Dissipative solitons for mode-locked lasers,” *Nature Photonics*, vol. 6, no. 2, p. 84, 2012. DOI: [10.1038/nphoton.2011.345](https://doi.org/10.1038/nphoton.2011.345).
- [170] J. Moores, K. Hall, S. LePage, K. Rauschenbach, W. Wong, H. Haus, and E. Ippen, “20-GHz optical storage loop/laser using amplitude modulation, filtering, and artificial fast saturable absorption,” *IEEE Photonics Technology Letters*, vol. 7, no. 9, p. 1096, 1995. DOI: [10.1109/68.414714](https://doi.org/10.1109/68.414714).
- [171] S. Barland, S. Coen, M. Erkintalo, M. Giudici, J. Javaloyes, and S. Murdoch, “Temporal localized structures in optical resonators,” *Advances in Physics: X*, vol. 2, no. 3, p. 496, 2017. DOI: [10.1080/23746149.2017.1321501](https://doi.org/10.1080/23746149.2017.1321501).
- [172] J. Tredicce, M. Giudici, and P. Glorieux, “Comment on ‘formation of repetitively nanosecond spatial solitons in a saturable AbsorberQ-switched laser’,” *Physical Review Letters*, vol. 94, no. 24, 2005. DOI: [10.1103/physrevlett.94.249401](https://doi.org/10.1103/physrevlett.94.249401).
- [173] M. Brambilla, L. A. Lugiato, and M. Stefani, “Interaction and control of optical localized structures,” *Europhysics Letters*, vol. 34, no. 2, p. 109, 1996. DOI: [10.1209/eppl/i1996-00424-4](https://doi.org/10.1209/eppl/i1996-00424-4).

- 
- [174] M. Turconi, M. Giudici, and S. Barland, “Response of laser-localized structures to external perturbations in coupled semiconductor microcavities,” *Philosophical Transactions of the Royal Society A: Mathematical, Physical and Engineering Sciences*, vol. 372, no. 2027, p. 2014004, 2014. DOI: 10.1098/rsta.2014.0004.
  - [175] F. Pedaci, P. Genevet, S. Barland, M. Giudici, and J. R. Tredicce, “Positioning cavity solitons with a phase mask,” *Applied Physics Letters*, vol. 89, no. 22, p. 221111, 2006. DOI: 10.1063/1.2388867.
  - [176] M. Giudici, F. Pedaci, E. Caboche, P. Genevet, S. Barland, J. Tredicce, G. Tissoni, and L. Lugiato, “Cavity solitons in vertical cavity surface emitting lasers and their applications,” in *Localized States in Physics: Solitons and Patterns*, Springer Berlin Heidelberg, 2010, p. 141. DOI: 10.1007/978-3-642-16549-8\_8.
  - [177] W. J. Firth and A. J. Scroggie, “Optical bullet holes: Robust controllable localized states of a nonlinear cavity,” *Physical Review Letters*, vol. 76, no. 10, p. 1623, 1996. DOI: 10.1103/physrevlett.76.1623.
  - [178] S. Barland, M. Giudici, and G.-L. Lippi, “Semiconductor lasers: coherence and localized states,” in *Université Côte d’Azur Complex Days*, 2018, p. 165. [Online]. Available: <https://hal.archives-ouvertes.fr/hal-02016004>.
  - [179] P. Coullet, C. Riera, and C. Tresser, “Stable static localized structures in one dimension,” *Physical Review Letters*, vol. 84, no. 14, p. 3069, 2000. DOI: 10.1103/PhysRevLett.84.3069.
  - [180] J. Burke and E. Knobloch, “Localized states in the generalized swift-hohenberg equation,” *Physical Review E*, vol. 73, no. 5, 2006. DOI: 10.1103/physreve.73.056211.
  - [181] P. Genevet, M. Turconi, S. Barland, M. Giudici, and J. Tredicce, “Bifurcation diagram and control of localized laser structures,” *Journal of Nonlinear Optical Physics & Materials*, vol. 21, no. 03, p. 1250029, 2012. DOI: 10.1142/s0218863512500294.
  - [182] P. Genevet, S. Barland, M. Giudici, and J. R. Tredicce, “Cavity soliton laser based on coupled micro-resonators,” in *Localized States in Physics: Solitons and Patterns*, Springer Berlin Heidelberg, 2010, p. 169. DOI: 10.1007/978-3-642-16549-8\_9.

## Bibliography

---

- [183] P. Woods and A. Champneys, “Heteroclinic tangles and homoclinic snaking in the unfolding of a degenerate reversible hamiltonian–hopf bifurcation,” *Physica D: Nonlinear Phenomena*, vol. 129, no. 3-4, p. 147, 1999. DOI: [10.1016/s0167-2789\(98\)00309-1](https://doi.org/10.1016/s0167-2789(98)00309-1).
- [184] P. Coullet, “Localized patterns and fronts in nonequilibrium systems,” *International Journal of Bifurcation and Chaos*, vol. 12, no. 11, p. 2445, 2002. DOI: [10.1142/s021812740200614x](https://doi.org/10.1142/s021812740200614x).
- [185] P. Coullet, C. Riera, and C. Tresser, “A new approach to data storage using localized structures,” *Chaos: An Interdisciplinary Journal of Nonlinear Science*, vol. 14, no. 1, p. 193, 2004. DOI: [10.1063/1.1642311](https://doi.org/10.1063/1.1642311).
- [186] G. Giacomelli and A. Politi, “Relationship between delayed and spatially extended dynamical systems,” *Physical Review Letters*, vol. 76, no. 15, p. 2686, 1996. DOI: [10.1103/physrevlett.76.2686](https://doi.org/10.1103/physrevlett.76.2686).
- [187] B. Garbin, J. Javaloyes, G. Tissoni, and S. Barland, “Topological solitons as addressable phase bits in a driven laser,” *Nature Communications*, vol. 6, no. 1, 2015. DOI: [10.1038/ncomms6915](https://doi.org/10.1038/ncomms6915).
- [188] B. Garbin, J. Javaloyes, S. Barland, and G. Tissoni, “Interactions and collisions of topological solitons in a semiconductor laser with optical injection and feedback,” *Chaos: An Interdisciplinary Journal of Nonlinear Science*, vol. 27, no. 11, p. 114308, 2017. DOI: [10.1063/1.5006751](https://doi.org/10.1063/1.5006751).
- [189] J. M. McSloy, W. J. Firth, G. K. Harkness, and G.-L. Oppo, “Computationally determined existence and stability of transverse structures. II. multipeaked cavity solitons,” *Physical Review E*, vol. 66, no. 4, 2002. DOI: [10.1103/physreve.66.046606](https://doi.org/10.1103/physreve.66.046606).
- [190] S. Balle, S. Barland, M. Giudici, J. Tredicce, and M. Brambilla, “Localised structures in edge emitter semiconductor lasers,” in *2003 European Quantum Electronics Conference. EQEC 2003 (IEEE Cat No.03TH8665)*, 2003. DOI: [10.1109/eqec.2003.1313880](https://doi.org/10.1109/eqec.2003.1313880).
- [191] S. Barland, J. R. Tredicce, M. Brambilla, L. A. Lugiato, S. Balle, M. Giudici, T. Maggipinto, L. Spinelli, G. Tissoni, T. Knödl, M. Miller, and R. Jäger, “Cavity solitons as pixels in semiconductor microcavities,” *Nature*, vol. 419, no. 6908, p. 699, 2002. DOI: [10.1038/nature01049](https://doi.org/10.1038/nature01049).
- [192] P. Genevet, S. Barland, M. Giudici, and J. R. Tredicce, “Cavity soliton laser based on mutually coupled semiconductor microresonators,” *Physical Review Letters*, vol. 101, no. 12, 2008. DOI: [10.1103/physrevlett.101.123905](https://doi.org/10.1103/physrevlett.101.123905).

- 
- [193] L. A. Lugiato, “Introduction to the Feature Section on Cavity Solitons: An Overview,” *IEEE Journal of Quantum Electronics*, vol. 39, no. 2, p. 193, 2003. DOI: [10.1109/JQE.2002.807195](https://doi.org/10.1109/JQE.2002.807195).
- [194] Y. Tanguy, T. Ackemann, W. J. Firth, and R. Jäger, “Realization of a semiconductor-based cavity soliton laser,” *Physical Review Letters*, vol. 100, no. 1, 2008. DOI: [10.1103/physrevlett.100.013907](https://doi.org/10.1103/physrevlett.100.013907).
- [195] N. N. Rozanov and G. V. Khodova, “Autosolitons in bistable interferometers,” *Optics and Spectroscopy*, vol. 65, p. 449, 1988.
- [196] P. Genevet, S. Barland, M. Giudici, and J. R. Tredicce, “Bistable and addressable localized vortices in semiconductor lasers,” *Physical Review Letters*, vol. 104, no. 22, 2010. DOI: [10.1103/physrevlett.104.223902](https://doi.org/10.1103/physrevlett.104.223902).
- [197] H. Bao, A. Cooper, M. Rowley, L. D. Lauro, J. S. T. Gongora, S. T. Chu, B. E. Little, G.-L. Oppo, R. Morandotti, D. J. Moss, B. Wetzel, M. Peccianti, and A. Pasquazi, “Laser cavity-soliton microcombs,” *Nature Photonics*, vol. 13, no. 6, p. 384, 2019. DOI: [10.1038/s41566-019-0379-5](https://doi.org/10.1038/s41566-019-0379-5).
- [198] E. Obrzud, M. Rainer, A. Harutyunyan, M. H. Anderson, J. Liu, M. Geiselman, B. Chazelas, S. Kundermann, S. Lecomte, M. Cecconi, A. Ghedina, E. Molinari, F. Pepe, F. Wildi, F. Bouchy, T. J. Kippenberg, and T. Herr, “A microphotonic astrocomb,” *Nature Photonics*, vol. 13, no. 1, p. 31, 2018. DOI: [10.1038/s41566-018-0309-y](https://doi.org/10.1038/s41566-018-0309-y).
- [199] E. Obrzud, S. Lecomte, and T. Herr, “Temporal solitons in microresonators driven by optical pulses,” *Nature Photonics*, vol. 11, no. 9, p. 600, 2017. DOI: [10.1038/nphoton.2017.140](https://doi.org/10.1038/nphoton.2017.140).
- [200] Q.-F. Yang, X. Yi, K. Y. Yang, and K. Vahala, “Counter-propagating solitons in microresonators,” *Nature Photonics*, vol. 11, no. 9, p. 560, 2017. DOI: [10.1038/nphoton.2017.117](https://doi.org/10.1038/nphoton.2017.117).
- [201] S. A. Miller, Y. Okawachi, S. Ramelow, K. Luke, A. Dutt, A. Farsi, A. L. Gaeta, and M. Lipson, “Tunable frequency combs based on dual microring resonators,” *Optics Express*, vol. 23, no. 16, p. 21527, 2015. DOI: [10.1364/oe.23.021527](https://doi.org/10.1364/oe.23.021527).
- [202] J. L. Oudar, R. Kuszelewicz, B. Sfez, J. C. Michel, and R. Planel, “Prospects for further threshold reduction in bistable microresonators,” *Optical and Quantum Electronics*, vol. 24, no. 2, S193, 1992. DOI: [10.1007/bf00625824](https://doi.org/10.1007/bf00625824).

## Bibliography

---

- [203] R. Kuszelewicz, I. Ganne, I. Sagnes, G. Slekys, and M. Brambilla, “Optical self-organization in bulk and multiquantum well GaAlAs microresonators,” *Physical Review Letters*, vol. 84, no. 26, p. 6006, 2000. DOI: [10.1103/physrevlett.84.6006](https://doi.org/10.1103/physrevlett.84.6006).
- [204] X. Hachair, S. Barland, L. Furfaro, M. Giudici, S. Balle, J. R. Tredicce, M. Brambilla, T. Maggipinto, I. M. Perrini, G. Tissoni, and L. Lugiato, “Cavity solitons in broad-area vertical-cavity surface-emitting lasers below threshold,” *Physical Review A*, vol. 69, no. 4, 2004. DOI: [10.1103/physreva.69.043817](https://doi.org/10.1103/physreva.69.043817).
- [205] F. Pedaci, S. Barland, E. Caboche, P. Genevet, M. Giudici, J. R. Tredicce, T. Ackemann, A. J. Scroggie, W. J. Firth, G.-L. Oppo, G. Tissoni, and R. Jäger, “All-optical delay line using semiconductor cavity solitons,” *Applied Physics Letters*, vol. 92, no. 1, p. 011 101, 2008. DOI: [10.1063/1.2828458](https://doi.org/10.1063/1.2828458).
- [206] Y. Menesguen, S. Barbay, X. Hachair, L. Leroy, I. Sagnes, and R. Kuszelewicz, “Optical self-organization and cavity solitons in optically pumped semiconductor microresonators,” *Physical Review A*, vol. 74, no. 2, p. 023 818, 2006. DOI: [10.1103/physreva.74.023818](https://doi.org/10.1103/physreva.74.023818).
- [207] M. Saffman, D. Montgomery, and D. Z. Anderson, “Collapse of a transverse-mode continuum in a self-imaging photorefractively pumped ring resonator,” *Optics Letters*, vol. 19, no. 8, p. 518, 1994. DOI: [10.1364/ol.19.000518](https://doi.org/10.1364/ol.19.000518).
- [208] S. Barbay, Y. Ménesguen, X. Hachair, L. Leroy, I. Sagnes, and R. Kuszelewicz, “Incoherent and coherent writing and erasure of cavity solitons in an optically pumped semiconductor amplifier,” *Optics Letters*, vol. 31, no. 10, p. 1504, 2006. DOI: [10.1364/ol.31.001504](https://doi.org/10.1364/ol.31.001504).
- [209] M. Marconi, J. Javaloyes, S. Barland, S. Balle, and M. Giudici, “Vectorial dissipative solitons in vertical-cavity surface-emitting lasers with delays,” *Nature Photonics*, vol. 9, no. 7, p. 450, 2015. DOI: [10.1038/nphoton.2015.92](https://doi.org/10.1038/nphoton.2015.92).
- [210] O. Okhotnikov, A. Grudinin, and M. Pessa, “Ultra-fast fibre laser systems based on SESAM technology: New horizons and applications,” *New Journal of Physics*, vol. 6, p. 177, 2004. DOI: [10.1088/1367-2630/6/1/177](https://doi.org/10.1088/1367-2630/6/1/177).
- [211] H. Zhang, D. Y. Tang, L. M. Zhao, and H. Y. Tam, “Induced solitons formed by cross-polarization coupling in a birefringent cavity fiber laser,” *Optics Letters*, vol. 33, no. 20, p. 2317, 2008. DOI: [10.1364/ol.33.002317](https://doi.org/10.1364/ol.33.002317).
- [212] L. M. Zhao, D. Y. Tang, and J. Wu, “Gain-guided soliton in a positive group-dispersion fiber laser,” *Optics Letters*, vol. 31, no. 12, p. 1788, 2006. DOI: [10.1364/ol.31.001788](https://doi.org/10.1364/ol.31.001788).

- 
- [213] L. Yun, X. Liu, and D. Mao, “Observation of dual-wavelength dissipative solitons in a figure-eight erbium-doped fiber laser,” *Optics Express*, vol. 20, no. 19, p. 20992, 2012. DOI: [10.1364/oe.20.020992](https://doi.org/10.1364/oe.20.020992).
  - [214] A. Grudinin, D. Richardson, and D. Payne, “Energy quantisation in figure eight fibre laser,” *Electronics Letters*, vol. 28, no. 1, p. 67, 1992. DOI: [10.1049/el:19920042](https://doi.org/10.1049/el:19920042).
  - [215] D. Y. Tang, L. M. Zhao, B. Zhao, and A. Q. Liu, “Mechanism of multisoliton formation and soliton energy quantization in passively mode-locked fiber lasers,” *Physical Review A*, vol. 72, no. 4, p. 043816, 2005. DOI: [10.1103/physreva.72.043816](https://doi.org/10.1103/physreva.72.043816).
  - [216] A. Komarov, K. Komarov, and F. Sanchez, “Quantization of binding energy of structural solitons in passive mode-locked fiber lasers,” *Physical Review A*, vol. 79, no. 3, p. 033807, 2009. DOI: [10.1103/physreva.79.033807](https://doi.org/10.1103/physreva.79.033807).
  - [217] D. Y. Tang, B. Zhao, L. M. Zhao, and H. Y. Tam, “Soliton interaction in a fiber ring laser,” *Physical Review E*, vol. 72, no. 1, p. 016616, 2005. DOI: [10.1103/physreve.72.016616](https://doi.org/10.1103/physreve.72.016616).
  - [218] A. Haboucha, H. Leblond, M. Salhi, A. Komarov, and F. Sanchez, “Analysis of soliton pattern formation in passively mode-locked fiber lasers,” *Physical Review A*, vol. 78, no. 4, p. 043806, 2008. DOI: [10.1103/physreva.78.043806](https://doi.org/10.1103/physreva.78.043806).
  - [219] G. Sobon, J. Sotor, and K. M. Abramski, “Passive harmonic mode-locking in er-doped fiber laser based on graphene saturable absorber with repetition rates scalable to 2.22 GHz,” *Applied Physics Letters*, vol. 100, no. 16, p. 161109, 2012. DOI: [10.1063/1.4704913](https://doi.org/10.1063/1.4704913).
  - [220] C. Lecaplain, P. Grelu, and S. Wabnitz, “Polarization-domain-wall complexes in fiber lasers,” *Journal of the Optical Society of America B: Optical Physics*, vol. 30, no. 1, p. 211, 2013. DOI: [10.1364/JOSAB.30.000211](https://doi.org/10.1364/JOSAB.30.000211).
  - [221] Z.-C. Luo, M. Liu, H. Liu, X.-W. Zheng, A.-P. Luo, C.-J. Zhao, H. Zhang, S.-C. Wen, and W.-C. Xu, “2GHz passively harmonic mode-locked fiber laser by a microfiber-based topological insulator saturable absorber,” *Optics Letters*, vol. 38, no. 24, p. 5212, 2013. DOI: [10.1364/ol.38.005212](https://doi.org/10.1364/ol.38.005212).
  - [222] F. Amrani, A. Haboucha, M. Salhi, H. Leblond, A. Komarov, and F. Sanchez, “Dissipative solitons compounds in a fiber laser. analogy with the states of the matter,” *Applied Physics B*, vol. 99, no. 1-2, p. 107, 2009. DOI: [10.1007/s00340-009-3774-7](https://doi.org/10.1007/s00340-009-3774-7).

## Bibliography

---

- [223] F. Amrani, M. Salhi, H. Leblond, and F. Sanchez, “Characterization of soliton compounds in a passively mode-locked high power fiber laser,” *Optics Communications*, vol. 283, no. 24, p. 5224, 2010. DOI: [10.1016/j.optcom.2010.08.003](https://doi.org/10.1016/j.optcom.2010.08.003).
- [224] Y. F. Song, L. Li, H. Zhang, D. Y. Shen, D. Y. Tang, and K. P. Loh, “Vector multi-soliton operation and interaction in a graphene mode-locked fiber laser,” *Optics Express*, vol. 21, no. 8, p. 10 010, 2013. DOI: [10.1364/oe.21.010010](https://doi.org/10.1364/oe.21.010010).
- [225] S. Chouli and P. Grelu, “Rains of solitons in a fiber laser,” *Optics Express*, vol. 17, no. 14, p. 11 776, 2009. DOI: [10.1364/oe.17.011776](https://doi.org/10.1364/oe.17.011776).
- [226] ——, “Soliton rains in a fiber laser: An experimental study,” *Physical Review A*, vol. 81, no. 6, p. 063 829, 2010. DOI: [10.1103/PhysRevA.81.063829](https://doi.org/10.1103/PhysRevA.81.063829).
- [227] C. R. Menyuk, “Stability of solitons in birefringent optical fibers i: Equal propagation amplitudes,” *Optics Letters*, vol. 12, no. 8, p. 614, 1987. DOI: [10.1364/ol.12.000614](https://doi.org/10.1364/ol.12.000614).
- [228] ——, “Stability of solitons in birefringent optical fibers II arbitrary amplitudes,” *Journal of the Optical Society of America B*, vol. 5, no. 2, p. 392, 1988. DOI: [10.1364/josab.5.000392](https://doi.org/10.1364/josab.5.000392).
- [229] M. N. Islam, C. D. Poole, and J. P. Gordon, “Soliton trapping in birefringent optical fibers,” *Optics Letters*, vol. 14, no. 18, p. 1011, 1989. DOI: [10.1364/ol.14.001011](https://doi.org/10.1364/ol.14.001011).
- [230] V. V. Afanasjev, “Soliton polarization rotation in fiber lasers,” *Optics Letters*, vol. 20, no. 3, p. 270, 1995. DOI: [10.1364/ol.20.000270](https://doi.org/10.1364/ol.20.000270).
- [231] S. Cundiff, B. Collings, and W. Knox, “Polarization locking in an isotropic, modelocked soliton er/yb fiber laser,” *Optics Express*, vol. 1, no. 1, p. 12, 1997. DOI: [10.1364/oe.1.000012](https://doi.org/10.1364/oe.1.000012).
- [232] S. T. Cundiff, B. C. Collings, N. N. Akhmediev, J. M. Soto-Crespo, K. Bergman, and W. H. Knox, “Observation of polarization-locked vector solitons in an optical fiber,” *Physical Review Letters*, vol. 82, no. 20, p. 3988, 1999. DOI: [10.1103/physrevlett.82.3988](https://doi.org/10.1103/physrevlett.82.3988).
- [233] D. Y. Tang, H. Zhang, L. M. Zhao, and X. Wu, “Observation of high-order polarization-locked vector solitons in a fiber laser,” *Physical Review Letters*, vol. 101, no. 15, p. 153 904, 2008. DOI: [10.1103/physrevlett.101.153904](https://doi.org/10.1103/physrevlett.101.153904).
- [234] L. M. Zhao, D. Y. Tang, H. Zhang, X. Wu, and N. Xiang, “Soliton trapping in fiber lasers,” *Optics Express*, vol. 16, no. 13, p. 9528, 2008. DOI: [10.1364/oe.16.009528](https://doi.org/10.1364/oe.16.009528).

- 
- [235] L. M. Zhao, D. Y. Tang, X. Wu, H. Zhang, and H. Y. Tam, “Coexistence of polarization-locked and polarization-rotating vector solitons in a fiber laser with SESAM,” *Optics Letters*, vol. 34, no. 20, p. 3059, 2009. DOI: 10.1364/ol.34.003059.
- [236] H. Zhang, D. Y. Tang, L. M. Zhao, X. Wu, and H. Y. Tam, “Dissipative vector solitons in a dispersionmanaged cavity fiber laser with net positive cavity dispersion,” *Optics Express*, vol. 17, no. 2, p. 455, 2009. DOI: 10.1364/oe.17.000455.
- [237] C. Mou, S. Sergeyev, A. Rozhin, and S. Turistyn, “All-fiber polarization locked vector soliton laser using carbon nanotubes,” *Optics Letters*, vol. 36, no. 19, p. 3831, 2011. DOI: 10.1364/ol.36.003831.
- [238] D. Mao, X. Liu, and H. Lu, “Observation of pulse trapping in a near-zero dispersion regime,” *Optics Letters*, vol. 37, no. 13, p. 2619, 2012. DOI: 10.1364/ol.37.002619.
- [239] Y. F. Song, H. Zhang, D. Y. Tang, and D. Y. Shen, “Polarization rotation vector solitons in a graphene mode-locked fiber laser,” *Optics Express*, vol. 20, no. 24, p. 27 283, 2012. DOI: 10.1364/oe.20.027283.
- [240] X. Yuan, T. Yang, J. Chen, X. He, H. Huang, S. Xu, and Z. Yang, “Experimental observation of vector solitons in a highly birefringent cavity of ytterbium-doped fiber laser,” *Optics Express*, vol. 21, no. 20, p. 23 866, 2013. DOI: 10.1364/oe.21.023866.
- [241] Z.-C. Luo, Q.-Y. Ning, H.-L. Mo, H. Cui, J. Liu, L.-J. Wu, A.-P. Luo, and W.-C. Xu, “Vector dissipative soliton resonance in a fiber laser,” *Optics Express*, vol. 21, no. 8, p. 10 199, 2013. DOI: 10.1364/oe.21.010199.
- [242] H. Zhang, D. Y. Tang, X. Wu, and L. M. Zhao, “Multi-wavelength dissipative soliton operation of an erbium-doped fiber laser,” *Optics Express*, vol. 17, no. 15, p. 12 692, 2009. DOI: 10.1364/oe.17.012692.
- [243] Z.-C. Luo, A.-P. Luo, and W.-C. Xu, “Tunable and switchable multiwavelength passively mode-locked fiber laser based on SESAM and inline birefringence comb filter,” *IEEE Photonics Journal*, vol. 3, no. 1, p. 64, 2011. DOI: 10.1109/jphot.2010.2102012.
- [244] Q.-Y. Ning, H. Liu, X.-W. Zheng, W. Yu, A.-P. Luo, X.-G. Huang, Z.-C. Luo, W.-C. Xu, S.-H. Xu, and Z.-M. Yang, “Vector nature of multi-soliton patterns in a passively mode-locked figure-eight fiber laser,” *Optics Express*, vol. 22, no. 10, p. 11 900, 2014. DOI: 10.1364/oe.22.011900.

## Bibliography

---

- [245] R. Michalzik, Ed., *VCSELs, Fundamentals, Technology and Applications of Vertical-Cavity Surface-Emitting Lasers*. Springer Berlin Heidelberg, 2013. DOI: [10.1007/978-3-642-24986-0](https://doi.org/10.1007/978-3-642-24986-0).
- [246] M. Giudici, S. Balle, T. Ackemann, S. Barland, and J. R. Tredicce, “Polarization dynamics in vertical-cavity surface-emitting lasers with optical feedback: Experiment and model,” *Journal of the Optical Society of America B*, vol. 16, no. 11, p. 2114, 1999. DOI: [10.1364/josab.16.002114](https://doi.org/10.1364/josab.16.002114).
- [247] J. Mulet, M. Giudici, J. Javaloyes, and S. Balle, “Square-wave switching by crossed-polarization gain modulation in vertical-cavity semiconductor lasers,” *Physical Review A*, vol. 76, no. 4, p. 043801, 2007. DOI: [10.1103/physreva.76.043801](https://doi.org/10.1103/physreva.76.043801).
- [248] J. Javaloyes, M. Marconi, and M. Giudici, “Phase dynamics in vertical-cavity surface-emitting lasers with delayed optical feedback and cross-polarized re-injection,” *Physical Review A*, vol. 90, no. 2, p. 023838, 2014. DOI: [10.1103/physreva.90.023838](https://doi.org/10.1103/physreva.90.023838).
- [249] M. Marconi, S. Barland, and M. Giudici, “Nonvolatile polarization control of a bistable VCSEL,” *Optics Express*, vol. 20, no. 26, p. B299, 2012. DOI: [10.1364/oe.20.00b299](https://doi.org/10.1364/oe.20.00b299).
- [250] M. Marconi, J. Javaloyes, S. Barland, M. Giudici, and S. Balle, “Robust square-wave polarization switching in vertical-cavity surface-emitting lasers,” *Physical Review A*, vol. 87, no. 1, p. 013827, 2013. DOI: [10.1103/physreva.87.013827](https://doi.org/10.1103/physreva.87.013827).
- [251] F. T. Arecchi, G. Giacomelli, A. Lapucci, and R. Meucci, “Two-dimensional representation of a delayed dynamical system,” *Physical Review A*, vol. 45, no. 7, p. R4225, 1992. DOI: [10.1103/physreva.45.r4225](https://doi.org/10.1103/physreva.45.r4225).
- [252] K. G. Wilcox, A. C. Tropper, H. E. Beere, D. A. Ritchie, B. Kunert, B. Heinen, and W. Stoltz, “435 kW peak power femtosecond pulse mode-locked VECSEL for supercontinuum generation,” *Optics Express*, vol. 21, no. 2, p. 1599, 2013. DOI: [10.1364/oe.21.001599](https://doi.org/10.1364/oe.21.001599).
- [253] M. Marconi, J. Javaloyes, S. Balle, and M. Giudici, “Passive mode-locking and tilted waves in broad-area vertical-cavity surface-emitting lasers,” *IEEE Journal of Selected Topics in Quantum Electronics*, vol. 21, no. 1, p. 85, 2015. DOI: [10.1109/jstqe.2014.2346614](https://doi.org/10.1109/jstqe.2014.2346614).
- [254] A. G. Vladimirov and D. Turaev, “Model for passive mode locking in semiconductor lasers,” *Physical Review A*, vol. 72, no. 3, p. 033808, 2005. DOI: [10.1103/physreva.72.033808](https://doi.org/10.1103/physreva.72.033808).

- 
- [255] BATOP GmbH, *FC heat sink with TEC and thermistor: specification sheet*, BATOP GmbH. [Online]. Available: [https://www.batop.de/products/saturable-absorber/resonant-saturable-absorber-mirror/data-sheet-mounts/mounted\\_FC\\_TEC.pdf](https://www.batop.de/products/saturable-absorber/resonant-saturable-absorber-mirror/data-sheet-mounts/mounted_FC_TEC.pdf).
- [256] P. Camelin, J. Javaloyes, M. Marconi, and M. Giudici, “Electrical addressing and temporal tweezing of localized pulses in passively-mode-locked semiconductor lasers,” *Physical Review A*, vol. 94, no. 6, p. 063854, 2016. DOI: [10.1103/PhysRevA.94.063854](https://doi.org/10.1103/PhysRevA.94.063854).
- [257] J. Tu and J. N. Kutz, “Pulse formation, harmonic mode-locking, and stability in actively mode-locked laser cavities,” *IEEE Journal of Quantum Electronics*, vol. 45, no. 3, p. 282, 2009. DOI: [10.1109/jqe.2009.2013143](https://doi.org/10.1109/jqe.2009.2013143).
- [258] G. Keiser, *Optical Fiber Communications*. Boston: McGraw-Hill College, 1999, ISBN: 0072321016.
- [259] THORLABS, *SOA image from THORLABS website*. [Online]. Available: [https://www.thorlabs.com/newgroupage9.cfm?objectgroup\\_id=3901](https://www.thorlabs.com/newgroupage9.cfm?objectgroup_id=3901).
- [260] BATOP GmbH, *Saturable Absorbers - Mounting Options*. [Online]. Available: [https://www.batop.de/products/overview/Poster\\_Mounting.pdf](https://www.batop.de/products/overview/Poster_Mounting.pdf).
- [261] ——, *RSAM Data Sheet*, BATOP GmbH. [Online]. Available: <https://www.batop.de/products/saturable-absorber/resonant-saturable-absorber-mirror/data-sheet/resonant-saturable-absorber-mirror-1550nm/resonant-saturable-absorber-mirror-RSAM-1550-10ps.pdf>.
- [262] NEWPORT. [Online]. Available: <https://www.newport.com/p/TBF-1550-1.0-FCAPC>.
- [263] OZ OPTICS, *Manually adjustable polarization insensitive tunable filters*, OZ OPTICS. [Online]. Available: [https://www.ozoptics.com/ALLNEW\\_PDF/DTS0051.pdf](https://www.ozoptics.com/ALLNEW_PDF/DTS0051.pdf).
- [264] THORLABS, *Manual fiber polarization controllers*, THORLABS. [Online]. Available: <https://www.thorlabs.com/drawings/8744eb99d4fdf6b1-D812511C-B621-6B3A-986B8C5765509B9E/FPC030-Manual.pdf>.
- [265] H. A. Haus, “Mode-locking of lasers,” *IEEE Journal of Selected Topics in Quantum Electronics*, vol. 6, no. 6, p. 1173, 2000. DOI: [10.1109/2944.902165](https://doi.org/10.1109/2944.902165).
- [266] V. Moskalenko, S. Latkowski, S. Tahvili, T. de Vries, M. Smit, and E. Bente, “Record bandwidth and sub-picosecond pulses from a monolithically integrated mode-locked quantum well ring laser,” *Optics Express*, vol. 22, no. 23, p. 28865, 2014. DOI: [10.1364/oe.22.028865](https://doi.org/10.1364/oe.22.028865).

## Bibliography

---

- [267] J. P. Zhuang, V. Pusino, Y. Ding, S. C. Chan, and M. Sorel, “Experimental investigation of anti-colliding pulse mode-locked semiconductor lasers,” *Optics Letters*, vol. 40, no. 4, p. 617, 2015. DOI: [10.1364/ol.40.000617](https://doi.org/10.1364/ol.40.000617).
- [268] S. Chen, A. Sato, T. Ito, M. Yoshita, H. Akiyama, and H. Yokoyama, “Sub-5-ps optical pulse generation from a 155- $\mu\text{m}$  distributed-feedback laser diode with nanosecond electric pulse excitation and spectral filtering,” *Optics Express*, vol. 20, no. 22, p. 24843, 2012. DOI: [10.1364/oe.20.024843](https://doi.org/10.1364/oe.20.024843).
- [269] J. Mark and J. Mørk, “Subpicosecond gain dynamics in InGaAsP optical amplifiers: Experiment and theory,” *Applied Physics Letters*, vol. 61, no. 19, p. 2281, 1992. DOI: [10.1063/1.108265](https://doi.org/10.1063/1.108265).
- [270] J. He and K. T. Chan, “All-optical actively modelocked fibre ring laser based on cross-gain modulation in SOA,” *Electronics Letters*, vol. 38, no. 24, p. 1504, 2002. DOI: [10.1049/el:20021082](https://doi.org/10.1049/el:20021082).
- [271] J. W. D. Chi, A. Fernandez, and C. Lu, “Properties of mode-locked optical pulses in a dispersion-managed fiber-ring laser using semiconductor optical amplifier as active device,” *IEEE Journal of Quantum Electronics*, vol. 49, no. 1, p. 80, 2013. DOI: [10.1109/jqe.2012.2230317](https://doi.org/10.1109/jqe.2012.2230317).
- [272] M. Tlidi, K. Staliunas, K. Panajotov, A. G. Vladimirov, and M. G. Clerc, “Localized structures in dissipative media: From optics to plant ecology,” *Philosophical Transactions of the Royal Society A: Mathematical, Physical and Engineering Sciences*, vol. 372, no. 2027, p. 20140101, 2014. DOI: [10.1098/rsta.2014.0101](https://doi.org/10.1098/rsta.2014.0101).
- [273] P. B. Umbanhowar, F. Melo, and H. L. Swinney, “Localized excitations in a vertically vibrated granular layer,” *Nature*, vol. 382, no. 6594, p. 793, 1996. DOI: [10.1038/382793a0](https://doi.org/10.1038/382793a0).
- [274] Y. A. Astrov and H.-G. Purwins, “Plasma spots in a gas discharge system: Birth, scattering and formation of molecules,” *Physics Letters A*, vol. 283, no. 5, p. 349, 2001. DOI: [10.1016/S0375-9601\(01\)00257-2](https://doi.org/10.1016/S0375-9601(01)00257-2).
- [275] F.-J. Niedernostheide, A. Arps, R. Dohmen, H. Willebrand, and H.-G. Purwins, “Spatial and spatio-temporal patterns in pn-pn semiconductor devices,” *Physica Status Solidi BBasic Solid State Physics*, vol. 172, no. 1, p. 249, 1992. DOI: [10.1002/pssb.2221720123](https://doi.org/10.1002/pssb.2221720123).
- [276] K.-J. Lee, W. D. McCormick, J. E. Pearson, and H. L. Swinney, “Experimental observation of self-replicating spots in a reaction-diffusion system,” *Nature*, vol. 369, no. 6477, p. 215, 1994. DOI: [10.1038/369215a0](https://doi.org/10.1038/369215a0).

- 
- [277] J. Wu, R. Keolian, and I. Rudnick, “Observation of a nonpropagating hydrodynamic soliton,” *Physical Review Letters*, vol. 52, no. 16, p. 1421, 1984. DOI: [10.1103/PhysRevLett.52.1421](https://doi.org/10.1103/PhysRevLett.52.1421).
- [278] E. Moses, J. Fineberg, and V. Steinberg, “Multistability and confined traveling-wave patterns in a convecting binary mixture,” *Physical Review A*, vol. 35, no. 6, p. 2757, 1987. DOI: [10.1103/PhysRevA.35.2757](https://doi.org/10.1103/PhysRevA.35.2757).
- [279] L. A. Lugiato, “Transverse nonlinear optics: Introduction and review,” *Chaos, Solitons & Fractals*, vol. 4, no. 8-9, p. 1251, 1994. DOI: [10.1016/0960-0779\(94\)90080-9](https://doi.org/10.1016/0960-0779(94)90080-9).
- [280] P. Mandel and M. Tlidi, “Transverse dynamics in cavity nonlinear optics (2000–2003),” *Journal of Optics B: Quantum and Semiclassical Optics*, vol. 6, no. 9, p. R60, 2004. DOI: [10.1088/1464-4266/6/9/R02](https://doi.org/10.1088/1464-4266/6/9/R02).
- [281] N. N. Rosanov, S. V. Fedorov, and A. N. Shatsev, “Dissipative solitons in laser systems with non-local and non-instantaneous nonlinearity,” in *Dissipative Solitons: From Optics to Biology and Medicine*. Berlin, Heidelberg: Springer Berlin Heidelberg, 2008, p. 1. DOI: [10.1007/978-3-540-78217-9\\_4](https://doi.org/10.1007/978-3-540-78217-9_4).
- [282] F. Leo, S. Coen, P. Kockaert, S.-P. Gorza, P. Emplit, and M. Haelterman, “Temporal cavity solitons in one-dimensional Kerr media as bits in an all-optical buffer,” *Nature Photonics*, vol. 4, no. 7, p. 471, 2010. DOI: [10.1038/nphoton.2010.120](https://doi.org/10.1038/nphoton.2010.120).
- [283] T. Herr, V. Brasch, J. D. Jost, C. Y. Wang, N. M. Kondratiev, M. L. Gorodetsky, and T. J. Kippenberg, “Temporal solitons in optical microresonators,” *Nature Photonics*, vol. 8, no. 2, p. 145, 2014. DOI: [10.1038/nphoton.2013.343](https://doi.org/10.1038/nphoton.2013.343).
- [284] M. Tlidi and L. Gelens, “High-order dispersion stabilizes dark dissipative solitons in all-fiber cavities,” *Optics Letters*, vol. 35, no. 3, p. 306, 2010. DOI: [10.1364/OL.35.000306](https://doi.org/10.1364/OL.35.000306).
- [285] M. Tlidi, L. Bahloul, L. Cherbi, A. Hariz, and S. Coulibaly, “Drift of dark cavity solitons in a photonic-crystal fiber resonator,” *Physical Review A*, vol. 88, no. 3, p. 1, 2013. DOI: [10.1103/PhysRevA.88.035802](https://doi.org/10.1103/PhysRevA.88.035802).
- [286] D. Y. Tang, W. S. Man, H. Y. Tam, and P. D. Drummond, “Observation of bound states of solitons in a passively mode-locked fiber laser,” *Physical Review A*, vol. 64, no. 3, p. 033814, 2001. DOI: [10.1103/PhysRevA.64.033814](https://doi.org/10.1103/PhysRevA.64.033814).

## Bibliography

---

- [287] P. Grelu and J. Soto-Crespo, “Temporal soliton “molecules” in mode-locked lasers: Collisions, pulsations, and vibrations,” in *Dissipative Solitons: From Optics to Biology and Medicine*. Berlin, Heidelberg: Springer Berlin Heidelberg, 2008, p. 1. DOI: [10.1007/978-3-540-78217-9\\_6](https://doi.org/10.1007/978-3-540-78217-9_6).
- [288] J. K. Jang, M. Erkintalo, S. G. Murdoch, and S. Coen, “Ultraweak long-range interactions of solitons observed over astronomical distances,” *Nature Photonics*, vol. 7, no. 8, p. 657, 2013. DOI: [10.1038/NPHOTON.2013.157](https://doi.org/10.1038/NPHOTON.2013.157).
- [289] S. T. Cundiff, J. M. Soto-Crespo, and N. Akhmediev, “Experimental evidence for soliton explosions,” *Physical Review Letters*, vol. 88, no. 7, p. 073903, 2002. DOI: [10.1103/PhysRevLett.88.073903](https://doi.org/10.1103/PhysRevLett.88.073903).
- [290] I. N. Duling, “All-fiber ring soliton laser mode-locked with a nonlinear mirror,” *Optics Letters*, vol. 16, no. 8, p. 539, 1991. DOI: [10.1364/OL.16.000539](https://doi.org/10.1364/OL.16.000539).
- [291] R. Manning, A. Kelly, K. Blow, A. Poustie, and D. Nessel, “Semiconductor optical amplifier based nonlinear optical loop mirror with feedback: Two modes of operation at high switching rates,” *Optics Communications*, vol. 157, no. 1-6, p. 45, 1998. DOI: [10.1016/S0030-4018\(98\)00513-6](https://doi.org/10.1016/S0030-4018(98)00513-6).
- [292] D. Chaparro, L. Furfaro, and S. Balle, “Subpicosecond pulses in a self-starting mode-locked semiconductor-based figure-of-eight fiber laser,” *Photonics Research*, vol. 5, no. 1, p. 37, 2017. DOI: [10.1364/PRJ.5.000037](https://doi.org/10.1364/PRJ.5.000037).
- [293] C. Antonelli and A. Mecozzi, “Reduced model for the nonlinear response of reflective semiconductor optical amplifiers,” *IEEE Photonics Technology Letters*, vol. 25, no. 23, p. 2243, 2013. DOI: [10.1109/LPT.2013.2282215](https://doi.org/10.1109/LPT.2013.2282215).
- [294] C. Antonelli, A. Mecozzi, Z. Hu, and M. Santagiustina, “Analytic study of the modulation response of reflective semiconductor optical amplifiers,” *Journal of Lightwave Technology*, vol. 33, no. 20, p. 4367, 2015. DOI: [10.1109/JLT.2015.2453232](https://doi.org/10.1109/JLT.2015.2453232).